Large Mass Interferometry for Understanding and Measuring Aspects of Gravity

Ryan J. Marshman

A dissertation submitted in partial fulfillment

of the requirements for the degree of

Doctor of Philosophy

of

University College London.

Department of Physics and Astronomy

University College London

29 March, 2022

I, Ryan J. Marshman, confirm that the work presented in this thesis is my own. Where information has been derived from other sources, I confirm that this has been indicated in the work.

Abstract

This thesis presents my work on exploring the use of large mass Stern-Gerlach interferometry for measuring both classical and quantum mechanical aspects of gravity. Chapter 1 serves as an introduction of the background physics necessary to understand this thesis. Part I (Chapters 2 and 3) is concerned with the underlying quantum mechanical mechanism behind a previously proposed experiment aimed at evidencing the quantum nature of gravity by witnessing gravitationally mediated entanglement. This includes determining the assumptions which must hold for a conclusion to be drawn from a positive result of the experiment and providing a clear and intuitive understanding behind what can and what can not be proved by such an experiment. Finally, this section presents the work done to explore further how entanglement forms in gravitationally interacting quantum systems. Part II of this thesis (Chapters4 and 5) discusses how a large mass interferometer will couple to the space-time metric for use as a detector. This includes considering the basic design of such a device, how different components of the space-time metric can be identified individually and an initial exploration of the final sensitivity of such a device given realistic noise parameters. Part III (Chapter 6) of this thesis looks at how such devices may be implemented experimentally, building off previous designs to create a large mass, large spatial superpositions with sufficient coherence to enable their use for interferometry. This is done to specifically design the interferometer around some issues and limitations with large mass interferometry using the Stern-Gerlach effect which have not been considered elsewhere.

Impact Statement

At the dawn of the twentieth century, two radical new theories for describing natural phenomena were developed. The first, quantum mechanics, lead to quantum field theory and the Standard Model. This represents our most complete description of all known particles and three of the four fundamental forces of nature, namely Electromagnetism and the Strong and Weak Nuclear Forces. Quantum field theory is built upon the two fundamental ideas: wave-particle duality and that forces are mediated by the exchange of an associated virtual particle, as described by Feynman diagrams. The second, General Relativity, tells us that gravitational interactions are due to massive objects warping the fabric of space itself. In this way, gravity can be thought of as due to the manipulation of space-time. Both of these theories have been hugely successful, but no unified description of nature has been found due to their fundamentally different descriptions of nature. One of the most challenging aspects of developing a unified description of reality is the lack of experimental tests in a regime where both are necessary to describe the system completely. Probing this regime may thus provide a significant opportunity for modern physics to progress. Recent proposals have opened the possibility of testing this regime using gravitationally mediated entanglement between two separate massive particle interferometers.

The first part of this thesis pertains to developing a complete understanding of precisely what would be evidenced by such an experiment. This includes considering how such an experiment may be used to characterise discrepancies in the strength of gravitational interactions at extremely short ranges, which are currently unexplored.

The second part of this thesis considers how such devices may be used as gravitational sensors. This opens the possibility of developing highly sensitive detectors capable of characterising the local space-time metric and its curvature. This may enable future gravitational wave observatories to be significantly smaller than previously considered and open new frequency regimes for earth-based detectors. Such devices could also be used for a variety of scientific and industrial applications, from geological surveys to detecting nearby massive objects in space.

The final section of this thesis pertains to practical considerations of how such devices can be built. Much of this work represents a first step toward realising the interferometric devices in question. However, this may also represent a step toward exciting developments in fundamental physics and massive particle devices with many scientific and industrial uses.

Acknowledgements

I would like to start by thanking Prof. Sougato Bose and Prof. Anupam Mazumdar for their encouragement and for guiding me throughout my PhD. They have taught me a lot about science, what it means to be a researcher, and how to deal with the dreaded referee 3.

I would also like to say thank you to my parents, Barry and Margaret Marshman, for instilling in me my love of science, for always encouraging me and for giving me so many opportunities throughout my life. Without them I would not be where I am today.

Finally, I would like to thank Caitlin, Matthew, John-Paul, Hazel, Thomas, Sunny and most importantly Alana. They were always there for me and kept me sane and smiling throughout the whole PhD. Without them I would never have had such a wonderful time throughout my Phd, let alone completed it. For that, I will always be grateful.

List of Publications

1 Ryan J. Marshman, Anupam Mazumdar, and Sougato Bose *Locality and Entanglement in Table-Top Testing of the Quantum Nature of Linearised Gravity*. Phys. Rev. A **101**, 052110 (2020)

2 Ryan J. Marshman, Anupam Mazumdar, Gavin W. Morley, Peter F. Barker, Steven Hoekstra, and Sougato Bose *Mesoscopic Interference for Metric and Curvature & Gravitational Wave Detection*. New Journal of Physics **22**, 083012 (2020)

3 Thomas W. van de Kamp, Ryan J. Marshman, Sougato Bose, and Anupam Mazumdar *Quantum Gravity Witness via Entanglement of Masses: Casimir Screening*. Phys. Rev. A. **102** 062809 (2020)

4 Marko Toroš, Thomas W. van de Kamp, Ryan J. Marshman, Myungshik Kim, Sougato Bose, and Anupam Mazumdar *Relative Acceleration Noise Mitigation for Nanocrystal Matter-wave Interferometry: Applications to Entangling Masses via Quantum Gravity*. Phys. Rev. Research **3** 023178 (2021)

5 Jules Tilly, Ryan J. Marshman, Anupam Mazumdar, and Sougato Bose *Qudits for Witnessing Quantum Gravity Induced Entanglement of Masses Under Decoherence*. Phys. Rev. A **104**, 052416 (2021)

6 Ryan J. Marshman, Anupam Mazumdar, Ron Folman, and Sougato Bose *Constructing Nano-Object Quantum Superpositions with a Stern-Gerlach Interferometer* (accepted for publication in Physical Review Research)

Contents

List of Figures

List of Symbols

The following list is neither exhaustive nor exclusive, but may be helpful.

$|\uparrow\rangle$, $|\downarrow\rangle$ . . . . . spin states

$|C\rangle$, $|L\rangle$, $|R\rangle$, $|x\rangle$ . . . . . position states

$|\psi\rangle$ /$|\Psi\rangle$ . . . . . one/two particle joint states

$\hat{U}$ . . . . . Time evolution operator

$\hat{\rho}$ . . . . . density matrix

ϕ . . . . . phase

m, M . . . . . mass

σ_x, σ_p . . . . . position, momentum uncertainty

σ . . . . . wave packet spread

$\Delta\alpha$ . . . . . relative difference of parameter α between two arms of the interferometer

$\delta\alpha$ . . . . . noise, uncertainty or variation in parameter α

S_γ . . . . . action calculated over path γ

$\hbar$ . . . . . Planck's constant

G . . . . . Newton's constant

$g_{\mu\nu}$ . . . . . space-time metric

$\eta_{\mu\nu}$ . . . . . Minkowski metric

$h_{\mu\nu}$ . . . . . space-time metric perturbation

Chapter 1

Introduction

This thesis presents an overview of the research I have undertaken throughout my PhD. My research focused on multiple aspects of interferometry with mesoscopic masses employing the Stern-Gerlach effect to create and manipulate spatial superpositions. It has included three specific topics:

- Work to understand better the underlying physics behind gravitational interactions in such a device, this makes up Part I (Chapters 2 and 3).

- Determining what purposes such a device might be beneficial for beyond pushing the boundaries of macroscopic superpositions or verifying the quantum nature of gravity. Specifically considering its use as a detector for gravitational effects. This is described in Part II (Chapters 4 and 5)

- Finally, determining how best to build such a device, considering how to obtain the maximal superposition size Δx with the largest mass m in the shortest time t. I also consider how other decoherence, noise and uncertainty effects limit such devices. This is given in Part III (Chapters 5 and 6).

This covers the research which I have undertaken, as well as the projects to which I have contributed substantially. The latter of which will be marked clearly at the start of the relevant chapter.

Chapter 2 details the work published in *Locality and Entanglement in Table-Top Testing of the Quantum Nature of Linearised Gravity*. This work helps establish

the underlying model for how linearised quantum mechanics describes the experiment previously proposed to witness gravitational mediated entanglement, potentially proving the quantum nature of gravity. Chapter 3 covers the work, which is still in progress, to take this further in considering how entanglement will form between two gravitationally interacting quantum masses in general. In Chapters 4 and 5 I will summaries the results published in *Mesoscopic Interference for Metric and Curvature & Gravitational Wave Detection*. This covers my proposal to use large mass interferometry for detecting the gravitational metric and its curvature, including gravitational waves using a metre scale device. Chapter 6 covers the work submitted under the title *Constructing Nano-Object Quantum Superpositions with a Stern-Gerlach Interferometer* on designing a Stern-Gerlach (SG) interferometer for large masses while accounting for diamagnetism, Majorana spin-flip transitions and ensuring the desired splitting direction is maintained. While I have endeavoured to present my own work exclusively, ultimately the work summarised in some of these chapters (Ch. 2, 4, 5, 6) was conducted while collaborating with my co-authors. Finally, Chapter 7 provides some concluding remarks on the research as a whole and summarises two other projects which I have contributed during my studies.

This project was inspired by the work proposing an experiment capable of evidencing the quantum nature of gravity [4, 5]. This work relies on the ability to place large (mesoscopic) masses in superpositions many times their radius such that they occupy a superposition of gravitationally distinct states. While there is a significant body of work on the use of atomic matter-wave interferometers [6], as well as efforts to push to larger then atomic masses and ever larger spatial superposition [7–24] for many uses, such as exploring collapse model modifications of quantum mechanics [25, 26], there was, up until recently, no promising candidate for placing large masses in spatially distinct superpositions. Recent work [3, 23, 27, 28] has demonstrated that Stern-Gerlach interferometry could be precisely the protocol required. My work focuses on detector applications for interferometers in the large mass, large superposition regime [4, 23, 24].

The first successful attempt to probe gravity using a quantum object was a

neutron interference experiment performed by Collela, Overhauser and Warner [1]. The so called COW experiment, named after the authors, involved using diffraction gratings to send a beam of neutrons through two different spatial trajectories, and interfering them afterwards. By rotating the entire apparatus they were able to alter the relative heights of the two trajectories through a background gravitational field sourced by the earth. They found that quantum phase accrued through each trajectory matched exactly that expected by treating the Newtonian gravitational potential as you would any background potential in standard quantum mechanics. Importantly this represented clear evidence that, while no quantum theory of gravity was known then (or even now), that the gravitational interaction can *coherently* interaction with a quantum system.

Since then, matter wave interferometry has progressed significantly, exemplified by two recent experiments. The first involved a light-pulse atom interferometer which demonstrated the ability to place atoms in two distinct locations separated by ~ 50 cm [2]. This represents a significant spatial superposition size. However, light-pulse interferometry cannot be used with large masses (relative to atomic masses) without inducing significant heating in the mass. This does however suggest significant coherent spatial splitting are achievable in practise. The second experiment was the successful demonstration of the use of Stern-Gerlach interferometry [3]. This involved utilising the coupling between an internal electronic spin state and an external magnetic field gradient, resulting in a spin dependent force acting on the atom (or larger crystal) holding the spin state. While the splitting sizes achieved were much smaller, this method of creating the superposition has the potential to be scaled to the use of much larger masses. It is with the background of these two significant advances in technology that this research was conducted. The hope is that by using a Stern-Gerlach interferometer, spatial superpositions approaching that already achieved for atoms might be possible for much larger masses, although this will be a significant endeavour.

There has been much work to get to these previously mentioned experiments, particularly on the use of atomic interferometers [1, 29, 30] but also larger optome-

chanical systems [31, 32]. These often focus on their use as a detector for the Newtonian potential and gravitational acceleration. Further work has considered the direct measurement of space-time curvature [33], or to detect the Earth's rotation [34, 35], or general relativistic effects [36–39]. The most difficult component of the gravitational metric to detect is the Gravitational Waves (GW), whose detection was famously achieved recently using laser interferometers [40, 41], but proposals exist for the use of atomic interferometers [42–48] and various resonators [49–53]. However, very little work has been done on using larger mass, matter-wave interferometers for such applications.

As for the more fundamental aspects of physics considered in this work, these generally revolve around the question of whether the gravitational force in fundamentally quantum. While it is often expected to be, there are several possible classical and semi-classical mechanisms which would generate a force with the same features as the Newtonian force [25, 54–62]. These generally rely on quantum states of matter coupling to the gravitational field via their spatial expectation values. If it is a quantum force, it is expected to be mediated by the exchange of off-shell (virtual) gravitons [63] similar to all other fundamental forces [64]. Since the original proposal for a quantum gravity induced entanglement of masses experiment (QGEM) [4, 5], there has been widespread debate about how best to interpret such an experiment and what conclusions should be drawn from a positive outcome of it [59, 65–71]. There have also been noise analysis [72], as well as related independent suggestions [73, 74].

1.1 Quantum Gravity Mediated Entanglement of Masses

The following is a brief description of the original QGEM proposal [4]. This is included to provide an overview of the experiment protocol itself. The details of precisely why this is sufficient to evidence the quantum nature of gravity is the subject of Chapter 2 and so is not included here. The set-up, shown in Fig. 1.1, consists of two mesoscopic mass ($\sim 10^{-14}$kg) nanospheres with embedded spins

traversing two Stern-Gerlach interferometers near to one another. The use of SG interferometers means that the spatial state will be correlated with the internal spin state. I will take the initial state of each spin-mass state to be $|\uparrow\rangle_i$ for particle i. The general scheme can then be summarised as follows:

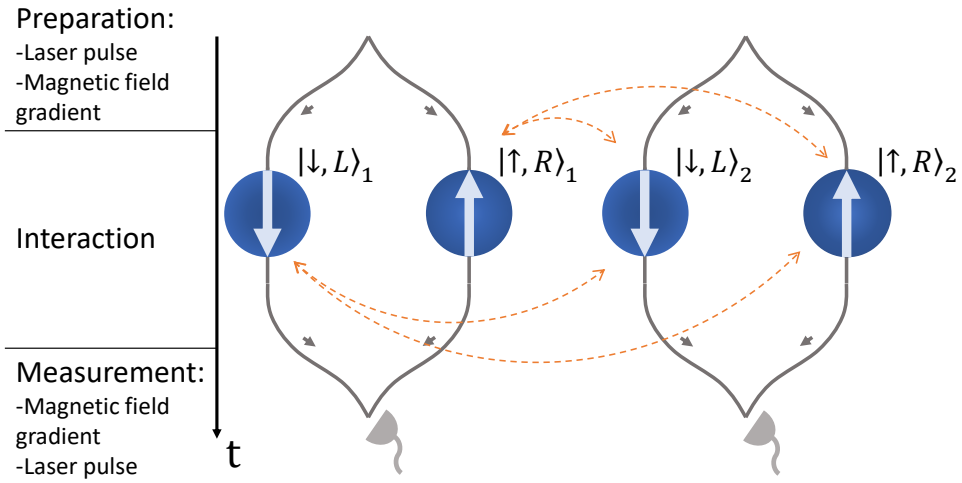

Figure 1.1: Simple representation of the QGEM experiment showing the key timesteps (preparation, interaction and measurment) and what must occur during them. The orange dashed lines represent the four distinct interactions, and hence space-time configurations, which must occur simultaneously. The particle state presented here corresponds to actual state during the interaction step.

$$
\begin{aligned}
&|\uparrow,C\rangle_1|\uparrow,C\rangle_2 \xrightarrow[\text{pulse}]{\text{Laser}} \frac{1}{2}\left(|\uparrow\rangle_1+|\downarrow\rangle_1\right)|C\rangle_1 \otimes \left(|\uparrow\rangle_2+|\downarrow\rangle_2\right)|C\rangle_2 \\
&\quad \xrightarrow[\text{field gradient}]{\text{Magnetic}} \frac{1}{2}\left(|\downarrow,L\rangle_1+|\uparrow,R\rangle_1\right)\otimes\left(|\downarrow,L\rangle_2+|\uparrow,R\rangle_2\right) \\
&\quad\quad \xrightarrow{\text{Interaction}} \frac{e^{i\phi}}{2}\left(|\downarrow,L\rangle_1|\downarrow,L\rangle_2+e^{i\Delta\phi_{LR}}|\downarrow,L\rangle_1|\uparrow,R\rangle_2+e^{i\Delta\phi_{RL}}|\uparrow,R\rangle_1|\downarrow,L\rangle_2+|\uparrow,R\rangle_1|\uparrow,R\rangle_2\right) \\
&\quad\quad \xrightarrow[\text{field gradient}]{\text{Magnetic}} \frac{e^{i\phi}}{2}\left(|\downarrow\rangle_1|\downarrow\rangle_2+e^{i\Delta\phi_{LR}}|\downarrow\rangle_1|\uparrow\rangle_2+e^{i\Delta\phi_{RL}}|\uparrow\rangle_1|\downarrow\rangle_2+|\uparrow\rangle_1|\uparrow\rangle_2\right)|C\rangle_1|C\rangle_2 \\
&\quad\quad\quad \xrightarrow[\text{pulse}]{\text{Laser}} \frac{e^{i\phi}}{4}\Big[\left(2-e^{i\Delta\phi_{LR}}-e^{i\Delta\phi_{RL}}\right)|\downarrow\rangle_1|\downarrow\rangle_2+\left(2+e^{i\Delta\phi_{LR}}+e^{i\Delta\phi_{RL}}\right)|\uparrow\rangle_1|\uparrow\rangle_2 \\
&\quad\quad\quad\quad +\left(e^{i\Delta\phi_{LR}}-e^{i\Delta\phi_{RL}}\right)\left(|\uparrow\rangle_1|\downarrow\rangle_2-|\downarrow\rangle_1|\uparrow\rangle_2\right)\Big]|C\rangle_1|C\rangle_2 \qquad (1.1)
\end{aligned}
$$

where

$$\phi \approx \frac{m\Phi(r_0)\,\tau}{\hbar}, \tag{1.2}$$

$$\Delta\phi_{LR} \approx \frac{m\tau}{\hbar}\left(\Phi(r_0+\Delta x)-\Phi(r_0)\right) \tag{1.3}$$

and

$$\Delta\phi_{RL} \approx \frac{m\tau}{\hbar}\left(\Phi(r_0-\Delta x)-\Phi(r_0)\right). \tag{1.4}$$

Here $\Phi(x)$ is the value of the interaction potential between the two masses at a distance x. Also $|C\rangle_i$, $|L\rangle_i$ and $|R\rangle_i$ represent the ith mass in its centre, left or right position state respectively. This shows that the internal spin states become entangled by the gravitationally mediated interaction between them. Importantly the masses position state factors out of the final joint state leaving only the internal spin states as entangled. Thus detecting any entanglement will require simple spin correlation measurements.

1.2 Quantum Mechanics

I will now provide a brief overview of the quantum mechanics used throughout this thesis. As previously discussed, this thesis will in part be investigating the entanglement that may form between gravitationally interacting masses. As such, it is worth first describing what entanglement is.

Consider two particles a and b which both act as qubits with the set of basis states $\{\|0\rangle_a, \|1\rangle_a\} \otimes \{\|0\rangle_b, \|1\rangle_b\}$. If we consider only pure states then the states are considered separable (and thus *not* entangled) if the joint state ($|\Psi\rangle$) can be written as

$$|\Psi_1\rangle = |\psi\rangle_a \otimes |\phi\rangle_b \tag{1.5}$$

for example, the bipartite state

$$|\Psi_1\rangle = \frac{1}{2}\left(|0\rangle_a + |1\rangle_a\right) \otimes \left(|0\rangle_b + |1\rangle_b\right) \tag{1.6}$$

If the joint state is *not* separable it is considered entangled. For example, the joint

state

$$|\Psi_2\rangle = \frac{1}{\sqrt{2}}\left(|0\rangle_a \otimes |0\rangle_b + |1\rangle_a \otimes |1\rangle_b\right) \tag{1.7}$$

cannot be written as the tensor product of two one-particle quantum states and is therefore entangled.

1.2.1 Phase from Action

It is also worth reviewing how the relative phase evolution can be calculated using the action, as it is used extensively throughout this thesis. The signal of an interferometer is determined by the relative phase of the interfering waves or wave-like particles at the output. This can be determined by measuring the length of every path taken through the interferometer in units of the de Broglie wavelength. This amounts to determining the wave's phase throughout the trajectory such that the phase difference at the point of interference can be determined. This is then used to calculate whether the paths lead to constructive (in phase) or destructive interference (out of phase). Doing so can be clumsy and will likely lead to many aspects of the complete evolution to be missed. Alternatively, the Feynman propagator [75] can be used. This gives the probability amplitude for the initial state of the particle as it enters the interferometer $|x_0, t_0\rangle$ to be found at point x_f and time t_f ($\left|x_f, t_f\right\rangle$) as

$$\left\langle x_f, t_f | x_0, t_0 \right\rangle \sim \sum_{\gamma} e^{\frac{iS_\gamma}{\hbar}} \tag{1.8}$$

where the sum is over all possible paths γ between the two space-time points and S_γ is the action for that path. Also, note that this is a somewhat loose definition for the Feynman path integral but provides the correct intuition behind the mathematics, hence the '$\sim$'. This appears to suggest it is necessary to calculate the action for all paths, however for massive particles, the action, defined as the integral over the particle's Lagrangian, is proportional to the mass, m, of the particle. Therefore, the propagator will contain terms of the form

$$e^{i\frac{m}{\hbar} f(\gamma)}. \tag{1.9}$$

As such, even slightly modified paths γ will see a rapidly oscillating phase given, for even modest masses of $m = 10^{-15}$ kg

$$\frac{m}{\hbar} \sim 10^9 \mathrm{m}^{-2}\mathrm{s}. \tag{1.10}$$

This will see all paths that are not extremal of the action generating a term with a random phase and so will, on average, not contribute to the final propagator. This results in a propagator which is, at least to the first order, only a function of paths that minimise the action. Hence, when considering large mass particles, even in quantum states, it is sufficient only to consider the classical trajectories, which by definition minimise the action, and perturbations around them.

For example, consider a large mass Stern-Gerlach interferometer. This will send a particle the along two classical trajectories according to its internal spin state. The probability amplitude for the mass to be detected at a given output o will be, up to the appropriate normalisation factor

$$\begin{aligned} \mathscr{A}_o =& e^{i\frac{S_{\gamma_1}}{\hbar}} + e^{i\frac{S_{\gamma_2}}{\hbar}} \\ =& e^{i\frac{S_{\gamma_1}}{\hbar}} \left(1 + e^{i\frac{S_{\gamma_2} - S_{\gamma_1}}{\hbar}}\right) \end{aligned} \tag{1.11}$$

and so the probability of observing the particle at output o, $P(o)$ will be

$$P(o) = |\mathscr{A}_o|^2 = \cos^2\left(\frac{S_{\gamma_2} - S_{\gamma_1}}{\hbar}\right). \tag{1.12}$$

This allows the identification that the particle phase along a trajectory ϕ_γ is determined by the action along that trajectory:

$$\phi_\gamma = \frac{S_\gamma}{\hbar} \tag{1.13}$$

As I am exclusively considering large mass interferometers, I will always assume it sufficient to consider the classical trajectories when calculating the output phase of an interferometry path.

1.3 General Relativity

The following section contains a brief overview of the background in General Relativity necessary to understand fully the work presented in this report. This section is based on information gained from Carroll's lecture series [76] and *Gravitation* by Misner, Thorne and Wheeler [77].

The essential feature to understanding General Relativity is the role played by the space-time metric, which I will generally refer to as simply the metric. To understand the metric, it is best to consider its role in Special Relativity (SR). SR is the result of requiring the speed of light to be constant for all observers, or more technically, that all physical laws hold for all inertial observers. To achieve this, it is necessary to consider space and time on a more level footing than what is standard in classical mechanics. This is done by first specifying locations not only in space but also in time through the use of four-vectors

$$x^{\mu} = \left(x^0, x^1, x^2, x^3\right) \equiv (t, x, y, z)\,. \tag{1.14}$$

Note that the Greek indices always include the spatial and time components, i.e. 0, 1, 2 and 3 while Latin indices refer only to the spatial components (1, 2 and 3)

I will generally restrict the analysis to the linear regime throughout this project, which is to say only metrics which are 'almost flat' are considered. This means that the metric can be written

$$g_{\mu\nu} = \eta_{\mu\nu} + h_{\mu\nu} \tag{1.15}$$

with $\left|h_{\mu\nu}\right| \ll 1$ and $\eta_{\mu\nu}$ is the Minkowski metric which represents flat space-time. I will take the metric signature $(-,+,+,+)$. Given the smallness of the perturbation, all indices are raised and lowered by the Minkowski metric. With this metric, the

Cristoffel symbols are

$$\begin{aligned}\Gamma^{\rho}_{\mu\nu} &= \frac{1}{2}g^{\rho\lambda}\left(\partial_\mu g_{\nu\lambda} + \partial_\nu g_{\lambda\mu} - \partial_\lambda g_{\mu\nu}\right) \\ &= \frac{1}{2}\left(\eta^{\rho\lambda} + h^{\rho\lambda}\right)\left(\partial_\mu\left(\eta_{\nu\lambda} + h_{\nu\lambda}\right) + \partial_\nu\left(\eta_{\lambda\mu} + h_{\lambda\mu}\right) - \partial_\lambda\left(\eta_{\nu\lambda} + h_{\nu\lambda}\right)\right) \\ &= \frac{1}{2}\eta^{\rho\lambda}\left(\partial_\mu h_{\nu\lambda} + \partial_\nu h_{\lambda\mu} - \partial_\lambda h_{\mu\nu}\right) \qquad (1.16)\end{aligned}$$

with all non linear terms in $h_{\mu\nu}$ dropped and using $\partial_\lambda \eta_{\mu\nu} = 0$.

The curvature of space-time characterised by the set of objects known as the Riemann tensor ($R^{\rho}_{\sigma\mu\nu}$) Ricci tensor ($R_{\mu\nu}$) and the Ricci scalar (R) which are defined as

$$R^{\rho}_{\sigma\mu\nu} = \partial_\mu\Gamma^{\rho}_{\nu\sigma} - \partial_\nu\Gamma^{\rho}_{\mu\sigma} + \Gamma^{\rho}_{\mu\lambda}\Gamma^{\lambda}_{\nu\sigma} - \Gamma^{\rho}_{\nu\lambda}\Gamma^{\lambda}_{\mu\sigma} \qquad (1.17)$$

$$R_{\mu\nu} = R^{\lambda}_{\mu\lambda\nu} \qquad (1.18)$$

$$R = R^{\mu}_{\mu}. \qquad (1.19)$$

However, since we are considering linearised gravity, they can be expanded to

$$\begin{aligned}R^{\mu}_{\nu\rho\sigma} &= \partial_\rho\Gamma^{\mu}_{\nu\sigma} - \partial_\sigma\Gamma^{\mu}_{\nu\rho} + O\left(\left(h_{\mu\nu}\right)^2\right) \\ &= \frac{1}{2}\partial_\rho\eta^{\mu\lambda}\left(\partial_\nu h_{\sigma\lambda} + \partial_\sigma h_{\lambda\nu} - \partial_\lambda h_{\nu\sigma}\right) - \frac{1}{2}\partial_\sigma\eta^{\mu\lambda}\left(\partial_\nu h_{\rho\lambda} + \partial_\rho h_{\lambda\nu} - \partial_\lambda h_{\nu\rho}\right) \\ &= \frac{1}{2}\left(\partial_\rho\partial_\nu h^{\mu}_{\sigma} + \partial_\rho\partial_\sigma h^{\mu}_{\nu} - \partial_\rho\partial^{\mu}h_{\nu\sigma}\right) - \left(\partial_\sigma\partial_\nu h^{\mu}_{\rho} + \partial_\sigma\partial_\rho h^{\mu}_{\nu} - \partial_\sigma\partial^{\mu}h_{\nu\rho}\right) \\ &= \frac{1}{2}\left(\partial_\rho\partial_\nu h^{\mu}_{\sigma} + \partial_\sigma\partial^{\mu}h_{\nu\rho} - \partial_\rho\partial^{\mu}h_{\nu\sigma} - \partial_\sigma\partial_\nu h^{\mu}_{\rho}\right). \qquad (1.20)\end{aligned}$$

Similarly, the Ricci tensor is

$$R^{\mu}_{\nu\mu\sigma} = \frac{1}{2}\left(\partial_\mu\partial_\nu h^{\mu}_{\sigma} + \partial_\sigma\partial^{\mu}h_{\nu\mu} - \partial_\mu\partial^{\mu}h_{\nu\sigma} - \partial_\sigma\partial_\nu h^{\mu}_{\mu}\right) \qquad (1.21)$$

$$R_{\mu\nu} = \frac{1}{2}\left(\partial_\lambda\partial_\mu h^{\lambda}_{\nu} + \partial_\nu\partial^{\lambda}h_{\mu\lambda} - \partial_\mu\partial_\nu h - \Box h_{\mu\nu}\right) \qquad (1.22)$$

and the Ricci scalar becomes

$$R = \partial_\lambda\partial_\mu h^{\lambda\mu} - \Box h. \qquad (1.23)$$

With this, the action for the metric tensor, also known as the Einstein-Hilbert action, can be written

$$\begin{aligned} S_{EH} &= \int d^4x\sqrt{-g}R \\ &= \int d^4x h^{\mu\nu}\left(R_{\mu\nu} - \frac{1}{2}\eta_{\mu\nu}R\right) \end{aligned} \tag{1.24}$$

To get the above expansion, one can Taylor expand about a small perturbation $h_{\mu\nu}$, writing

$$\begin{aligned} S_{EH}\left(g_{\mu\nu}\right) =& S_{EH}\left(\eta_{\mu\nu}\right) + \frac{\delta S_{EH}\left(\eta_{\mu\nu}\right)}{\delta g^{\mu\nu}}\delta g^{\mu\nu}, \\ \frac{\delta S_{EH}\left(\eta_{\mu\nu}\right)}{\delta g^{\mu\nu}}\delta g_{\mu\nu} =& \frac{\delta}{\delta g^{\mu\nu}}\left(\int d^4x\sqrt{-g}R\right)\delta g^{\mu\nu} \\ =& \int d^4x\left(\frac{\delta R}{\delta g^{\mu\nu}} + \frac{\delta\sqrt{-g}}{\delta g^{\mu\nu}}\frac{R}{\sqrt{-g}}\right)\sqrt{-\eta}\delta g^{\mu\nu} \\ =& \int d^4x\left(R_{\mu\nu} - \frac{1}{2}\frac{g g_{\mu\nu}\delta g^{\mu\nu}}{\delta g^{\mu\nu}}\frac{R}{\sqrt{-g}}\right)\delta g^{\mu\nu} \\ \implies S_{EH} =& \int d^4x h^{\mu\nu}\left(R_{\mu\nu} - \frac{1}{2}\eta_{\mu\nu}R\right) \end{aligned} \tag{1.25}$$

This can be further expanded to give the Lagrangian density

$$\mathscr{L}_{EH} = \frac{1}{2}h_{\mu\nu}\mathscr{O}^{\mu\nu\rho\sigma}h_{\rho\sigma} \tag{1.26}$$

where $\mathscr{O}^{\mu\nu\rho\sigma}$ can be expressed as a linear combination of terms of the form $\eta^{\alpha\beta}\partial^\gamma\partial^\delta$ whose details are unimportant here. Doing so, once the appropriate gauge fixing terms have been added, allows field equations to be found for the gravitational field, which can then be inverted yielding the graviton propagator.

1.3.1 Gravitational Waves

One of the interesting predictions of the space-time metric is the existence of gravitational waves. Gravitational waves are dynamic degrees of freedom of the space-time metric and are generally considered in what is known as the weak field limit.

So again considering an approximately flat metric with some time dependent perturbation, small enough such that its only important to low orders. Again, writing the metric as $g_{\mu\nu} = \eta_{\mu\nu} + h_{\mu\nu}$ with $\left|h_{\mu\nu}\right| \ll 1$ and $\eta_{\mu\nu}$ is the Minkowski metric. Given the smallness of the perturbation, all indices are raised and lowered by the Minkowski metric. To derive the form of the gravitational waves it is customary to work in the transverse traceless gauge (TT), such that

$$h^{\mu}_{\mu} = 0 \tag{1.27}$$

$$\partial_{\mu} h^{\mu}_{\nu} = 0. \tag{1.28}$$

I am not considering the source to gravitational waves, and as such will look for dynamic solutions to Einstein's equations in the vacuum, that is

$$\begin{aligned} 0 &= R_{\mu\nu} - \frac{1}{2} R g_{\mu\nu} \\ &= \frac{1}{2}\left(\partial_{\lambda}\partial_{\mu} h^{\lambda}_{\nu} + \partial_{\nu}\partial^{\lambda} h_{\mu\lambda} - \Box h_{\mu\nu}\right) - \frac{1}{2}\partial_{\lambda}\partial_{\mu} h^{\lambda\mu}\left(\eta_{\mu\nu} + h_{\mu\nu}\right) \\ &= \Box h_{\mu\nu} \end{aligned} \tag{1.29}$$

where I have simplified by dropping all higher order terms in $h_{\mu\nu}$ as well as enforcing the Lorentz gauge whereby

$$\partial_{\mu} h^{\mu}_{\nu} = 0. \tag{1.30}$$

This can be identified as a relativistic wave equation. A well known set of general solutions to Eq. 1.29 is

$$h_{\mu\nu} = A_{\mu\nu} e^{i k_{\alpha} x^{\alpha}}, \tag{1.31}$$

substituting this solution back into the wave equation gives

$$\begin{aligned} 0 &= \Box h_{\mu\nu} \\ &= \Box A_{\mu\nu} e^{i k_{\alpha} x^{\alpha}} \\ &= -k_{\alpha} k^{\alpha} h_{\mu\nu} \\ \implies k_{\alpha} k^{\alpha} &= 0 \end{aligned} \tag{1.32}$$

which implies the wave travels at the speed of light. This also eliminates a degree of freedom in $h_{\mu\nu}$ given $\omega^2 = k_j k^j$ where $k_\alpha = \left(\omega, k_j\right)$. The Lorentz gauge condition imposes

$$\begin{aligned} 0 &= \partial_\mu h^{\mu\nu} \\ &= ik_\mu h^{\mu\nu} \\ \implies 0 &= k_\mu h^{\mu\nu}. \end{aligned} \tag{1.33}$$

As such, this gravitational wave must be a transverse wave, hence the transverse moniker in the TT gauge. Finally, all remaining degrees of freedom in the space-time metric can be eliminated by imposing

$$A_{\mu\nu} u^\nu = 0. \tag{1.34}$$

By choosing $u^\mu = \left(1, \vec{0}\right)$ all time components of $A_{\mu\nu}$ can be set to zero. With all this we can conclude

$$h_{\mu\nu} = \left(h_+ \begin{bmatrix} 0 & 0 & 0 & 0 \\ 0 & 1 & 0 & 0 \\ 0 & 0 & -1 & 0 \\ 0 & 0 & 0 & 0 \end{bmatrix} + h_\times \begin{bmatrix} 0 & 0 & 0 & 0 \\ 0 & 0 & 1 & 0 \\ 0 & 1 & 0 & 0 \\ 0 & 0 & 0 & 0 \end{bmatrix} \right) e^{ik_\alpha x^\alpha} \tag{1.35}$$

where the x_3 direction has been fixed to the direction of propagation for the wave. Thus gravitational waves are waves propagating through the space-time metric with two possible polarisations, here written as h_+ and $h_\times$. One can imagine these gravitational waves in a manner similar to sound waves, only with the wave travelling in the transverse direction rather than longitudinally with the compression and rearification occurring to space-time itself. Furthermore, this stretching and compressing occurs in both transverse spatial directions simultaneously. It is this effect which has been directly detected by laser interferometers known as aLIGO [41]. They are large Michelson-Morley interferometers, where the gravitational wave simultaneously stretch the spatial length of one arm and compress the other, leading to

observable interference fringes.

Part I

Sensing Quantum Gravity

Chapter 2

Quantum Nature of Gravity

This chapter summaries the work published in the paper titled *Locality and Entanglement in Table-Top Testing of the Quantum Nature of Linearised Gravity*, which aims to describe the underlying assumptions and physics underpinning the experimental proposal published in [4] and also discussed in [5]. These papers suggest that evidence for the quantum nature of linearised gravity could be observed by entangling two masses using only their gravitational interaction. The QGEM proposal suggests that if each mass is placed in a spatial superposition state, coupled to an internal spin degree of freedom, then any gravitationally induced entanglement might be witnessed by measuring the internal spin state. The argument presented in the original paper then posits that by the properties of LOCC, given the mediating channel is gravitational, if any entanglement is witnessed, it must be quantum.

This work set out to answer three primary questions that must be answered to understand the QGEM experiment:

- What are what aspects of gravity are being considered?
- What does it mean for something, and in particular a field, to be quantum?
- How would witnessing entanglement in the QGEM experiment verify that the gravitational field is quantum in nature?

The first two questions have at least superficially straightforward answers. Specifically, as the QGEM experiment involves two $\sim 10^{-14}$ kg masses interacting over distances ~ 100 μm it can be seen that the gravitational interaction is strongly

dominated by the Newtonian interaction, at least under the assumption that there is no as yet undetected, non-Newtonian interactions which occur at such length scales. Also, a field can be considered quantum if it is evidenced to be in a superposition, or a field can be considered quantum if it is capable of acting as an entangling channel via the properties of the group known as LOCC as discussed in Section 2.3. To understand the QGEM experiment entirely, it is necessary to discuss these questions and their answers in detail.

2.1 Gravity in QGEM

This section will seek to explore and clarify the boundary between the quantum world and general relativity in the linear regime, the relevant domain for considering gravity in the QGEM experiment. To do this, I will present an outline of the standard relativistic quantum field theory (RQFT) model for relativity. I will then use this to model the experiment proposed in *A Spin Entanglement Witness for Quantum Gravity* [4] while focusing on aspects that were not previously highlighted in that paper. I will then attempt to demonstrate the necessity of a quantum gravitational field capable of existing in a superposition for the generation of entanglement in such an experiment. This will highlight how similar systems can be used to test modifications to Newtonian gravity further.

To model an interaction between a mass and the gravitational field using RQFT, it is helpful to begin with the Einstein-Hilbert (gravity field) action, and from this, find graviton propagator. The Einstein-Hilbert action is given

$$S_{EH} = \int d^4x\sqrt{-g}R. \tag{2.1}$$

This can be expanded in the linear gravity regime where $g_{\mu\nu} = \eta_{\mu\nu} + h_{\mu\nu}$ given that $\left|h_{\mu\nu}\right| \ll 1$ where $\eta_{\mu\nu}$ is the Minkowski metric. This gives

$$S_{EH} = \frac{1}{4}\int d^4x\, h_{\mu\nu}\,\mathscr{O}^{\mu\nu\rho\sigma}\,h_{\rho\sigma} + O(\kappa h^3), \tag{2.2}$$

where $O(\kappa h^3)$ are the higher order perturbation terms. The four-rank operator

$\mathscr{O}^{\mu\nu\rho\sigma}$ is totally symmetric in all its indices and defined as

$$\begin{aligned}\mathscr{O}^{\mu\nu\rho\sigma} &= \frac{1}{4}(\eta^{\mu\rho}\eta^{\nu\sigma}+\eta^{\mu\sigma}\eta^{\nu\rho})\Box-\frac{1}{2}\eta^{\mu\nu}\eta^{\rho\sigma}\Box \\ &+\frac{1}{2}(\eta^{\mu\nu}\partial^{\rho}\partial^{\sigma}+\eta^{\rho\sigma}\partial^{\mu}\partial^{\nu}-\eta^{\mu\rho}\partial^{\nu}\partial^{\sigma}-\eta^{\mu\sigma}\partial^{\nu}\partial^{\rho}),\end{aligned} \tag{2.3}$$

for $\Box = \eta_{\mu\nu}\nabla^{\mu}\nabla^{\nu}$. The kinetic operator can then be inverted to obtain the graviton propagator, again as expanded around the Minkowski background, with its gauge independent part given by [78, 79]

$$\Pi_{\mu\nu\rho\sigma}(k) = \frac{1}{2\vec{k}^2}\left(\eta_{\mu\rho}\eta_{\nu\sigma}+\eta_{\nu\rho}\eta_{\mu\sigma}-\eta_{\mu\nu}\eta_{\rho\sigma}\right) \tag{2.4}$$

$$= \left(\frac{\mathscr{P}^2_{\mu\nu\rho\sigma}}{k^2}-\frac{\mathscr{P}^0_{s,\mu\nu\rho\sigma}}{2k^2}\right), \tag{2.5}$$

where $\mathscr{P}^2$ and $\mathscr{P}^0_s$ are two spin projection operators projecting along the spin-2 and spin-0 components, respectively. See Refs.[78, 79] for further details. To calculate the interaction energy between two masses, it is necessary first to find the appropriate stress-energy tensor, $T^{\mu\nu}$, corresponding to the masses. For a non-relativistic setup, this will include only the 00 components. To see this, note that for a particle moving at non-relativistic speeds, the stress-energy tensor can be approximated as

$$T^{\mu\nu} = \frac{E v^{\mu} v^{\nu}}{c^2}\delta(\vec{x}-\vec{\chi}) \tag{2.6}$$

where $\vec{\chi}$ and v^{μ} is the particles position and four velocity. Thus, given the masses involve move at highly non-relativistic speeds, all but the T^{00} component will be suppressed by a factor of $c^2 \sim 10^{-17}$. For a particle of mass m located at the origin ($T_1^{\mu\nu} \sim m\delta_0^{\mu}\delta_0^{\nu}\delta^{(3)}(0)$) and a unit mass at $\vec{r}$ ($T_2^{\mu\nu} \sim \delta_0^{\mu}\delta_0^{\nu}\delta^{(3)}(\vec{r})$), the potential is found by integrating all the momenta of the off-shell graviton (specifically those that do not obey the classical equations of motion)

$$\begin{aligned}\Phi(r) &= -\kappa^2\int\frac{d^3|\vec{k}|}{(2\pi)^3}T_1^{00}(k)\Pi_{0000}(k)T_2^{00}(-k)e^{i\vec{k}\cdot\vec{r}} \\ &= -\frac{\kappa^2 m}{2}\int\frac{d^3|\vec{k}|}{(2\pi)^3}\frac{1}{\vec{k}^2}e^{i\vec{k}\cdot\vec{r}} = -\frac{Gm}{r}.\end{aligned} \tag{2.7}$$

So starting with the graviton propagator, which is derived directly from General relativity in the linear regime, the Newtonian potential arises. This is nothing more than undergraduate-level physics but provides a quantum foundation for the gravitational interaction. It also demonstrates that provided the experiment is truly represented by the linearised gravity regime (see the discussion below in section 2.5), then it is possible the exchange of off-shell gravitons is what mediates the gravitational interaction between masses. This off-shell process of exchange of gravitons as captured by the propagator can then be seen as the quantum underpinning, which is sufficient to provide the necessary quantum mediator for the entanglement proposed in [4].

Of course, simply providing a *possible* quantum mechanism for linearised quantum gravity is *not* sufficient to prove that gravity is fundamentally a quantum force. However, in the next section, I will seek to lay out the specific argument behind why a positive result in the QGEM experiment would prove that the gravitational interaction is quantum.

2.2 Entanglement Between Gravitationally Interacting Interferometers

Now that a quantum mediator has been established as possible, I will seek to demonstrate that it is required to understand entanglement formation in the QGEM experiment. The most fundamental aspect underpinning the requirement of quantumness is locality. It is a central assumption in quantum field theory, ensuring microcausality between two quantum field operators. It is also generally taken as a given for all quantum and classical interactions to ensure causality holds in general. This then also ensures that information cannot violate special relativity, among other key observations of nature. Given this assumption, it is reasonable to treat each interferometer as a local region, in which local operations are performed to create the spatial superposition and measure the internal spin state of the masses. In these local regions, arbitrary transformations are allowed (although successful implementation of the QGEM protocol requires a few very specific ones). Meanwhile,

the two masses interact via the local gravitational field, which acts as a mediating channel. In this way, despite the two masses being non-local to one another, they still interact via only local effects. This setup is shown in Figure 2.1. The experimentalists need to ensure that this mediating channel is only gravitational. This can be achieved with careful preparation of the masses, ensuring the ideal distance between the masses and using conductive plates to screen the masses (see [4] and [80]). In this way, the entire experiment can be treated as two local experiments, connected via either a classical or quantum channel, depending on the fundamental nature of the gravitational interaction. The experiment is then run with the aim of entangling the masses via the mediating gravitational interaction. Provided the two masses are not initialised in an entangled state, the formation of any entanglement can be directly interpreted as evidence that the mediating gravitational interaction is fundamentally quantum. This holds due to the properties of the set of transformations known as LOCC (see section 2.3 for more details). It is also worth noting that the masses can also be initialised in an entangled state. The experimentalists would then have the more difficult task of verifying an *increase* in the total entanglement between the masses. This would still prove the quantum nature of the mediating channel as LOCC is strictly entanglement non-increasing.

Alternatively, it is possible to see the necessity of the gravitational field by considering the pairwise interaction of the four joint states which describe the system once it is initialised with the two spatial superpositions, i.e. $|l,\uparrow\rangle \otimes |L,\uparrow\rangle$, $|l,\uparrow\rangle \otimes |R,\downarrow\rangle$, $|r,\downarrow\rangle \otimes |L,\uparrow\rangle$ and $|r,\downarrow\rangle \otimes |R,\downarrow\rangle$. For the two states $|l,\uparrow\rangle \otimes |L,\uparrow\rangle$ and $|l,\uparrow\rangle \otimes |R,\downarrow\rangle$, the gravitational field as experienced by the right mass (corresponding to capital letter notation) corresponds to the the left mass being in the state $|l,\uparrow\rangle$. This is shown in figure 2.1 by interactions U_{lL} and U_{lR}. However, the gravitational field experienced by the right mass for the joint states $|r,\downarrow\rangle \otimes |L,\uparrow\rangle$ and $|r,\downarrow\rangle \otimes |R,\downarrow\rangle$ require the gravitational field as corresponding to the left mass being in the $|l,\uparrow\rangle$ state. For entanglement to form, the states $|l,\uparrow\rangle \otimes |L,\uparrow\rangle$ and $|l,\uparrow\rangle \otimes |R,\downarrow\rangle$ *can not* experience interactions U_{lL} and U_{lR}, and as such the gravitational field itself must be viewed as being in a superposition state. Otherwise, if the gravitational field was

in either a statistical mixture, then only some of the required interactions U_{iJ} would occur in any given experimental run and no entanglement would develop. Alternatively if the gravitational field maintains classicality by corresponding to that for all four arms populated simultaneously, then again no entanglement would form as each mass would evolve according to the other mass occupying both position states simultaneously in the classical sense.

Such an argument does rely on the masses being in 'noon' states, that is, when written in the Fock basis, the state will be $\frac{1}{\sqrt{2}}\left(\hat{\phi}_1^\dagger(l)+\hat{\phi}_1^\dagger(r)\right)|0\rangle$. This will ensure there cannot be any interaction between the two arms within an interferometer of the form shown in Fig 2.1 by U_{lr}. If, for example, a Bose-Einstein Condensate (BEC) is used one might expect something more akin to coherent states in each arm of the interferometer of the form $e^{\frac{|\alpha_l|^2}{2}}e^{\frac{|\alpha_r|^2}{2}}e^{\alpha_l\hat{\phi}_1^\dagger(l)}e^{\alpha_r\hat{\phi}_1^\dagger(r)}|0\rangle$. This would create interactions of the form U_{lr} which will not result in entanglement in the manner here desired. Instead, the gravitational interaction would be dominated by every atom experiencing a non-entangling, mean-field interaction sourced by the large number of atoms in each arm of both interferometers. As such we would expect negligible entanglement to form between the interferometers. Furthermore it is desirable to use highly localised states such that $U_{ll'}$ type interactions as shown in Fig. 2.1 could not impact the final result. If a continuous stream of particles were used, such interactions ($U_{aa'/bb'}$ and $U_{lr/LR}$) may overwhelm any signal from the inter-arm interactions (U_{aB})

2.3 Impossibility of Entanglement Through a Classical Field: Local Operations and Classical Communications

To highlight the role of a quantum channel in the formation of entanglement, I will here present a counter-example of the entanglement experiment mediated by a purely classical field $h_{\mu\nu}$. The matter states consist of two quantized systems A and B at separate locations. The gravity-matter coupling is given by $h_{\mu\nu}T^{\mu\nu}$

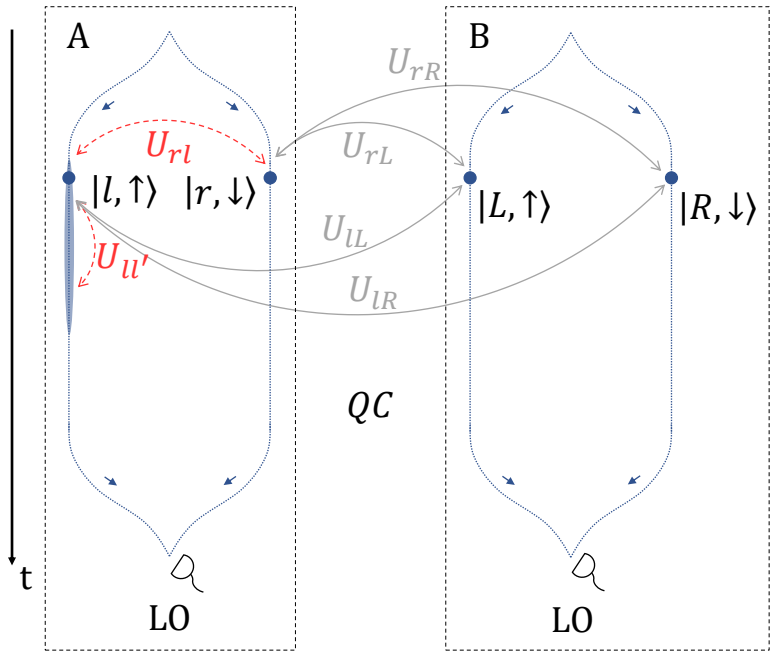

Figure 2.1: Experiment set-up showing the two interferometers, the two particles (A and B) and their trajectories (dotted blue path). The dashed rectangle encompasses the local operations (LO) regions for particles A and B. The solid grey lines show the gravitational interactions (quantum channel QC) which would lead to the formation of entanglement. The dashed red lines are example of some of the unwanted interactions which could occur for non-Fock mass states. Note the particle in the left arm of the left interferometer is shown as both a localised mass (dark blue circle) and numerous, large spatially spread particles (lighter blue oval).

where $T^{\mu\nu}$ is the quantum operator which encodes the masses associated stress-energy tensor. This will give rise to solely unitary evolutions of the quantized matter systems. I will consider three time steps: $t < 0$ before the spatial superposition is created at time $t = 0$; $0 \leq t \leq \delta t$, after the superposition has been created, but before any information has had time to propagate between A and B; and finally $t > \delta t$, when both A and B are within the light cone of the other mass' past when its in a superposition.

When $t < 0$, the mass states will be in a product (unentangled) state $|\psi(t)\rangle_A \otimes |\phi(t)\rangle_B$ and the gravity field will be $h_{\mu\nu}(\vec{r}, t < 0)$. Trivially any evolution occurring in the systems A and B will not induce entanglement as the superposition states to be entangled do not exist. For $0 \leq t \leq \delta t$, the mass states will

evolve according to some unitary operator $\hat{U}_A(t,|\psi(0\leq t\leq\delta t)\rangle,|\phi(t<0)\rangle)\otimes\hat{U}_B(t,|\psi(t<0)\rangle,|\phi(0\leq t\leq\delta t)\rangle)$, with the gravitational field in the regions of the two masses will be of the form $h_{\mu\nu}(\vec{r}_A,t)=f_{\mu\nu}(|\psi(t)\rangle_A,|\phi(t<0)\rangle_B)$ and $h_{\mu\nu}(\vec{r}_B,t)=f_{\mu\nu}(|\psi(t<0)\rangle_A,|\phi(t)\rangle_B)$. At later times, once both superposition states have interacted through the gravitational field ($t>\delta t$) the evolution operator will be of the form $\hat{U}_A(t,|\psi(t)\rangle,|\phi(t)\rangle)\otimes\hat{U}_B(t,|\psi(t)\rangle,|\phi(t)\rangle)$, that is, each system can evolve in a time dependent fashion, and depending on the state of both systems, however the evolution occurs in a separable manner. The gravitational field will similarly be of the form $h_{\mu\nu}(\vec{r},t)=f_{\mu\nu}(|\psi(t)\rangle_A,|\phi(t)\rangle_B)$.

The above description can be expanded to allow a probabilistic gravitational field $h_{\mu\nu}(\vec{r},t,j)$ whereby the field value depends probabilistically on, for example, it 'measuring' the location of the matter, giving the jth result with probability $P(j)$. In such a case however the result is still qualitatively the same, with the state's evolution operators being of the form $\hat{U}_A(t,|\psi(t)\rangle,|\phi(t)\rangle,j)\otimes\hat{U}_B(t,|\psi(t)\rangle,|\phi(t)\rangle,j)$, again taking separable states to separable states. As such it can clearly be seen that at no stage can entanglement between the two masses form via a purely classical intermediary.

Now the above argument can be expanded to allow arbitrary sets of local operations, $\{\hat{A}_j\}$ and $\{\hat{B}_j\}$ that can act on systems A and B respectively. These include unitary operations, more generally completely positive maps, and the action of general measurement operators (as given by Kraus operators). These operations can be thought of as enacted by experimentalists Alice or Bob, due to the natural evolution of the system in isolation, due to the interaction with a classical field (unitary), through fundamental nonlinear modifications of quantum dynamics leading to intrinsic measurement operations (as in collapse models), or any combination of these. Alice (or indeed nature) can then act on system A to produce the state

$$\hat{\rho}_{A,j}=\hat{A}_j|\psi\rangle\langle\psi|\hat{A}_j^\dagger, \tag{2.8}$$

where I will ignore normalization for simplicity. In the above, the symbol j comes in only if the operation on A was a generalized measurement (by Alice or due to some

dynamical collapse model) with $\rho_{A,j}$ corresponding to the jth outcome. This leads to the gravitational field $h_{\mu\nu}(t,\vec{r},j)$ derived as a function of $\hat{\rho}_{A,j}$ (the dependence of the classical field $h_{\mu\nu}(t,\vec{r},j)$ on $\hat{\rho}_{A,j}$ can be according to any mapping). Now depending on this $h_{\mu\nu}(\vec{r},t,j)$, system B will evolve as

$$\hat{\rho}_B^{(j)} = \hat{B}_k^{(j)}|\phi\rangle\langle\phi|\hat{B}_k^{\dagger(j)}, \tag{2.9}$$

which again manipulates the field, now giving $h_{\mu\nu}(t,\vec{r},j,k)$. At this stage, there will be a continued swapping of information between A and B. However, this is already sufficient to produce a state suitable to illustrate the point. Taking an initial state as a product state (this occurs by virtue of the QGEM protocol) the final state will be given by:

$$\begin{aligned} \hat{\rho}(t=0) &= \rho_A \otimes \rho_B, \\ \hat{\rho}(t=\delta t) &= \textstyle\sum_j \hat{A}_j|\psi\rangle\langle\psi|\hat{A}_j^\dagger \otimes \hat{B}_k^{(j)}|\phi\rangle\langle\phi|\hat{B}_k^{\dagger(j)}, \end{aligned} \tag{2.10}$$

which is a product state. To extend this to the completely general case of an arbitrary separable initial state, which can be a probabilistic summation over product states, giving the final state

$$\hat{\rho}(t=\delta t) = \sum_l \sum_j p(l)\hat{A}_{jl}|\psi\rangle\langle\psi|\hat{A}_{jl}^\dagger \otimes \hat{B}_{kl}^{(j)}|\phi\rangle\langle\phi|\hat{B}_{kl}^{\dagger(j)}. \tag{2.11}$$

Due to the generality of the above treatment, it follows that starting from a separable state of two systems A and B, quantum entanglement cannot be generated by any model in which gravity is a classical field (classical according to the very reasonable definition given in section 2.5). This automatically encompasses all specific models such as the Moller-Rosenfeld semiclassical gravity model or models where the matter field undergoes collapses and sources a stochastic classical gravitational field.

2.4 Witnessing Entanglement through Measurement Statistics

To fully understand the experiment described in [4], it is necessary to understand how entanglement can be detected. Remembering that for a bipartite state to be entangled means its state cannot be written as the tensor product of the states of each particle. That is, a state is not entangled (it is separable) if it can be written

$$\hat{\rho} = \sum_j p(j)\, \hat{\rho}_{A,j} \otimes \hat{\rho}_{B,j} \tag{2.12}$$

where $\hat{\rho}_{A,j} = |\phi\rangle\langle\phi|_A$ and $\hat{\rho}_{B,j} = |\chi\rangle\langle\chi|_B$ are arbitrary states belonging to the Hilbert space of particles A and B respectively and $\sum_j p(j) = 1$. If we restrict ourselves to bipartite, pure qubit states, then we can understand and quantify entanglement by the von Neumann entropy of the reduced density matrix. The von Neumann entropy, S, for the joint state is defined as

$$\begin{aligned} S &= -\operatorname{Tr}[\rho_a \log_2(\rho_a)] \\ &= -\sum_\lambda \operatorname{Tr}[\lambda \log_2(\lambda)] \end{aligned} \tag{2.13}$$

where λ are the eigenvalues of ρ_a, the reduced density matrix for particle a, defined as

$$\rho_a = \sum_j \langle j|_b |\Psi\rangle\langle\Psi| j\rangle_b \tag{2.14}$$

and the summation is over a complete basis for particle b. Note that the von Neumann entropy can be equivalently defined by tracing over particle a, leaving the reduced density operator for particle b. The entropy is then bounded from above by $\log_2(n)$ for an n dimensional system. It is maximised ($S = \log_2(n)$) when the system is fully entangled and zero for separable states. As such, the von Neumann entropy characterises the entanglement for a joint state. This can be understood as when two particles are entangled, tracing over one of them throws away the information content of both the masses. In comparison, if the two particles are not

entangled then throwing away the information contained in one of the particle states has no bearing on the information stored in the other. The von Neumann entropy is useful for characterising the entanglement as it is an entanglement monotone. That is to say that the entropy is non-decreasing with increasing entanglement. As such, if the von Neumann entropy is seen to increase, the states must be becoming more entangled. This is not the only method of characterising the entanglement; however it is the most common method used throughout this thesis.

In a realistic experiment however, we cannot rule out non-pure states throughout the evolution. In this case the von Neumann entropy could be also maximised by decoherence through other channels. As a result of this, entanglement measures which are compatible with mixed states must be used. For example, the concurrence or an entanglement witness can be used. The concurrence can be calculated for a general (pure or mixed) two qubit state, using

$$C(\rho) = \max\{0, \lambda_1 - \lambda_2 - \lambda_3 - \lambda_4\} \tag{2.15}$$

where λ_i is the square root of the eigenvalues of the matrix $\hat{\rho}\tilde{\rho}$ arranged in decreasing order, where $\tilde{\rho} = (\sigma_y \otimes \sigma_y)\,\hat{\rho}^*\,(\sigma_y \otimes \sigma_y)$. However, similarly to the von Neumann entropy, to calculate the concurrence, the entire states density operator is needed. This will then require full state tomography, a measurement intensive process. To avoid this, entanglement witnesses can be used, which looks for non-classical correlations between the two particles. In this way, any measured entanglement is confirmed to be between the two particles and not one particle and its environment. Such an entanglement witness $\mathscr{W}(\hat{\rho})$ can be defined such that it has the property that it evaluates to greater than 1 only if $\hat{\rho}$ is entangled. It is important to note that the converse is not true. That is, if it is not greater than 1, it does not imply anything about $\hat{\rho}$. Furthermore, such witnesses need to be created to detect the specific entangled state, which can be difficult in general. However, due to the simple nature of the final state, a suitable witness was found [4] to be

$$\mathscr{W} = \left| \left\langle \sigma_x^{(1)} \otimes \sigma_z^{(2)} \right\rangle - \left\langle \sigma_y^{(1)} \otimes \sigma_y^{(2)} \right\rangle \right|, \tag{2.16}$$

which is sufficient for discriminating the entanglement as it is expected to develop in the tabletop experiment. It also only requires two sets of measurements for each particle

2.5 Assumptions Underpinning QGEM

With all this, it is now possible to more clearly articulate the assumptions inherently underlying the QGEM experiment.

- **Locality of physical interactions:** One of the pillars of quantum field theory is the assumption of locality. All the interactions are local at both classical and at a quantum level. In the context of gravity, the local interaction is expected to be given by:

$$\kappa h_{\mu\nu} T^{\mu\nu} \tag{2.17}$$

where $\kappa = \sqrt{8\pi G}$, $G = \hbar/M_p^2$ is Newton's constant and $M_p \sim 10^{19}$GeV. The energy momentum tensor of matter is given by $T_{\mu\nu}$. Note that i am now including $kappa$ as a prefactor rather than absorbing it into the definition of $h_{\mu\nu}$ to demonstrate how in the context of RQFT it can be viewed as the source of the coupling strength. The metric perturbation around Minkowski background is

$$g_{\mu\nu} = \eta_{\mu\nu} + \kappa h_{\mu\nu}\,, \tag{2.18}$$

where $\eta_{\mu\nu}$ is the Minkowski metric, and $|\kappa h_{\mu\nu}| \ll 1$, in order to maintain the linearity. The concept of locality is also an essential criteria from the perspective of quantum information and quantum entanglement. In particular, under Local Operations and Classical Communications (LOCC), the two particles exchanging only classical energy momentum will not lead to enhancement in entanglement. Note that while LOCC is used as a principle to define mixed state entanglement [81, 82], it can be easily *proved* when we start from an unentangled state of two states (the interferometric masses in this case).

Recently, there has been a resurgent interest towards understanding non-local field theories [83–85], note these are *not* action at a distance theories. One

of the features of a non-local theory is that it does not have a point support [84, 86, 87]; therefore it is very helpful towards ameliorating some of the singularities in nature, such as point singularity due to gravitational $1/r$ potential.

The non-local theories arise in many contexts in quantum gravity, in string theory, the notion of point objects are replaced by strings and branes [88], Dynamical triangulation [89] and loop quantum gravity [90] exploits Wilson operators, which are inherently non-local. The string field theory introduces non-locality at the string scale, for a review [91], and infinite derivative ghost free theory of gravity (IDG) [85], which does not introduce any instability around a given background, is motivated from string field theory [92–94]. Especially in string field theory and in IDG, the non-locality appears only at the level of interactions.

As an alternative to local gravitational interaction, I have included below (Section 2.6) an overview of the interaction when assuming non-local IDG and explore the entanglement properties. Thus a certain amount of locality is assumed from the knowledge of physical interactions in the observed regimes.

- **Linearized gravity:** The above analysis always starts by working in a regime of weak-field gravity, linearized around the Minkowski background. This also means that the gravitational potential is always bounded below unity. In fact, below the millimetre scale, there is currently no direct constraint on Newtonian $1/r$ potential [95]. Work is ongoing to explore this regime, with the general focus on constraining a Yukawa type gravitational potential, which also depends on the strength of the Yukawa interaction [95–97]. The experiment will be undertaken in a regime of roughly ≥ 10 micrometres, and for the masses under consideration, the gravitational interaction is indeed weak. Thus the assumption that gravity is only being probed in the linearized regime is reasonable. This minimum distance of > 100 micrometres ensures the Casimir interaction is weaker than that of the gravitational interaction, see [4, 80].

- **A reasonable definition of a classical field:** It is finally necessary to clarify what we mean by a “classical" field. Disagreements on this definition can, of course, result in a disagreement as to whether our experiment demonstrates a non-classicality. Here, I have defined a classical field to be an entity which, with general probabilities P_j has fixed (unique) values $h^j_{\mu\nu}$ at each point of space-time. While I have used a tensor field in the definition, it could alternatively be a scala or spinor. Of course, a special case of that is when there is no probabilistic nature to the field at all – the field just has the one value $h_{\mu\nu}$. Furthermore, the field should also follow the classical equations of motion, that is, on-shell behaviour. It is perhaps worth emphasising that the statistical nature of something does not make it quantum (think of a classical dice) – quantum comes with the possibility to go beyond statistical mixtures of field configurations to coherent superpositions of field configurations. Additionally, it is assumed that a classical field means that there is no Hilbert space for the field. Thus, even joint quantum states of fields with other (say, matter) systems is disallowed, i.e., states of the form $\sum_j \sqrt{P_j}|j\rangle|h^j_{\mu\nu}\rangle$ are *not* allowed. Only allowed joint states of quantised matter and classical field are the probability distributions P_j of configurations $\{|j\rangle\langle j|, h^j_{\mu\nu}\}$, where $h^j_{\mu\nu}$ is a tensor for each point in space-time, but *not* an operator-valued quantity. Here we are defining a classical field as, for example, used by Feynman during his 1957 debate with other researchers on the quantum nature of gravity [63] “... if I have an amplitude for a field, that is what I would define as a quantised field."

2.6 Non-Local Gravity

Here I present a proposed post-Newtonian model for gravity which appears to violate one of the key assumptions outlined above, specifically that of locality. The model for gravity known as Infinite Derivative Gravity (IDG) predicts a non-local region in the immediate vicinity of a mass within which the gravitational potential is constant. Importantly outside this region the gravitational potential acts as described above. This will show how outside the non-local region, a quantum me-

diator may still entangle the masses. Furthermore, if such a non-local region exists, it may be characterised through the results found in such an experiment.

The entanglement experiment protocol could also be used to probe the nature of gravity at short distances. The most general quadratic action in 4 dimensions, which is invariant under parity and also torsion-free is given by [85, 98]:

$$\begin{aligned} S = \quad & \frac{1}{16\pi G}\int d^4x\sqrt{-g}\,\{\mathscr{R}+\beta\,(\mathscr{R}\mathscr{F}_1(\Box_s)\mathscr{R} \\ & +\mathscr{R}_{\mu\nu}\mathscr{F}_2(\Box_s)\mathscr{R}^{\mu\nu}+\mathscr{R}_{\mu\nu\rho\sigma}\mathscr{F}_3(\Box_s)\mathscr{R}^{\mu\nu\rho\sigma})\}\,, \end{aligned} \tag{2.19}$$

where $\Box_s = \Box/M_s^2$ and M_s is considered as the fundamental scale of non-locality, which in the context of string theory corresponds to the string scale. The three gravitational form-factors $\mathscr{F}_i(\Box_s)$ are covariant functions of the d'Alembertian and can be uniquely determined around the Minkowski background [85, 99]. Setting $\mathscr{F}_3(\Box_s) = 0$, without loss of generality up to quadratic order in the metric perturbation around the flat background, the massless spin-2 graviton can be kept as the only dynamical degree of freedom by imposing the following condition: $2\mathscr{F}_1(\Box_s) = -\mathscr{F}_2(\Box_s)$ around the Minkowski background, as shown in Ref.[85].

Expanding around the Minkowski background, $g_{\mu\nu} = \eta_{\mu\nu} + \kappa h_{\mu\nu}$, gives

$$S = \frac{1}{4}\int d^4x\, h_{\mu\nu}\,(1-\mathscr{F}_1(\Box_s)\Box_s)\mathscr{O}^{\mu\nu\rho\sigma}\,h_{\rho\sigma} + \mathscr{O}(\kappa h^3). \tag{2.20}$$

Following the previous procedure, inverting the kinetic operator and taking the saturated and gauge independent part yields [79, 85]

$$\Pi_{\mu\nu\rho\sigma}(k) = \frac{1}{1+\mathscr{F}_1(k)k^2/M_s^2}\left(\frac{\mathscr{P}^2_{\mu\nu\rho\sigma}}{k^2} - \frac{\mathscr{P}^0_{s,\mu\nu\rho\sigma}}{2k^2}\right), \tag{2.21}$$

where $\mathscr{P}^2/k^2 - \mathscr{P}^0_s/2k^2$ is the graviton propagator. Note that in order not to introduce any extra dynamical degrees of freedom other than the massless spin-2 graviton, it is necessary to require that the function $1+\mathscr{F}_1(k)k^2/M_s^2$ does not have any zeros. This can be achieved by defining it as an exponential of an entire

function[85]:

$$1+\mathscr{F}_1(k)\frac{k^2}{M_s^2}=e^{\gamma(k^2/M_s^2)}, \tag{2.22}$$

with the simplest option giving $\gamma(k^2)=k^2/M_s^2$, see also Ref. [100, 100, 101] for other examples. In all these examples, the short distance behaviour becomes soft and in the infrared, the gravitational potential matches that of Newtonian prediction. The scattering diagram can now be computed. The key difference from a local gravitational theory is that now the existence of a new scale, M_s, which determines the interaction at short distances. The quantum aspects of the above action Eq.(2.19) has also been studied in [102, 103], where the spreading of the quantum wave packet has been studied in presence of self gravitational potential and the results have been compared that of a local theory of general relativity. Furthermore, non-local quantum mechanics has been studied widely before in [104–107].

The gravitational potential can be computed by integrating all the momenta of the off-shell graviton, assuming the two vertices are non-relativistic. Essentially, taking the T^{00} components only, and with modified graviton propagator, yields:

$$\begin{aligned}\Phi(r) &= -\kappa^2\int\frac{d^3|\vec{k}|}{(2\pi)^3}T_1^{00}(k)\Pi_{0000}(k)T_2^{00}(-k)e^{i\vec{k}\cdot(\vec{r})}\\ &= -\frac{\kappa^2 m}{2}\int\frac{d^3|\vec{k}|}{(2\pi)^3}\frac{e^{-\vec{k}^2/M_s^2}}{\vec{k}^2}e^{i\vec{k}\cdot(\vec{r})},\\ &= -\frac{Gm}{r}\mathrm{Erf}\left(\frac{M_s r}{2}\right).\end{aligned} \tag{2.23}$$

As such, when $r<2/M_s$, the error function increases linearly with r, which cancels the denominator. Therefore at short distances, for $r<2/M_s$, the gravitational potential becomes constant and given by

$$\Phi(r)\sim\frac{GmM_s}{\sqrt{\pi}}. \tag{2.24}$$

When $r>2/M_s$, the error function approaches ±1, and therefore the potential recovers the standard Newtonian potential, $-Gm/r$, as seen in Fig 2.2. The force

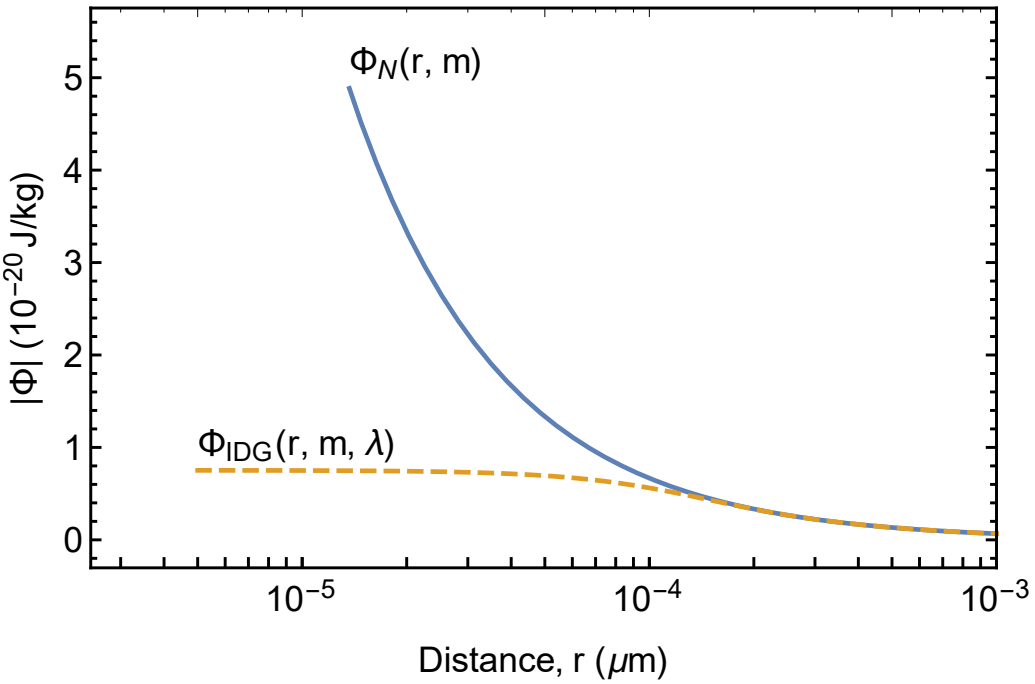

Figure 2.2: Potential energy per unit test mass as generated by a $m = 10^{-14}$ kg source mass for both the standard Newtonian potential (Φ_N) and the modified infinite derivative gravity potential (Φ_{IDG}). The non-local parameter for Φ_{IDG} was set to $M_s = 0.004$ which corresponds to a non-local range $\lambda = 5 \times 10^{-5}$ m.

between the masses is given by

$$F(r) = -\frac{Gm^2}{r^2}\left[\text{Erf}\left(\frac{rM_s}{2}\right) - \frac{e^{-r^2M_s^2/2}M_s r}{\sqrt{\pi}}\right], \tag{2.25}$$

which recovers the Newton's gravitational force Law $-Gm^2/r^2$ for $r > 2/M_s$, while for $r < 2/M_s$, the force vanishes linearly,

$$F(r) \sim -\frac{Gm^2M_s^3}{6\sqrt{\pi}}r. \tag{2.26}$$

thus the gravitational interaction weakens at short distances. It is this behaviour which ameliorates the point like singularity within ghost free[1] IDG.

Since the entanglement phase depends on the potential, at short distances ($r < 2/M_s$) the gravitational potential approaches a constant, and the masses can be said

[1]Ghost free refers to the lack of support for solutions with no minimum energy.

to be within the non-local region. It has also been shown that non-locality never exceeds beyond the non-local scale of M_s, see for instance [108–112]. Therefore, if the two superposed masses are well inside the radius of $r < 2/M_s$, the entanglement phase which is proportional to the gradient of the potential will linearly go to zero at short distances. This has indeed very intriguing repercussions for the entanglement phase. The non-local interaction tends to keep the two states almost separable. This serves as an interesting example of how non-local interactions can alter the quantum behaviour of the many-body system. However, for $r > 2/M_s$, the entanglement phase is the same as that of general relativity as presented above.

The entanglement witness experiment results can be quantified by the two parameters $\Delta\phi_{LR}$ and $\Delta\phi_{RL}$ which can be compared for the two gravitational interactions presented. For an experimental set-up involving 10^{-14} kg masses, 2.5×10^{-4} m superpositions and a minimum separation of 2×10^{-4} m, assuming standard Newtonian gravity, $\Delta\phi_{LR} = -0.125$ rad and $\Delta\phi_{RL} = 0.439$ rad, whereas with IDG one would expect $\Delta\phi_{LR} = -0.125$ rad and $\Delta\phi_{RL} = 0.435$ rad, for $M_s = 0.004$ eV. This translates to an expected entanglement witness value $\mathscr{W} = 1.223$ with IDG compared to $\mathscr{W} = 1.224$ for standard Newtonian gravity. As such, there would be a slight change in the result. However, as the experiment is conducted outside the non-local region, no significant change would be expected. Thus all conclusions still hold, even with the restrained breaking of the local gravity assumption. In fact, with such a small change in the phase, it is unlikely such a modification would be noticed in such an experiment

Chapter 3

Inevitability of Entanglement in Quantum Theories of Gravity

In this chapter I will explore the basic premise that if gravity is fundamentally a quantum force, then any pair of objects which are in non-degenerate gravitational energy eigenstates as sourced by one another should be entangled. This represents an as yet unfinished project in which I attempt to gain insight into the the behaviour of two simple quantum mechanical systems interacting through a weak quantum gravity. In this chapter I will analysed a series of toy models before presenting any insights gained from and limitations of the model. In general this corresponds to considering the wavefunctions of two gravitationally-interacting masses in a discritised spatial basis as shown in Figure 3.1.

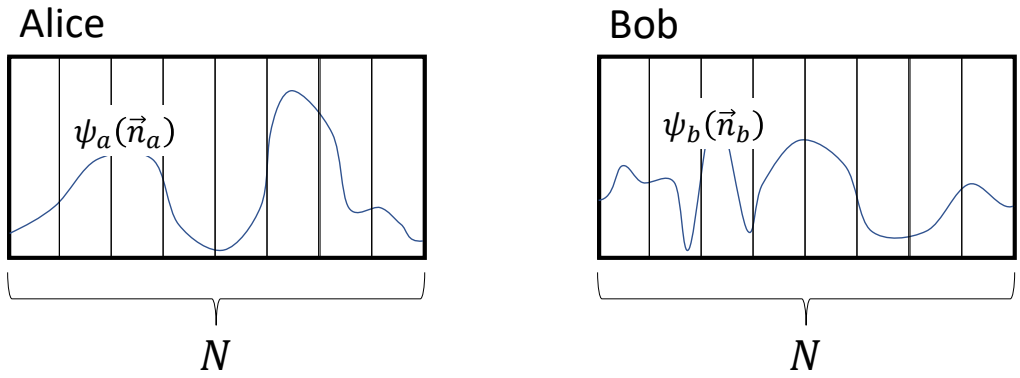

Figure 3.1: Example system to be considered throughout this chapter. Here the wave function of two particles a and b (potentially controlled by Alice and Bob) are binned into N discretise position basis states.

Throughout this chapter I will characterise the entanglement between two masses using the von Neumann entropy as discussed in Section 1.2.

3.1 Flat Distribution, No Dynamics

For the initial toy model I will consider two masses with a distance r_0 between their centre of mass, with some characteristic spread σ_x. I will discretise the wave packets into N equally spread, equally weighted states. The systems dynamics will also be ignored for simplicity. The joint state after interacting for a time t will therefore be

$$|\Psi\rangle = \frac{1}{N}\sum_{a,b}^{N} e^{i\phi_{a,b}t} \left|x_{1,a}\right\rangle \left|x_{2,b}\right\rangle \tag{3.1}$$

where

$$\begin{aligned}\phi_{a,b} &= \frac{Gm_1m_2}{\hbar x_{ab}} && (3.2)\\ &= \frac{Gm_1m_2}{\hbar x_{ab}} && (3.3)\\ &= \frac{Gm_1m_2}{\hbar\left(r_0 - \sigma_x\frac{a-b}{N-1}\right)} && (3.4)\end{aligned}$$

The states density matrix, $\hat{\rho}$ will then be

$$\begin{aligned}\hat{\rho} &= |\Psi\rangle\langle\Psi| && (3.5)\\ &= \frac{1}{N^2}\sum_{a,b,c,d}^{N} e^{i\frac{Gm_1m_2t}{\hbar}\left(\frac{1}{\left(r_0-\sigma_x\frac{a-b}{N-1}\right)}-\frac{1}{\left(r_0-\sigma_x\frac{c-d}{N-1}\right)}\right)} \left|x_{1,a}\right\rangle\left\langle x_{1,c}\right| \otimes \left|x_{2,b}\right\rangle\left\langle x_{2,d}\right| && (3.6)\end{aligned}$$

Now as I am characterising the entanglement using the von Neumann Entropy for the reduced density matrix (which I will in general refer to as simply the entropy), I need to trace out one of the particles. To do this I can use

$$\mathbf{Tr}_B\left(\hat{\rho}_{AB}\right) = \sum_{i,j,k,l}^{N} c_{i,j,k,l}\left|a_i\right\rangle\left\langle a_j\right| \otimes \langle b_l|b_k\rangle \tag{3.7}$$

and the orthonormality of the position basis states $\{|x_{i,a}\rangle\}$. The reduced density matrix will then be

$$\mathbf{Tr}_2(\hat{\rho}) = \frac{1}{N^2}\sum_{a,b,c}^{N} e^{i\frac{Gm_1m_2t}{\hbar}\left(\frac{1}{\left(r_0-\sigma_x\frac{a-b}{N-1}\right)}-\frac{1}{\left(r_0-\sigma_x\frac{c-b}{N-1}\right)}\right)}\left|x_{1,a}\right\rangle\left\langle x_{1,c}\right| \tag{3.8}$$

from which the entropy can be calculated. The resulting entropy scaling with N was calculated numerically and is shown in Figures 3.2 and 3.3. These show that outside of the $N = 2$ case, the entropy scaling at long time appears to be highly chaotic. The short time behaviour however appears to be exhibiting logarithmic growth, although this quickly breaks down as the entropy approaches its maximum value. This suggests that even for extremely simplified systems, with no dynamics outside of phase evolution, and a flat spatial distribution, the entropy development appears highly chaotic as shown in Figure 3.3

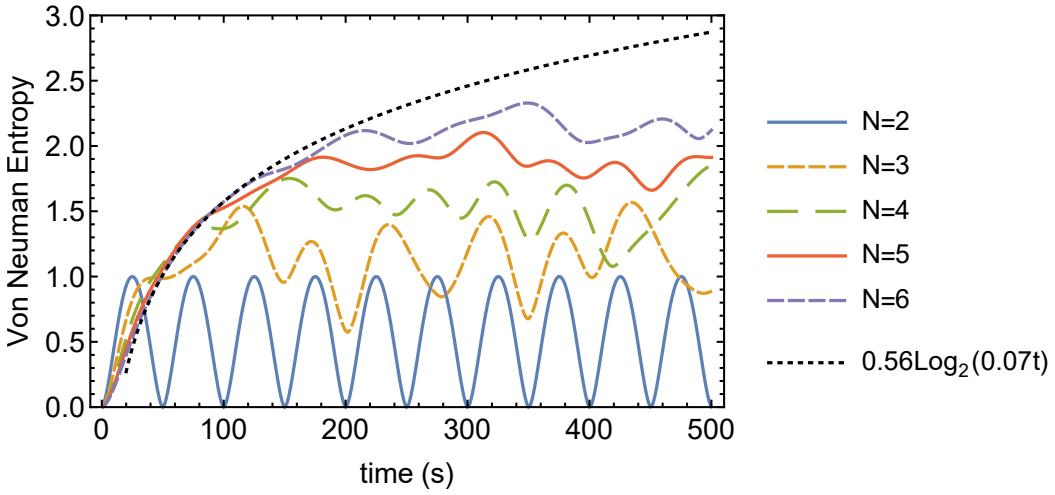

Figure 3.2: von Neumann Entropy of the reduced density matrix for $N \in [2,6]$ for a centre of mass wavepacket separation of 4.5×10^{-14}m, a total wavepacket spread of 2.5×10^{-4}m and 10^{-14}kg masses. This also shows a crude Logarithmic fit to estimate the larger and potentially infinite dimensional scaling.

By extending to higher N, information about the behaviour in the continuous regime can be gained. Figure 3.4 shows the entropy scaling into higher N as well as higher dimensional systems. As N becomes large the small time behaviour becomes completely independent of N, this suggests it may be approximating the entropy for continuous spatial degrees of freedom accurately. This also suggest a minimum fundamental length scale would not be visible by simply looking at the

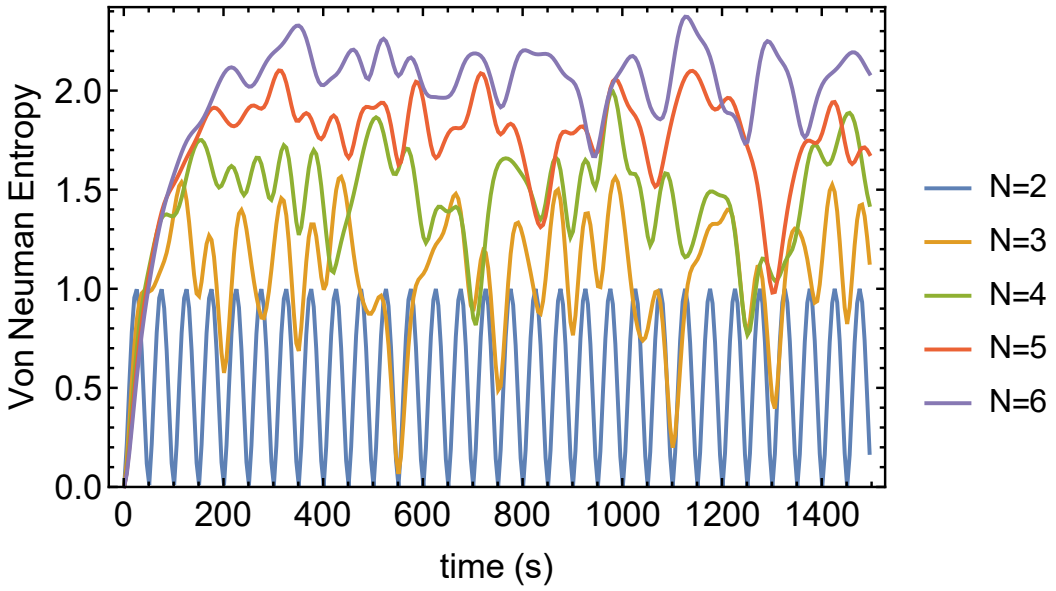

Figure 3.3: von Neumann Entropy of the reduced density matrix showing the long time behaviour for a centre of mass wavepacket separation of 4.5×10^{-14}m, a total wavepacket spread of 2.5×10^{-4}m and 10^{-14}kg masses.

entanglement growth rate. The behaviour in higher dimensional systems appears to be qualitatively equivalent to a single dimensional system.

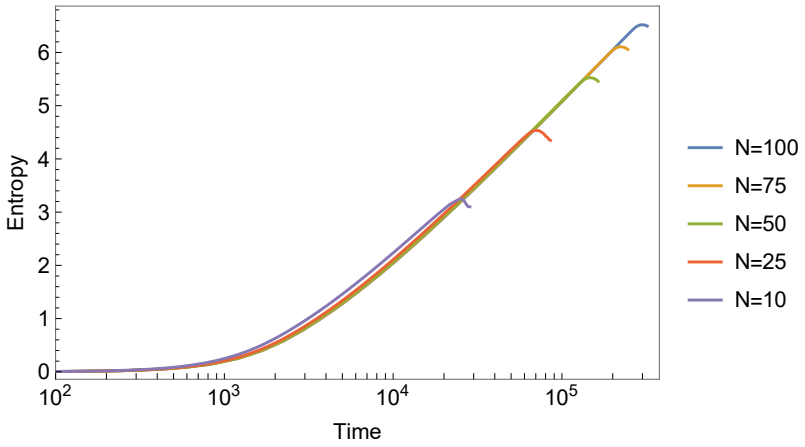

(a) $1-D$ wave function.

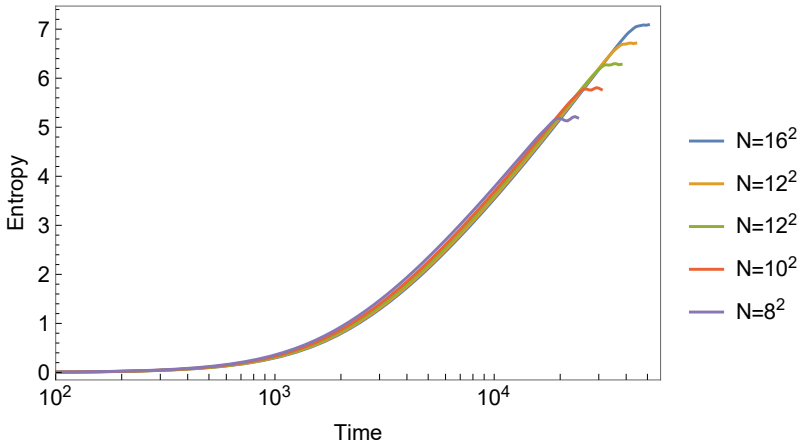

(b) $2-D$ wave function.

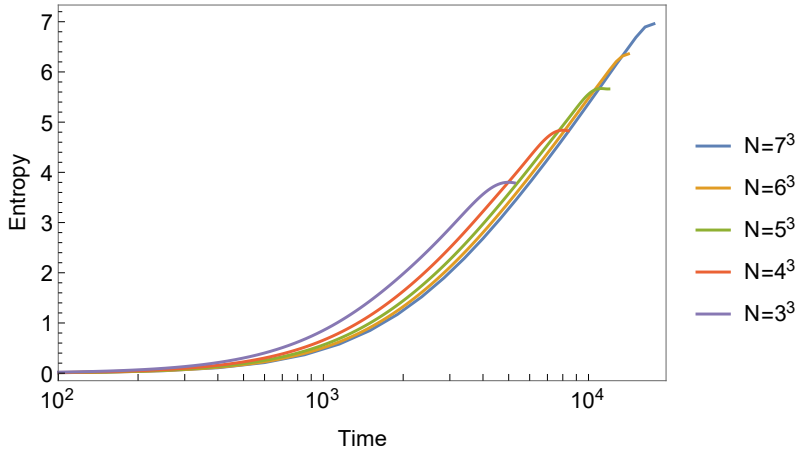

(c) $3-D$ wave function.

Figure 3.4: von Neumann entropy scaling with time in 1, 2 and 3 dimensions with uniform spatial spread. Here the only the qualitative behaviour is of interest and so the time is in arbitrary time units. The entropy growth appears logarithmic. Here N denotes the total number of discrete spatial states which the particles are separated into. As only the scaling is of interest, here $c = \hbar = G = m_1 = m_2 = 1$, and the total spread of the wave functions, $\sigma_x = 1$ with a centre of mass separations of $r_0 = 10$.

3.2 Gaussian Toy Model

Here I will consider improving the toy model slightly. I will still be neglecting the motion of the particle, allowing the interaction to only effect the phase, but here considering the wave packets to have a Gaussian distribution as shown in Figure 3.5. So I am looking to approximate

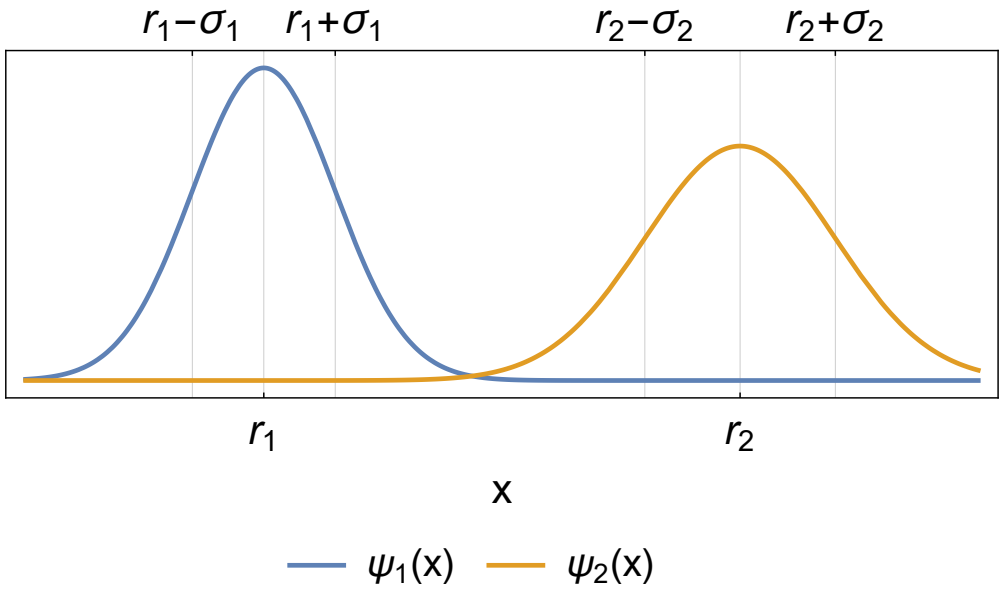

Figure 3.5: Example of two arbitrary Gaussian state distributions.

$$\psi_i(x) = \frac{1}{\sqrt{2\pi\sigma_i^2}} e^{-\frac{(x-r_i)^2}{2\sigma_i^2}} \tag{3.9}$$

as N discrete components forming the state

$$|\Psi\rangle = \sum_{n=1}^{N} |\psi_n\rangle \tag{3.10}$$

where

$$|\psi_n\rangle = \mathcal{N} e^{-\frac{(x_n-r_i)^2}{2\sigma_i^2}} |x_n\rangle \tag{3.11}$$

with $\mathcal{N}$ being the appropriate normalisation factor and for simplicity, I will assume $r_1 = -r_2 = r_0$ and $\sigma_1 = \sigma_2 = \sigma$. While a Gaussian decays but never

becomes zero, I will approximate it as finite, with a total width 2μ, such that $r_0 - \mu \leq x_n \leq r_0 + \mu$ and so $x_n = r_0 + \mu\left(2\frac{n-1}{N-1} - 1\right)$. This will ensure that the two wave packets never actually overlap. The normalisation factor is given by $\mathscr{N} = \left(\sqrt{\pi}\sigma\right)^{-1/2}\sqrt{\frac{2\mu}{N-1}}$ provided $\frac{2\mu}{N-1} \ll \sigma$ and $\mu \gg \sigma$. Given that the motion of the particles is ignored, the two particle joint state will be

$$|\Psi_{tot}\rangle = \sum_{n_1,n_2} \phi\left(n_1,n_2\right) f_1(n_1) f_2(n_2) |x_{n_1}\rangle |x_{n_2}\rangle \tag{3.12}$$

where

$$f_i(n_i) = \left(\sqrt{\pi}\sigma_i\right)^{-1/2}\sqrt{\frac{2\mu_i}{N-1}} e^{-\frac{(x_{n_i}-r_0)^2}{2\sigma_i^2}} \tag{3.13}$$

and

$$\phi\left(n_1,n_2\right) = e^{-\frac{iGm_1m_2t}{\hbar}\left|x_{n_1}-x_{n_2}\right|^{-1}} \tag{3.14}$$

is the phase interaction. The reduced density operator for the first particle is

$$\rho_1\left(n,n'\right) = \sum_{n_2} \phi\left(n,n_2\right)\phi^*\left(n',n_2\right) f_1(n) f_1^*(n') \left|f_2(n_2)\right|^2 |x_n\rangle\langle x_{n'}|. \tag{3.15}$$

This was evaluated in Mathematica and is shown in Figure 3.6. This shows how the entropy scales with time and N, the number of discrete states used to approximate the continuous Gaussian. Once again, the entropy initially scales logarithmically with time. In fact, it appears that the modified spatial distribution has no qualitative impact on the entanglement. As N increases it can be seen that the entropy appears to reach some maximal bound, before settling into a slightly lower value. For larger N, the entropy becomes less chaotic and appears to reach a steady state value. This is likely a result of the larger number of pairs of states which entangle and unentangle with time. For larger N this will lead to the total entanglement reaching some steady state, average value. While there is a physical limit on the maximum entropy in a discrete system, given by $\log_2(N)$, this is not the bound seen in Figure 3.6a. Figure 3.6b shows the entropy scaled by the maximum obtainable entropy so the maximum relative entropy would be 1 in a maximally entangled state. While for larger N, the entropy does approach 1, thus saturating the entanglement

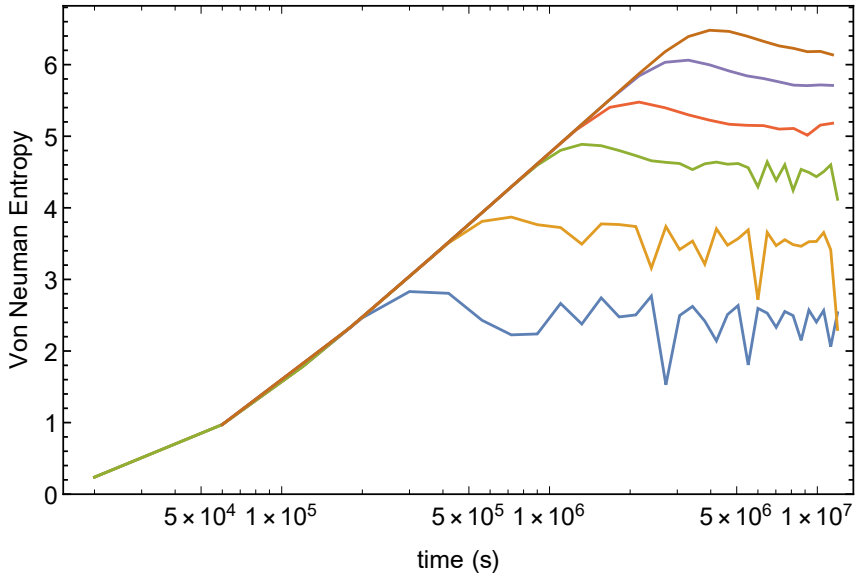

(a) Von-Neumann entropy with time.

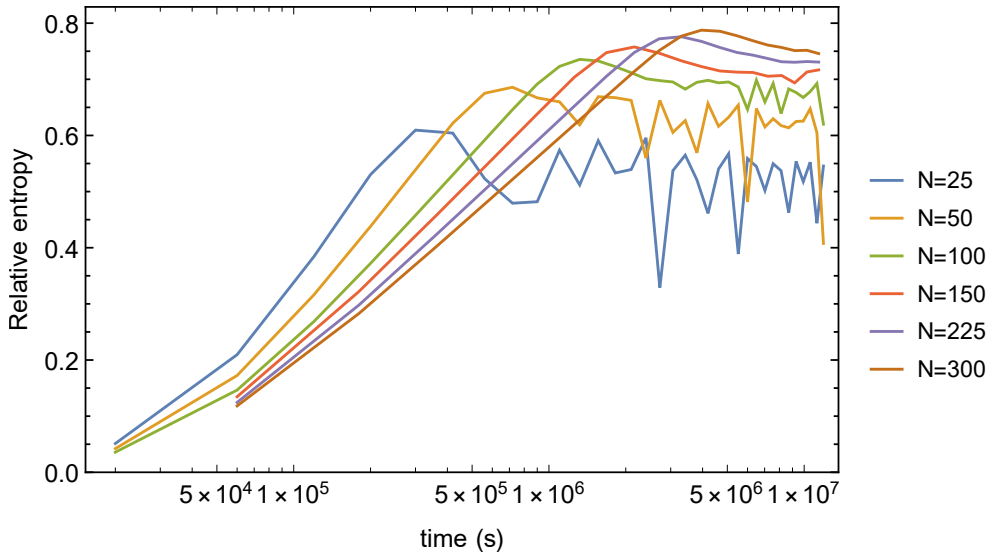

(b) Von-Neumann entropy with time normalised by maximum entropy obtainable.

Figure 3.6: Von-Neumann Entropy for two interacting Gaussian states approximated as N discrete states. These are all for scalled units with $\hbar = G = m_1 = m_2 = 1$, $\sigma_1 = \sigma_2 = 0.1$ and $\mu_1 = \mu_2 = 0.4$ for the two wave packets centred at $r_{1/2} = +/-5$.

bound, it is unclear whether it will ever reach it.

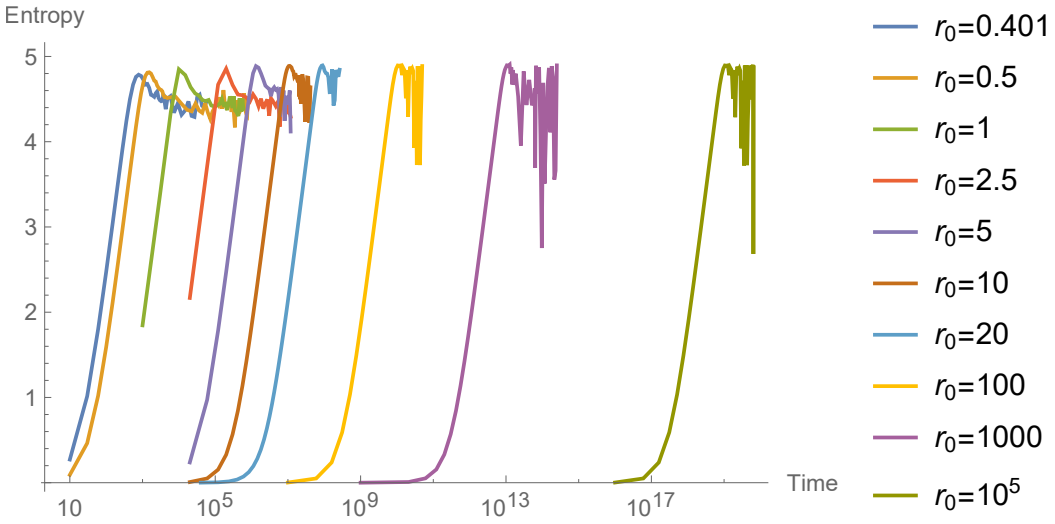

Figure 3.7: von Neumann Entropy of the reduced density matrix for varying wave packet separation. Here $\hbar = G = m_1 = m_2 = 1$, $\sigma_1 = \sigma_2 = 0.1$, $\mu_1 = \mu_2 = 0.4$ and $N = 100$. The two wave packets are centred at $r_{1/2} = \pm r_0$.

Surprisingly the relative distance between the two wave packets also does not appear to qualitatively change the manner in which they become entangled. This can be seen in Figure 3.7 which shows how the entropy growth changes as the wave packet separation varies. The distance between the two particles appears to only scale the time it takes for entanglement to develop. It does not however modify the way in which it develops, or the maximum amount of entanglement. It is also of note that I have considered wave packet separations to the point at which the two particles are as close as they reasonably can be without any overlap (note $\mu = 0.4$ and $r_0 = 0.401$). Furthermore, the minimum of the fluctuations appear to begin to resemble the sinusoidal behaviour seen for $N = 2$. It could be possible that for sufficiently large separations, the entropy behaviour could match that for $N = 2$. This also may be the result of the numerical method used to plot the results, with the full entropy curves showing higher frequency fluctuation patterns, only some of which are appearing in any given result.

3.3 A More Complete Model

While the results so far have been intriguing, they're only of very limited applicability given the rather limiting approximations which have been used to calculate the results. As such, I then sort to solve for the full dynamics. The first method used to achieve this was to treat the problem non-relativistically. It is then possible to simply employ the known solutions to the hydrogen atom with the appropriate modification to the coulomb potential. While this was a satisfactory method for computing the time evolution for the joint state, I was unable to use it to gain any insights. Given the highly localised and non-uniform nature of the two particle system being modelled, it was found to be too computationally intensive to calculate a sufficient number of overlaps between the eigenstates and the initial state.

To simplify this problem and the solution, I instead return to modelling a one dimensional system. This time using an approximate of the time evolution for such a system.

Starting with the full Hamiltonian of the system:

$$\hat{H}_{\text{tot}} = \frac{-\hbar^2}{2m_1}\nabla_1^2 + \frac{-\hbar^2}{2m_2}\nabla_2^2 - \frac{m_1 m_2 G}{|\hat{r}_1 - \hat{r}_2|} \tag{3.16}$$

which can be recast into centre of mass coordinates setting $\hat{R} = \frac{m_1\hat{r}_1 + m_2\hat{r}_2}{m_1+m_2}$ and $\hat{r} = \hat{r_1} - \hat{r}_2$. I will also define the total and reduced mass as $M = m_1 + m_2$ and $\mu = \frac{m_1 m_2}{M}$ as introduced above. The total Hamiltonian can then be written

$$\hat{H}_{\text{tot}} = \frac{-\hbar^2}{2M}\nabla_R^2 + \frac{-\hbar^2}{2\mu}\nabla_r^2 - \frac{\mu M G}{|\hat{r}|} = \hat{H}_R + \hat{H}_r. \tag{3.17}$$

This leaves two uncoupled equations which can be solved independently. I will assume the solutions are separable, specifically that $\Psi(R,r,t) = \psi(R,t)\psi(r,t)$.

$\hat{H}_R$ simply corresponds to free evolution of the wave packet and will be covered later. The other coordinate corresponds to the particle moving in a central potential. To determine the evolution I will seek to calculate the time evolution operator $\hat{U}(t)$. Furthermore, to simplify the calculation I will assume that $\langle\hat{r}_1\rangle > \langle\hat{r}_2\rangle$ and $|\hat{r}| \approx \vec{r}_0 + \hat{\delta}r$ where at all times (at least for all times that the time evolution operator I am

seeking to calculate is used) $\langle\hat{\delta}r\rangle \ll |\vec{r}|$ such that I can write

$$\frac{1}{|\hat{r}|} \approx \frac{1}{r_0}\left(1+\frac{\hat{\delta}r}{r_0}+\frac{\hat{\delta}r^2}{r_0^2}\right) \tag{3.18}$$

3.3.1 1-D Time Evolution Operator

The Hamiltonian for the r coordinate, once expanded using Eq. 3.18, becomes

$$\begin{aligned}\hat{H}_r =& \frac{-\hbar^2}{2\mu}\nabla_r^2 - \frac{\mu MG}{|\hat{r}|} \\ \approx& \frac{\hat{p}_r^2}{2\mu} - \frac{\mu MG}{r_0}\left(1+\frac{\hat{\delta}r}{r_0}+\frac{\hat{\delta}r^2}{r_0^2}\right).\end{aligned} \tag{3.19}$$

Before proceeding to calculate the time evolution operator it is necessary to verify the commutation relations. In the original co-ordinates $\left[\hat{r}_i,\hat{p}_j\right] = i\hbar\delta_{ij}$, now in the converted units we have $[\hat{r},\hat{p}_r] = i\hbar$ and $\left[\hat{R},\hat{p}_R\right] = i\hbar$ and finally these commutation relations will also hold for the new $\hat{\delta}r$ operator, that is $\left[\hat{\delta}r,\hat{p}_r\right] = i\hbar$. The time evolution operator for the r wave function over some time t small enough that the wave packets do not move a significant distance towards one another is

$$\begin{aligned}\hat{U}_r(t) =& e^{\frac{-it}{\hbar}\left(\frac{\hat{p}_r^2}{2\mu}-\frac{\mu MG}{r_0}\left(1+\frac{\hat{\delta}r}{r_0}+\frac{\hat{\delta}r^2}{r_0^2}\right)\right)} \\ =& e^{\frac{i\mu MGt}{\hbar r_0}}\, e^{\frac{-it}{\hbar}\left(\frac{\hat{p}_r^2}{2\mu}-\frac{\mu MG}{r_0}\left(\frac{\hat{\delta}r}{r_0}+\frac{\hat{\delta}r^2}{r_0^2}\right)\right)} \\ =& e^{\frac{i\mu MGt}{\hbar r_0}}\, e^{\frac{-it}{\hbar}\left(\hat{P}+\hat{X}\right)}\end{aligned} \tag{3.20}$$

where $\hat{P} = \frac{\hat{p}_r^2}{2\mu}$ and $\hat{X} = -\frac{\mu MG}{r_0}\left(\frac{\hat{\delta}r}{r_0}+\frac{\hat{\delta}r^2}{r_0^2}\right)$. Using the Baker-Campbell-Hausdorff (BCH) expansion:

$$\begin{aligned}e^{a\left(\hat{A}+\hat{B}\right)} =& e^{a\hat{A}}e^{a\hat{B}}e^{\frac{-a^2}{2}\left[\hat{A},\hat{B}\right]}e^{\frac{a^3}{6}\left(2\left[\hat{B},\left[\hat{A},\hat{B}\right]\right]+\left[\hat{A},\left[\hat{A},\hat{B}\right]\right]\right)} \\ &\times e^{\frac{a^4}{24}\left(\left[\left[\left[\hat{A},\hat{B}\right],\hat{A}\right],\hat{A}\right]+3\left[\left[\left[\hat{A},\hat{B}\right],\hat{A}\right],\hat{B}\right]+3\left[\left[\left[\hat{A},\hat{B}\right],\hat{B}\right],\hat{B}\right]\right)}\end{aligned} \tag{3.21}$$

As such it is necessary to calculate the various commutators, for reference I will use the commutation identities:

$$\left[\hat{A},\hat{B}\hat{C}\right] = \left[\hat{A},\hat{B}\right]\hat{C} + \hat{B}\left[\hat{A},\hat{C}\right] \tag{3.22}$$

$$\left[\hat{A}\hat{B},\hat{C}\hat{D}\right] = \hat{A}\left[\hat{B},\hat{C}\right]\hat{D} + \left[\hat{A},\hat{C}\right]\hat{B}\hat{D} + \hat{C}\hat{A}\left[\hat{B},\hat{D}\right] + \hat{C}\left[\hat{A},\hat{D}\right]\hat{B} \tag{3.23}$$

And so

$$\begin{aligned}
\left[\hat{X},\hat{P}\right] &= \left[-\frac{\mu MG}{r_0}\left(\frac{\hat{\delta}r}{r_0} + \frac{\hat{\delta}r^2}{r_0^2}\right), \frac{\hat{p}_r^2}{2\mu}\right] \\
&= -\frac{MG}{2r_0^2}\left[\hat{\delta}r, \hat{p}_r^2\right] - \frac{MG}{2r_0^3}\left[\hat{\delta}r^2, \hat{p}_r^2\right] \\
&= -\frac{MG}{2r_0^2}\left(\left[\hat{\delta}r, \hat{p}_r\right]\hat{p}_r + \hat{p}_r\left[\hat{\delta}r, \hat{p}_r\right]\right)) \\
&\quad -\frac{MG}{2r_0^3}\left(\hat{\delta}r\left[\hat{\delta}r, \hat{p}_r\right]\hat{p}_r + \left[\hat{\delta}r, \hat{p}_r\right]\hat{\delta}r\hat{p}_r + \hat{p}_r\hat{\delta}r\left[\hat{\delta}r, \hat{p}_r\right] + \hat{p}_r\left[\hat{\delta}r, \hat{p}_r\right]\hat{\delta}r\right) \\
&= -\frac{MG}{2r_0^2}\left(i\hbar\hat{p}_r + \hat{p}_r i\hbar\right)) - \frac{MG}{2r_0^3}\left(\hat{\delta}r i\hbar\hat{p}_r + i\hbar\hat{\delta}r\hat{p}_r + \hat{p}_r\hat{\delta}r i\hbar + \hat{p}_r i\hbar\hat{\delta}r\right) \\
&= -\frac{i\hbar MG}{r_0^2}\hat{p}_r - \frac{2i\hbar MG}{r_0^3}\hat{\delta}r\hat{p}_r - \frac{\hbar^2 MG}{r_0^3},
\end{aligned} \tag{3.24}$$

$$\begin{aligned}
\left[\hat{P},\left[\hat{X},\hat{P}\right]\right] &= \left[\frac{\hat{p}_r^2}{2\mu}, \left[-\frac{\mu MG}{r_0}\left(\frac{\hat{\delta}r}{r_0} + \frac{\hat{\delta}r^2}{r_0^2}\right), \frac{\hat{p}_r^2}{2m}\right]\right] \\
&= \frac{1}{2\mu}\left[\hat{p}_r^2, -\frac{i\hbar MG}{r_0^2}\hat{p}_r - \frac{2i\hbar MG}{r_0^3}\hat{\delta}r\hat{p}_r - \frac{\hbar^2 MG}{r_0^3}\right] \\
&= -\frac{i\hbar MG}{\mu r_0^3}\left[\hat{p}_r^2, \hat{\delta}r\hat{p}_r\right] \\
&= -\frac{2\hbar^2 MG}{\mu r_0^3}\hat{p}_r^2,
\end{aligned} \tag{3.25}$$

and

$$\begin{aligned}\left[\hat{X},\left[\hat{X},\hat{P}\right]\right] =& \left[-\frac{\mu MG}{r_0}\left(\frac{\hat{\delta}r}{r_0}+\frac{\hat{\delta}r^2}{r_0^2}\right),-\frac{i\hbar MG}{r_0^2}\hat{p}_r-\frac{2i\hbar MG}{r_0^3}\hat{\delta}r\hat{p}_r-\frac{\hbar^2 MG}{r_0^3}\right]\\ =&\frac{i\hbar\mu M^2G^2}{r_0^4}\left[\hat{\delta}r,\hat{p}_r\right]+\frac{2i\hbar\mu M^2G^2}{r_0^5}\left[\hat{\delta}r,\hat{\delta}r\hat{p}_r\right]\\ &+\frac{i\hbar\mu M^2G^2}{r_0^5}\left[\hat{\delta}r^2,\hat{p}_r\right]+\frac{2i\hbar\mu M^2G^2}{r_0^6}\left[\hat{\delta}r^2,\hat{\delta}r\hat{p}_r\right]\\ =&-\frac{\hbar^2\mu M^2G^2}{r_0^4}-\frac{4\hbar^2\mu M^2G^2}{r_0^5}\hat{\delta}r-\frac{4\hbar^2\mu M^2G^2}{r_0^6}\hat{\delta}r^2. \end{aligned} \tag{3.26}$$

As such, it is clear this series is not going to terminate. To deal with this I will try to drop the trailing term $\frac{\hat{\delta}r^2}{r_0^2}$. That is, I will set $\hat{P}=\frac{\hat{p}_r^2}{2\mu}$ and $\hat{X}=-\frac{\mu MG}{r_0}\frac{\hat{\delta}r}{r_0}$. The commutation relations are now

$$\begin{aligned}\left[\hat{X},\hat{P}\right] =& \left[-\frac{\mu MG}{r_0}\frac{\hat{\delta}r}{r_0},\frac{\hat{p}_r^2}{2\mu}\right]\\ =&-\frac{MG}{2r_0^2}\left[\hat{\delta}r,\hat{p}_r^2\right]\\ =&-\frac{MG}{2r_0^2}\left(\left[\hat{\delta}r,\hat{p}_r\right]\hat{p}_r+\hat{p}_r\left[\hat{\delta}r,\hat{p}_r\right]\right)\\ =&-\frac{i\hbar MG}{r_0^2}\hat{p}_r, \end{aligned} \tag{3.27}$$

$$\begin{aligned}\left[\hat{P},\left[\hat{X},\hat{P}\right]\right] =& \left[\frac{\hat{p}_r^2}{2\mu},-\frac{i\hbar MG}{r_0^2}\hat{p}_r\right]\\ =&\frac{1}{2\mu}\left[\hat{p}_r^2,-\frac{i\hbar MG}{r_0^2}\hat{p}_r\right]\\ =&0, \end{aligned} \tag{3.28}$$

and

$$\begin{aligned}\left[\hat{X},\left[\hat{X},\hat{P}\right]\right] =& \left[-\frac{\mu MG}{r_0}\frac{\hat{\delta}r}{r_0},-\frac{i\hbar MG}{r_0^2}\hat{p}_r\right]\\ =&\frac{i\hbar\mu M^2G^2}{r_0^4}\left[\hat{\delta}r,\hat{p}_r\right]\\ =&-\frac{\hbar^2\mu M^2G^2}{r_0^4}.\end{aligned} \tag{3.29}$$

and so all higher order commutators will be zero, and the BCH expansion can be truncated. The time evolution operator can thus be written

$$\begin{aligned}\hat{U}_r(t) =&e^{\frac{-\hat{H}_rt}{\hbar}}\\ =&e^{\frac{i\mu MGt}{\hbar r_0}}e^{\frac{-it}{\hbar}\left(\hat{X}+\hat{P}\right)}\\ =&e^{\frac{i\mu MGt}{\hbar r_0}}e^{\frac{-it}{\hbar}\hat{X}}e^{\frac{-it}{\hbar}\hat{P}}e^{\frac{t^2}{2\hbar^2}\left[\hat{X},\hat{P}\right]}e^{-\frac{it^3}{6\hbar^3}\left(2\left[\hat{P},\left[\hat{X},\hat{P}\right]\right]+\left[\hat{X},\left[\hat{X},\hat{P}\right]\right]\right)}\\ =&e^{\frac{i\mu MGt}{\hbar r_0}}e^{\frac{i\mu MGt}{\hbar r_0}\frac{\hat{\delta}r}{r_0}}e^{\frac{-it\hat{p}_r^2}{2\hbar\mu}}e^{-\frac{iMGt^2}{2\hbar r_0^2}\hat{p}_r}e^{-\frac{it^3}{6\hbar^3}\left(2\times0-\frac{\hbar^2\mu M^2G^2}{r_0^4}\right)}\\ =&e^{i\phi}e^{\frac{i\mu MGt}{r_0^2\hbar}\hat{\delta}r}e^{-\frac{iMGt^2}{2r_0^2\hbar}\hat{p}_r}e^{\frac{-it\hat{p}_r^2}{2\mu\hbar}}\end{aligned} \tag{3.30}$$

where $\phi = e^{\frac{i\mu MGt}{\hbar r_0}-\frac{i\mu M^2G^2t^3}{6r_0^4\hbar}}$ will generate an unimportant global phase which can safely ignored. It is thus now necessary to start to consider the mass states to be modelled. In doing this I will make some simplifying assumptions: $m_1 = m_2 = m$, both wave packets will be taken to be Gaussian states centred at $\pm\frac{r_0}{2}$, the two wave packets are initially at rest and their position spreads are equal and small with respect to the centre of mass spread. This last assumption is necessary to ensure we do not need to consider the corrections due to the $\frac{1}{x}$ dependence of the mediating force. This gives the initial state of the two wave packets as

$$\psi_1(x,t=0) = \left(2\pi\sigma^2\right)^{-1/4}e^{-\frac{\left(x_1-\frac{1}{2}r_0\right)^2}{4\sigma^2}} \tag{3.31}$$

$$\psi_2(x,t=0) = \left(2\pi\sigma^2\right)^{-1/4}e^{-\frac{\left(x_2+\frac{1}{2}r_0\right)^2}{4\sigma^2}}. \tag{3.32}$$

and as such the joint state is

$$\begin{aligned}
\Psi(x_1,x_2) &= \left(2\pi\sigma^2\right)^{-1/4}\left(2\pi\sigma^2\right)^{-1/4} e^{-\frac{\left(x_1-\frac{1}{2}r_0\right)^2}{4\sigma^2}} e^{-\frac{\left(x_2+\frac{1}{2}r_0\right)^2}{4\sigma^2}} \\
&= \left(2\pi\sigma^2\right)^{-1/2} e^{-\frac{\left(x_1-\frac{1}{2}r_0\right)^2}{4\sigma^2}-\frac{\left(x_2+\frac{1}{2}r_0\right)^2}{4\sigma^2}} \\
&= \left(2\pi\sigma^2\right)^{-1/2} e^{-\frac{1}{2\sigma^2}\left(x_1^2+x_2^2+x_2r_0-x_1r_0+2\frac{r_0^2}{4}\right)} \\
\implies \Psi(R,r,t=0) &= \left(2\pi\sigma^2\right)^{-1} e^{-\frac{1}{4\sigma^2}\left(\left(R+\frac{r}{2}\right)^2+\left(R-\frac{r}{2}\right)^2+\left(R-\frac{r}{2}\right)r_0-\left(R+\frac{r}{2}\right)r_0+2\frac{r_0^2}{4}\right)} \\
&= \left(2\pi\sigma^2\right)^{-1/2} e^{-\frac{1}{4\sigma^2}\left(2R^2+\frac{r^2}{2}-rr_0+2\frac{r_0^2}{4}\right)} \\
\implies \Psi(\delta r,R,t=0,r_0(\tau)) &= \left(2\pi\sigma^2\right)^{-1/2} e^{-\frac{1}{4\sigma^2}\left(2R^2+\frac{(r_0+\delta r)^2}{2}-(r_0+\delta r)r_0+2\frac{r_0^2}{4}\right)} \\
&= \left(2\pi\sigma^2\right)^{-1/2} e^{-\frac{1}{4\sigma^2}\left(2R^2+\frac{\delta r^2}{2}\right)} \\
&= \left(2\pi\sigma_R^2\right)^{-1/4} e^{-\frac{R^2}{4\sigma_R^2}}\left(2\pi\sigma_r^2\right)^{-1/4} e^{-\frac{\delta r^2}{4\sigma_r^2}} = \psi(R,t)\,\psi(\delta r,t)
\end{aligned} \tag{3.33}$$

where $\sigma_R^2=\frac{\sigma^2}{2}$, $\sigma_r^2=2\sigma^2$. Note that as I have also set $\sigma_1=\sigma_2=\sigma$ to greatly simplify the above. On the left hand side I have written $r_0(\tau)$ as a reminder that here r_0 is a classical number, and a constant, which should be updated each time the evolution is re-calculated for another time step τ, for notational clarity I will cease doing this from now. I will now evaluate the more simple component of the evolution, that for the centre of mass coordinate.

3.3.2 Centre of Mass Evolution

For the centre of mass state, the initial state is

$$\psi(R,t=0) = \left(2\pi\sigma_R^2\right)^{-1/4} e^{-\frac{R^2}{4\sigma_R^2}} \tag{3.34}$$

which we can evolve using the time evolution operator

$$\hat{U}_R(t) = e^{-\frac{it\hat{p}_R^2}{2M\hbar}} \tag{3.35}$$

To do so, we also need the Fourier and inverse-Fourier transforms, defined as

$$f(x) = \frac{1}{\sqrt{2\pi}} \int_{-\infty}^{\infty} F(k) e^{ikx} \mathrm{d}k \tag{3.36}$$

$$F(k) = \frac{1}{\sqrt{2\pi}} \int_{-\infty}^{\infty} f(x) e^{-ikx} \mathrm{d}x \tag{3.37}$$

$$\tag{3.38}$$

where k is the wavenumber, which is related to the momentum by $p = \hbar\, k$. Thus

$$\begin{aligned}
\psi(R,t) =& \hat{U}_R(t)\psi(R,t=0) \\
=& e^{-\frac{it\hat{p}_R^2}{2M\hbar}} \left(2\pi\sigma_R^2\right)^{-1/4} e^{-\frac{R^2}{4\sigma_R^2}} \\
=& \left(2\pi\sigma_R^2\right)^{-1/4} e^{-\frac{it\hat{p}_R^2}{2M\hbar}} \frac{1}{2\pi} \left(\int_{-\infty}^{\infty} \mathrm{d}k \, \left(\int_{-\infty}^{\infty} \mathrm{d}x \, e^{-\frac{x^2}{4\sigma_R^2}} e^{-ikx} \right) e^{ikR} \right) \\
=& (2\pi)^{-1} \left(2\pi\sigma_R^2\right)^{-1/4} \left(\int_{-\infty}^{\infty} \mathrm{d}k \, \left(\int_{-\infty}^{\infty} \mathrm{d}x \, \cos(kx) \, e^{-\frac{x^2}{4\sigma_R^2}} - i\sin(kx) \, e^{-\frac{x^2}{4\sigma_R^2}} \right) e^{ikR} e^{-i\frac{\hbar t k^2}{2M}} \right) \\
=& (2\pi)^{-1} \left(2\pi\sigma_R^2\right)^{-1/4} \left(\int_{-\infty}^{\infty} \mathrm{d}k \, \left(\int_{-\infty}^{\infty} \mathrm{d}x \, \cos(kx) \, e^{-\frac{x^2}{4\sigma_R^2}} \right) e^{ikR} e^{-i\frac{\hbar t k^2}{2M}} \right) \\
=& (2\pi)^{-1} \left(2\pi\sigma_R^2\right)^{-1/4} \left(4\pi\sigma_R^2\right)^{1/2} \left(\int_{-\infty}^{\infty} \mathrm{d}k \, \left(e^{-k^2\sigma_R^2} \right) e^{ikR} e^{-i\frac{\hbar t k^2}{2M}} \right) \\
=& \left(2\pi^2\right)^{-1/2} \left(2\pi\sigma_R^2\right)^{1/4} \left(\int_{-\infty}^{\infty} \mathrm{d}k \, e^{-k^2\left(\sigma_R^2 + i\frac{\hbar t}{2M}\right)} e^{ikR} \right) \\
=& \left(2\pi^2\right)^{-1/2} \left(2\pi\sigma_R^2\right)^{1/4} \left(\pi^{1/2} \left(\sigma_R^2 + i\frac{\hbar t}{2M} \right)^{-1/2} e^{\frac{-R^2}{4\left(\sigma_R^2 + i\frac{\hbar t}{2M}\right)}} \right) \\
=& (2\pi)^{-1/2} \left(2\pi\sigma_R^2\right)^{1/4} \left(\sigma_R^2 + i\frac{\hbar t}{2M} \right)^{-1/2} e^{\frac{-R^2}{4\left(\sigma_R^2 + i\frac{\hbar t}{2M}\right)}} \\
=& \left(2\pi\sigma_R^2 \left(1 + i\frac{\hbar t}{2M\sigma_R^2} \right)^2 \right)^{-1/4} e^{\frac{-R^2}{4\left(\sigma_R^2 + i\frac{\hbar t}{2M}\right)}}
\end{aligned} \tag{3.39}$$

3.3.3 Breathing Mode Evolution

For the breathing mode the initial state is

$$\psi(r,0) = \left(4\pi\sigma_r^2\right)^{-1/2} e^{-\frac{\delta r^2}{4\sigma_r^2}} \tag{3.40}$$

and the time evolution is given by

$$\hat{U}_r(t) = e^{i\phi} e^{\frac{i\mu MGt}{r_0^2\hbar}\hat{\delta r}} e^{\frac{iMGt^2}{2r_0^2\hbar}\hat{p}_r} e^{\frac{-it\hat{p}_r^2}{2\mu\hbar}}. \tag{3.41}$$

Note however, this only holds for short times $t \leq \tau$, then r_0 needs to be updated for the next time step. So for the first time step

$$\begin{aligned}
\psi(\delta r, \tau) =& e^{i\phi} e^{\frac{i\mu MG\tau}{r_0^2\hbar}\hat{\delta r}} e^{-\frac{iMG\tau^2}{2r_0^2\hbar}\hat{p}_r} e^{\frac{-i\tau\hat{p}_r^2}{2\mu\hbar}} \left(2\pi\sigma_r^2\right)^{-1/4} e^{-\frac{\delta r^2}{4\sigma_r^2}} \\
=& e^{i\phi} e^{\frac{i\mu MG\tau}{r_0^2\hbar}\hat{\delta r}} e^{-\frac{iMG\tau^2}{2r_0^2\hbar}\hat{p}_r} e^{\frac{-i\tau\hat{p}_r^2}{2\mu\hbar}} \\
& (2\pi)^{-1} \left(2\pi\sigma_r^2\right)^{-1/4} \left(\int_{-\infty}^{\infty} \mathrm{d}k \left(\int_{-\infty}^{\infty} \mathrm{d}x\, e^{-\frac{x^2}{2\sigma_r^2}} e^{-ikx} \right) e^{ik\delta r} \right) \\
=& (2\pi)^{-1} \left(2\pi\sigma_r^2\right)^{-1/4} \left(4\pi\sigma_r^2\right)^{1/2} e^{i\phi} e^{\frac{i\mu MG\tau}{r_0^2\hbar}\hat{\delta r}} \left(\int_{-\infty}^{\infty} \mathrm{d}k\, e^{-k^2\left(\sigma_r^2 + i\frac{\hbar\tau}{2\mu}\right)} e^{ik\left(\delta r - \frac{MG\tau^2}{2r_0^2}\right)} \right) \\
=& \left(2\pi^2\right)^{-1/2} \left(2\pi\sigma_r^2\right)^{1/4} e^{i\phi} e^{\frac{i\mu MG\tau}{r_0^2\hbar}\hat{\delta r}} \left((\pi)^{1/2} \left(\sigma_r^2 + i\frac{\hbar\tau}{2\mu}\right)^{-1/2} e^{\frac{-\left(\delta r - \frac{MG\tau^2}{2r_0^2}\right)^2}{4\left(\sigma_r^2 + i\frac{\hbar\tau}{2\mu}\right)}} \right) \\
=& \left(2\pi\sigma_r^2 \left(1 + i\frac{\hbar\tau}{2\mu\sigma_r^2}\right) 2\right)^{-1/4} e^{i\phi} e^{\frac{i\mu MG\tau}{r_0^2\hbar}\delta r} e^{\frac{-\left(\delta r - \frac{MG\tau^2}{2r_0^2}\right)^2}{4\left(\sigma_r^2 + i\frac{\hbar\tau}{2\mu}\right)}}.
\end{aligned} \tag{3.42}$$

At this stage there are two separate directions which can be used to characterise the entropy of gravitationally interacting Gaussian states. Specifically the above wave functions can be used, with the entanglement entropy being calculated under the restriction that $\frac{MG\tau^2}{2r_0^2} \ll r_0$. Or, the full time evolution can be calculated using $\hat{U}_r(t) = \hat{U}_r(n\tau) = \Pi_{j=0}^{n} \hat{U}_r(\tau, r_j)$ where $\hat{U}_r(\tau, r_j)$ refers to $\hat{U}_r(t)$ for some infinitesimal time step τ, with a centre of mass distance r_j which must be updated based on the previous time-step. Here the infinitesimal time evolution operators *must* be ordered with the earliest time-step (with r_0) being rightmost. For the moment however, I will take the first option. To calculate the entanglement entropy it is necessary to return to the original co-ordinate system.

3.3.4 Original Co-ordinate System

The joint state in the de-coupled co-ordinate system is given

$$\begin{aligned}
\Psi(\delta r,R,t) =& \psi_R(R,t)\,\psi_r(\delta r,t) \\
=& \left(2\pi\sigma_R^2\left(1+i\frac{\hbar t}{2M\sigma_R^2}\right)^2\right)^{-1/4} e^{\frac{-R^2}{4\left(\sigma_R^2+i\frac{\hbar t}{2M}\right)}} \\
& \times\left(2\pi\sigma_r^2\left(1+i\frac{\hbar\tau}{2\mu\sigma_r^2}\right)2\right)^{-1/4} e^{i\phi} e^{\frac{i\mu MG\tau}{r_0^2\hbar}\delta r} e^{\frac{-\left(\delta r-\frac{MG\tau^2}{2r_0^2}\right)^2}{4\left(\sigma_r^2+i\frac{\hbar\tau}{2\mu}\right)}} \\
\implies \Psi(r,R,t) =& \left(2\pi\sigma_R^2\left(1+i\frac{\hbar t}{2M\sigma_R^2}\right)^2\right)^{-1/4}\left(2\pi\sigma_r^2\left(1+i\frac{\hbar\tau}{2\mu\sigma_r^2}\right)2\right)^{-1/4} e^{i\phi} \\
& \times e^{\frac{-R^2}{4\left(\sigma_R^2+i\frac{\hbar t}{2M}\right)}} e^{\frac{i\mu MGt}{r_0^2\hbar}(r-r_0)} e^{\frac{-\left(r-r_0-\frac{MGt^2}{2r_0^2}\right)^2}{4\left(\sigma_r^2+i\frac{\hbar t}{2\mu}\right)}}. \qquad (3.43)
\end{aligned}$$

Using the identities: $\sigma_R^2=\frac{\sigma^2}{2}$, $\sigma_r^2=2\sigma^2$, $R=\frac{r_1+r_2}{2}$, $r=r_1-r_2$, $M=2m$ and $\mu=\frac{m}{2}$ to joint state is given by

$$\begin{aligned}
\Psi(r,R,t) =& \left(2\pi\sigma_R^2\left(1+i\frac{\hbar t}{2M\sigma_R^2}\right)^2\right)^{-1/4}\left(2\pi\sigma_r^2\left(1+i\frac{\hbar\tau}{2\mu\sigma_r^2}\right)2\right)^{-1/4} e^{i\phi} \\
& \times e^{\frac{-R^2}{4\left(\sigma_R^2+i\frac{\hbar t}{2M}\right)}} e^{\frac{i\mu MGt}{r_0^2\hbar}(r-r_0)} e^{\frac{-\left(r-r_0-\frac{MGt^2}{2r_0^2}\right)^2}{4\left(\sigma_r^2+i\frac{\hbar t}{2\mu}\right)}} \\
\implies \Psi(r_1,r_2,t) =& \left(\pi\sigma^2\left(1+i\frac{\hbar t}{2m\sigma^2}\right)^2\right)^{-1/4}\left(4\pi\sigma^2\left(1+i\frac{\hbar\tau}{2m\sigma^2}\right)2\right)^{-1/4} e^{i\phi} \\
& \times e^{\frac{-\frac{1}{4}(r_1+r_2)^2}{2\left(\sigma^2+i\frac{\hbar t}{2m}\right)}} e^{\frac{im^2Gt}{r_0^2\hbar}(r_1-r_2-r_0)} e^{\frac{-\left(r_1-r_2-r_0-\frac{mGt^2}{r_0^2}\right)^2}{4\left(2\sigma^2+i\frac{\hbar t}{m}\right)}} \\
=& \left(2\pi\sigma^2\left(1+i\frac{\hbar t}{2m\sigma^2}\right)^2\right)^{-1/4}\left(2\pi\sigma^2\left(1+i\frac{\hbar\tau}{2m\sigma^2}\right)2\right)^{-1/4} e^{i\phi} \\
& \times e^{\frac{im^2Gt}{r_0^2\hbar}(r_1-r_2-r_0)} e^{\frac{-(r_1+r_2)^2}{2\times4\left(\sigma^2+i\frac{\hbar t}{2m}\right)}} e^{\frac{-\left(r_1-r_2-r_0-\frac{mGt^2}{r_0^2}\right)^2}{2\times4\left(\sigma^2+i\frac{\hbar t}{2m}\right)}} \\
=& e^{\frac{im^2Gt}{r_0^2\hbar}(r_1-r_2-r_0)}\psi_1(r_1,t)\,\psi_2(r_2,t) \qquad (3.44)
\end{aligned}$$

where $\psi_1(r_1,t) = \left(2\pi\sigma^2\left(1+i\frac{\hbar t}{2m\sigma^2}\right)^2\right)^{-1/4} e^{\frac{-\left(r_1-\frac{r_0}{2}-\frac{mGt^2}{r_0^2}\right)^2}{4\left(\sigma^2+i\frac{\hbar t}{2m}\right)}}$ and $\psi_2(r_2,t) = \left(2\pi\sigma^2\left(1+i\frac{\hbar t}{2m\sigma^2}\right)^2\right)^{-1/4} e^{\frac{-\left(r_2+\frac{r_0}{2}+\frac{mGt^2}{r_0^2}\right)^2}{4\left(\sigma^2+i\frac{\hbar t}{2m}\right)}}$. Also, I have dropped the unimportant global phase, $e^{i\phi}$. The time dependent joint state of the two masses interacting via a quantum gravitational channel is

$$|\Psi(r_1,r_2,t)\rangle = \int \mathrm{d}r_1 \int \mathrm{d}r_2 \, e^{\frac{im^2Gt}{r_0^2\hbar}(r_1-r_2-r_0)} \psi_1(r_1,t)\,\psi_2(r_2,t)\,|r_1,r_2\rangle \tag{3.45}$$

where $|r_1,r_2\rangle = |r_1\rangle_1 \otimes |r_2\rangle_2$ is the position eigenbasis for the the two masses. Before proceeding however it is important to note a few things:

1. The joint time dependent wave function above can be identified to contain a few simple ingredients: a time and joint position dependent, gravitationally sourced phase term and two Gaussian states which are both spreading as if they are freely states, and whose centres of mass are moving towards one another like classically gravitating masses.

2. The above is only an approximation of the full joint state, because here only the centre of mass motion is really being considered. As a result, the mass wave functions are not spreading due to the gravitational curvature, acting like a tidal force. The centre of mass acceleration is also actually only an approximation of the full motion which only holds for short times.

3. Most importantly, the above states are *not entangled*. This shows that simply letting the masses attract under a completely linearised gravitational force is *not* enough to generate acceleration. A higher order, gravitational curvature term *must* be included for any hope of generating entanglement.

I can however go some way to correct for the approximations used to calculate the above state, recognising that we can simply invert the approximation used earlier

when originally applying the BCH expansion to get

$$\begin{aligned}\frac{1}{r_0^2}(r_1-r_2-r_0) =& \frac{1}{r_0}\left(1-\frac{r_1-r_2}{r_0}\right)\\ \approx& \frac{1}{r_1-r_2}\end{aligned} \tag{3.46}$$

where care is taken to ensure $r_1 > r_2$ (that is, consider the masses to be separated by large distance, with the first mass to be to the right of the first) which then gives

$$|\Psi(r_1,r_2,t)\rangle = \int \mathrm{d}r_1 \int \mathrm{d}r_2 \; e^{\frac{im^2Gt}{(r_1-r_2)\hbar}} \psi_1(r_1,t)\,\psi_2(r_2,t)\,|r_1,r_2\rangle\,. \tag{3.47}$$

It is worth stressing that this is not the full time evolved state, it is still an approximation of the full dynamics, one that is based largely on a linearised gravitational approximation.

The density state of the joint state can now be written out as

$$\rho = \int \mathrm{d}r_1 \int \mathrm{d}r_1' \int \mathrm{d}r_2 \int \mathrm{d}r_2' \; \Psi^*\left(r_1',r_2',t\right)\Psi(r_1,r_2,t)\,|r_1,r_2\rangle\left\langle r_1',r_2'\right| \tag{3.48}$$

and the reduced density matrix as

$$\begin{aligned}\rho_1 =& \int \mathrm{d}x_{\,2}\,\langle x_2|\,\rho\,|x_2\rangle_2\\ =& \int \mathrm{d}r_1 \int \mathrm{d}r_1' \int \mathrm{d}x\; \Psi^*\left(r_1',x,t\right)\Psi(r_1,x,t)\,|r_1\rangle\left\langle r_1'\right|.\end{aligned} \tag{3.49}$$

So now to characterise the entanglement the entropy of the reduced density operator can again be used. To do so here I will use the Renyi entropy of order 2 ($S_2(\rho_a)$), which is given by

$$S_2(\rho_a) = \frac{1}{1-2}\log\left[\mathrm{tr}\left(\rho_a^2\right)\right] \tag{3.50}$$

where ρ_a is the reduced density matrix for subsystem a. This was chosen as it avoids the added complexity of calculating the eigenvalues of the reduced density matrix, and so it was hoped it would enable the entanglement to be characterised

more easily. So it is necessary to first calculate the trace of the squared reduced density matrix:

$$\begin{aligned}
\mathrm{tr}\left(\rho_1^2\right) =& \mathrm{tr}\Bigg[\int \mathrm{d}r_1 \int \mathrm{d}r_1' \int \mathrm{d}r_1'' \int \mathrm{d}r_1'''\Bigg(\int \mathrm{d}x \ \left[\Psi^*\left(r_1',x,t\right)\Psi\left(r_1,x,t\right)\right] \\
&\times \int \mathrm{d}x' \ \left[\Psi^*\left(r_1''',x',t\right)\Psi\left(r_1'',x',t\right)\right] |r_1\rangle\langle r_1'| \, |r_1''\rangle\langle r_1'''| \Bigg)\Bigg] \\
=& \mathrm{tr}\Bigg[\int \mathrm{d}r_1 \int \mathrm{d}r_1' \int \mathrm{d}r_1'''\Bigg(\int \mathrm{d}x \ \left[\Psi^*\left(r_1',x,t\right)\Psi\left(r_1,x,t\right)\right] \\
&\times \int \mathrm{d}x' \ \left[\Psi^*\left(r_1''',x',t\right)\Psi\left(r_1',x',t\right)\right] |r_1\rangle\langle r_1'''| \Bigg)\Bigg] \\
=& \int \mathrm{d}r_1 \int \mathrm{d}r_1'\Bigg(\int \mathrm{d}x \ \left[\Psi^*\left(r_1',x,t\right)\Psi\left(r_1,x,t\right)\right] \\
&\times \int \mathrm{d}x' \ \left[\Psi^*\left(r_1,x',t\right)\Psi\left(r_1',x',t\right)\right]\Bigg). \qquad (3.51)
\end{aligned}$$

Now it is just a matter of actually evaluating the above integrals:

$$\begin{aligned}
&\int \mathrm{d}x \ \left[\Psi\left(r_1,x,t\right)\Psi^*\left(r_1',x,t\right)\right] \\
=& \int \mathrm{d}x \, e^{\frac{-im^2Gt}{\left(r_1'-x\right)\hbar}} e^{\frac{im^2Gt}{\left(r_1-x\right)\hbar}} \psi_1^*\left(r_1',t\right)\psi_2^*\left(x,t\right)\psi_1\left(r_1,t\right)\psi_2\left(x,t\right) \qquad (3.52)
\end{aligned}$$

At this stage the entropy should be computable numerically however given the limited computational power available and limited time this has been left incomplete.

Part II

Sensing Classical Gravity

Chapter 4

Curvature Detection with Massive Interferometers

In this chapter, I will demonstrate how atomic and particle interferometers might be used to detect and measure the curvature of space-time. This will proceed under the assumption that, over the extent of the experiment, the space-time consists of a flat (Minkowski) component and a much smaller perturbation on this. The local space-time can thus be written $g_{\mu\nu} = h_{\mu\nu} + \eta_{\mu\nu}$ where $\eta_{\mu\nu}$ is the Minkowski background and $h_{\mu\nu} \ll 1$.

The first section (4.1) in this chapter will consider how a general interferometric signal in a massive particle interferometer can encode information about the local space-time metric perturbations $h_{\mu\nu}$. I will present how the detectable components of the metric changes with the interferometer geometry. I will then choose a specific geometry to be used throughout the chapter and describe how it may be achieved. Sections 4.2, 4.3 and 4.4 will consider the detection of the Newtonian (h_{00}), Fame Dragging (h_{0j}) and Gravitational Wave (h_{ij}) signals respectively. Finally section 4.5 will contain some concluding remarks.

4.1 Detectable Components of Metric and Curvature

The detectable components of the space-time metric and its curvature can be determined by the path phase difference between the two arms of the interferometer, $\Delta\phi$.

This is in turn determined by the action difference between the two arms, ΔS, with

$$\Delta\phi = \frac{\Delta s}{\hbar} \tag{4.1}$$

The action for a particle with mass m travelling through along a trajectory ι through the linearised space-time metric will be

$$\begin{aligned} S^{\iota} &= -mc\int_{\iota} ds \\ &= -mc\int_{\iota}\sqrt{ds^2} \\ &= -mc\int_{\iota}\left(g_{\mu\nu}\frac{dx^{\mu}}{d\tau}\frac{dx^{\nu}}{d\tau}\right)^{1/2} d\tau \\ &= mc^2\int_{\iota}\left[(1-h_{00})\frac{dt^2}{d\tau^2} - h_{0j}\frac{v^j}{c}\frac{dt}{d\tau} - h_{i0}\frac{v^i}{c}\frac{dt}{d\tau}\right. \\ &\left. -\left(1+h_{ij}\right)\frac{v^i}{c}\frac{v^j}{c}\right]^{1/2} d\tau \end{aligned} \tag{4.2}$$

where I have used

$$ds^2 = -g_{\mu\nu}\frac{dx^{\mu}}{d\tau}\frac{dx^{\nu}}{d\tau}d\tau^2. \tag{4.3}$$

In the non-relativistic limit, when the proper time τ is approximately equivalent to the laboratory time t, this can be further simplified to

$$S^{\iota} \approx \int_{\iota} mc^2\left(1-\frac{1}{2}h_{00}\right) - mch_{0j}v^j - \frac{m}{2}\left(\delta_{ij}+h_{ij}\right)v^iv^j\,dt \tag{4.4}$$

where v^i is the particles velocity 3-vector.

To explore what components and derivatives of a general perturbation from the Minkowski background can be found using a massive particle interferometric scheme, the general action can be integrated over the classical trajectories through such a device. At this stage, I will define the reference frame as that for the apparatus. As such, a term like h_{xy} can be interpreted as an appropriate summation of terms such that it corresponds to the metric perturbation in the reference frame of the apparatus. That is, $\frac{\partial h_{0y}}{\partial x}$ is the directional derivative in the x direction of h_{0j} projected into the y direction.

The action can then be calculated approximately using a second order Taylor series expansion assuming a static and slowly varying metric, whereby

$$\begin{aligned} S^{\iota} \approx & \int_{\iota} mc^2 \left(1 - \frac{1}{2} h_{00}\right) - mc h_{0j} v^j - \frac{m}{2} \left(\delta_{ij} + h_{ij}\right) v^i v^j \, \mathrm{d}\tau \\ = & S^{\iota}_{00} + S^{\iota}_{0j} + S^{\iota}_{ij} \end{aligned} \tag{4.5}$$

given

$$\begin{aligned} S^{\iota}_{00} \approx & mc^2 - mc^2 \frac{1}{2} \int_{\iota} h_{00} + x(t) \partial_x h_{00} + y(t) \partial_y h_{00} \\ & + \frac{1}{2} \left(x^2(t) \partial_x^2 h_{00} + 2x(t) y(t) \partial_{xy} h_{00} + y^2(t) \partial_y^2 h_{00}\right) \mathrm{d}t \ , \end{aligned} \tag{4.6}$$

$$\begin{aligned} S^{\iota}_{0j} \approx & - mc \int_{\iota} v_x(t) h_{0x} + x(t) v_x(t) \partial_x h_{0x} + y(t) v_x(t) \partial_y h_{0x} \\ & + \frac{1}{2} \left(x^2(t) v_x(t) \partial_x^2 h_{0x} + 2x(t) y(t) v_x(t) \partial_{xy} h_{0x} + y^2(t) v_x(t) \partial_y^2 h_{0x}\right) \mathrm{d}t \\ & - mc \int_{\iota} v_y(t) h_{0y} + x(t) v_y(t) \partial_x h_{0y} + y(t) v_y(t) \partial_y h_{0y} \\ & + \frac{1}{2} \left(x^2(t) v_y(t) \partial_x^2 h_{0y} + 2x(t) y(t) v_y(t) \partial_{xy} h_{0y} + y^2(t) v_y(t) \partial_y^2 h_{0y}\right) \mathrm{d}t \ , \end{aligned} \tag{4.7}$$

and

$$
\begin{aligned}
S^{\iota}_{ij} \approx & -\frac{m}{2}\int_{\iota} v_x^2(t)+v_y^2(t)\mathrm{d}t \\
& -\frac{m}{2}\int_{\iota} v_x^2(t)\Bigg[h_{xx}+x(t)\partial_x h_{xx}+y(t)\partial_y h_{xx} \\
& +\frac{1}{2}\left(x^2(t)\partial_x^2 h_{xx}+2x(t)y(t)\partial_{xy}h_{xx}+y^2(t)\partial_y^2 h_{xx}\right)\Bigg]\mathrm{d}t \\
& -m\int_{\iota} v_x(t)v_y(t)\Bigg[h_{xy}+x(t)\partial_x h_{xy}+y(t)\partial_y h_{xy} \\
& +\frac{1}{2}\left(x^2(t)\partial_x^2 h_{xy}+2x(t)y(t)\partial_{xy}h_{xy}+y^2(t)\partial_y^2 h_{xy}\right)\Bigg]\mathrm{d}t \\
& -mc\int_{\iota} v_y^2(t)\Bigg[h_{yy}+x(t)\partial_x h_{yy}+y(t)\partial_y h_{yy} \\
& +\frac{1}{2}\left(x^2(t)\partial_x^2 h_{yy}+2x(t)y(t)\partial_{xy}h_{yy}+y^2(t)\partial_y^2 h_{yy}\right)\Bigg]\mathrm{d}t. \qquad (4.8)
\end{aligned}
$$

The phase difference observed at the end of the interferometery process will then be determined by the difference between the action of the two paths:

$$\Delta\phi = \sum_{\mu,\nu}\frac{\Delta S_{\mu\nu}}{\hbar} = \sum_{\mu,\nu}\frac{S^{\uparrow}_{\mu\nu}-S^{\downarrow}_{\mu\nu}}{\hbar} \qquad (4.9)$$

To gain a more general sense of what signals are possible it is best to consider multiple geometries. Specifically a 'box', 'triangular', 'diamond' and 'curved' as shown in Figure 4.1. The 'Box' geometry corresponds to an impossible, but conceptually simple design in which the spatial superpositions are created and destroyed instantaneously. The 'Triangle' and 'Diamond' geometries correspond to interferometers in which the particle moves with constant velocity in either a symmetric or asymmetric fashion. The reason for considering both symmetric and asymmetric interferometers will become clear later. Finally the 'curved' geometry corresponds to the geometry when the particle experiences a constant acceleration in the x direction.

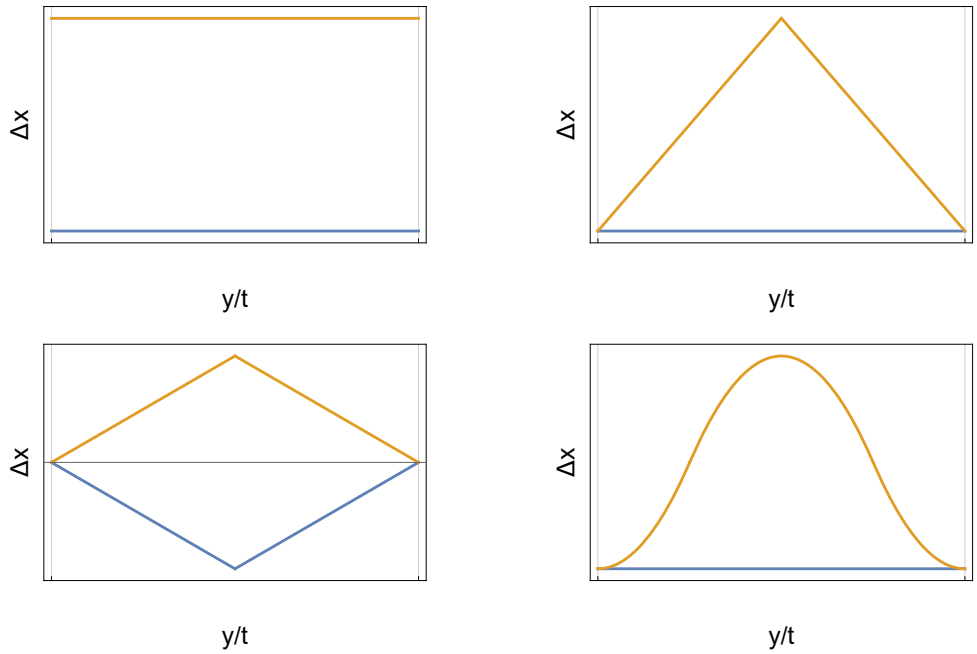

Figure 4.1: 'Box', 'Triangular', 'Diamond' and 'Curved' interferometer geometries. The orange and blue lines show the top and bottom arms respectively. Note that, as drawn here, a left handed co-ordintate system is used with the x axis corresponding to the vertical direction, and the y axis corresponding to the horizontal direction (or at times, equivalently time). This is done as in general we will actually consider a $1+1$ dimensional interferometer, with the only motion in the x spatial direction. In this case then the same figures can be used for the interferometers, with the vertical axis again corresponding to the x axis, but now the horizontal axis corresponds to time.

4.1.1 Action difference for varying geometries

The geometry depended action difference between the two interferometer arms can thus be found by evaluating equation 4.9 over each of the four trajectories shown in Figure 4.1. To do so I will assume 2+1 dimensional interferometers with a constant velocity in the y-direction v_y. These results can then be simplified into 1+1 dimensional interferometers by simply setting $v_y = 0$. The resulting output phases are:

Box Geometry:

$$\Delta S_{00} = -\frac{mc^2}{4}\left(2\partial_x h_{00}\Delta xT + \partial_x\partial_y h_{00}v_y\Delta xT^2 + \partial_x^2 h_{00}\Delta x^2 T\right) \tag{4.10}$$

$$\Delta S_{0j} = -\frac{mc}{2}v_y\left(2\partial_x h_{0j}\Delta xT + \partial_x\partial_y h_{0j}v_y\Delta xT^2 + \partial_x^2 h_{0j}\Delta x^2 T\right) \tag{4.11}$$

$$\Delta S_{ij} = -\frac{mc}{2}v_y^2\left(2\partial_x h_{ij}\Delta xT + \partial_x\partial_y h_{ij}v_y\Delta xT^2 + \partial_x^2 h_{ij}\Delta x^2 T\right) \tag{4.12}$$

Triangle Geometry:

$$\Delta S_{00} = -\frac{mc^2}{48}\left(3\partial_x h_{00}\Delta xT + 0.25\partial_x\partial_x h_{00}\Delta x^2 T + 1.5\partial_x\partial_y h_{00}v_y\Delta xT^2\right) \tag{4.13}$$

$$\begin{aligned}\Delta S_{0j} = -\frac{mc^2}{24}\Bigg(&3\partial_x h_{0j}v_y\Delta xT - 3\partial_y h_{0j}v_y\Delta xT + 0.25\partial_x\partial_x h_{0j}v_y\Delta x^2 T \\ &- 0.25\partial_x\partial_y h_{0j}v_y\Delta x^2 T + 1.5\partial_x\partial_y h_{0j}v_y^2\Delta xT^2 - 1.5\partial_y^2 h_{0j}v_y^2\Delta xT^2\Bigg)\end{aligned} \tag{4.14}$$

$$\begin{aligned}\Delta S_{ij} = -\frac{m}{48}\Bigg(&24Tv_x^2 + 6h_{ij}\Delta x^2 T^{-1} + \frac{6}{8}\partial_x h_{ij}\frac{\Delta x^3}{T} + \partial_x^2 h_{ij}\frac{\Delta x^4}{2^4 T} + 3\partial_y h_{ij}\Delta x^2 v_y \\ &+ 3\partial_x\partial_y h_{ij}v_y\frac{\Delta x^3}{2^3} + 3\partial_x h_{ij}v_y^2\Delta xT - 12\partial_y h_{ij}v_x v_y^2 T^2 + \partial_x^2 h_{ij}v_x^2 v_y^2 T^3 \\ &- 0.5\partial_x\partial_y h_{ij}v_y^2\Delta x^2 T + \partial_y^2 h_{ij}v_y^2\Delta x^2 T + 1.5\partial_x\partial_y h_{ij}v_y^3\Delta xT^2 - 3\partial_y^2 h_{ij}v_y^3\Delta xT^2\Bigg)\end{aligned} \tag{4.15}$$

Diamond Geometry:

$$\Delta S_{00} = -\frac{mc^2}{8}\left(2\partial_x h_{00}\Delta xT + \partial_x\partial_y h_{00}v_y\Delta xT^2\right) \tag{4.16}$$

$$\Delta S_{0j} = -\frac{mc^2}{4}\left(2\partial_x h_{0j}v_y\Delta xT - 2\partial_y h_{0j}v_y\Delta xT + \partial_x\partial_y h_{0j}v_y^2\Delta xT^2 - \partial_y^2 h_{0j}v_y^2\Delta xT^2\right) \tag{4.17}$$

$$\begin{aligned}\Delta S_{ij} = -\frac{m}{8}(&2\partial_x h_{ij}\frac{\Delta x^3}{T} + \partial_x\partial_y h_{ij}v_y\Delta x^3 + 2\partial_x h_{ij}v_y^2\Delta xT - 4\partial_y h_{ij}v_y^2\Delta xT \\ &+ \partial_x\partial_y h_{ij}v_y^3\Delta xT^2 - 2\partial_y^2 h_{ij}v_y^3\Delta xT^2)\end{aligned} \tag{4.18}$$

Curved Geometry:

$$\Delta S_{00} = -mc^2\left(\partial_x h_{00} 0.5\Delta x\tau_1 + 2\partial_x\partial_y h_{00} v_y 0.5\Delta x\tau_1^2 + \frac{23}{60}\partial_x^2 h_{00} 0.25\Delta x^2\tau_1\right), \tag{4.19}$$

$$\begin{aligned}\Delta S_{0j} = -mc\Bigg(&2\partial_x h_{0y} v_y 0.5\Delta x\tau_1 - 2\partial_y h_{0x} v_y 0.5\Delta x\tau_1 + 4\partial_x\partial_y h_{0y} v_y^2 0.5\Delta x\tau_1^2 \\ &- 4\partial_y^2 h_{0x} v_y^2 0.5\Delta x\tau_1^2 + \frac{23}{30}\partial_x^2 h_{0y} v_y 0.25\Delta x^2\tau_1 - \frac{23}{30}\partial_x\partial_y h_{0x} v_y 0.25\Delta x^2\tau_1\Bigg)\end{aligned} \tag{4.20}$$

$$\begin{aligned}\Delta S_{ij} = &-ma^2\left(\frac{2}{3}h_{xx}\tau_1^3 + \frac{1}{3}\frac{\partial h_{xx}}{\partial x}a\tau_1^5 + \frac{43}{420}\frac{\partial^2 h_{xx}}{\partial x^2}a^2\tau_1^7\right. \\ &\left. + \frac{4}{3}\frac{\partial h_{xy}}{\partial y}v_y\tau_1^4 + \frac{17}{10}\frac{\partial^2 h_{xx}}{\partial y^2}v_y^2\tau_1^5\right) \\ &- mv_y^2\left(\partial_y h_{xy} 0.5\Delta x\tau_1 + 2\partial_y^2 h_{yx} v_y 0.5\Delta x\tau_1 + \frac{293}{60}\partial_x\partial_y h_{xy} 0.25\Delta x^2\tau_1\right) \\ &- mv_y^2\left(\partial_x h_{yy} 0.5\Delta x\tau_1 + \frac{23}{60}\partial_x^2 h_{yy} 0.25\Delta x^2\tau_1 - \frac{38}{3}\partial_x\partial_y h_{yy} v_y 0.5\Delta x\tau_1^2\right).\end{aligned} \tag{4.21}$$

All geometries are sensitive to both first order and second order perturbations, however, only the asymmetric interferometers (Diamond and Curved) are sensitive to the zeroth order h_{ij} term. Thus it is these two geometries that or of most interest. Considering the curved trajectory, given the wide variety of terms, it is insightful to set $v_y = 0$ leaving

$$\Delta S\left(h_{ij}\right) = \frac{ma^2}{3}\left(-2h_{xx}\tau_1^3 + \frac{1}{2}\frac{\partial h_{xx}}{\partial x}a\tau_1^5 + \frac{43}{420}\frac{\partial^2 h_{xx}}{\partial x^2}a^2\tau_1^7\right). \tag{4.22}$$

So clearly such an interferometer can couple to gravitational waves h_{xx}.

Alternatively, if the free-fall of the particle due to earths acceleration is also considered:

$$\Delta S\left(h_{00}, g\right) = mc^2\left(\frac{\partial h_{00}}{\partial x}a\tau_1^3 + \frac{23}{60}\frac{\partial^2 h_{00}}{\partial x^2}a^2\tau_1^5 - \frac{9}{4}\frac{\partial^2 h_{00}}{\partial x^2}ag\tau_1^5\right) \tag{4.23}$$

and

$$\Delta S\left(h_{0j},g\right) = mcav_y\left(-2\frac{\partial h_{0x}}{\partial y}\tau_1^3 - 4\frac{\partial^2 h_{0x}}{\partial y^2}v_y\tau_1^4 + 2\frac{\partial h_{0y}}{\partial x}\tau_1^3 + \frac{23}{30}\frac{\partial^2 h_{0y}}{\partial x^2}a\tau_1^5 - \frac{9}{2}\frac{\partial^2 h_{0y}}{\partial x^2}g\tau_1^5\right). \tag{4.24}$$

However, as this only serve to increase the complexity of the equations, obfuscating the key details. As such these extra term will be neglected. It is also worth noting that these term could potentially also be eliminated by operating the apparatus in orbit, or alternatively levitating both arms through some other means to counteract the extra acceleration.

This shows that the interferometer is expected to be sensitive to the spatial derivatives of the metric and as such, by re-orientating the interferometer it would be possible to measure different components of the Riemann tensor. However, with this interferometric system no terms of the form $\partial_j h_{0j}$ or $\partial_i\partial_j h_{0j}$ can be detected. Given the interferometer is sensitive directly to h_{xx} and so therefore to all terms of the form h_{ij} this can be used to map out all derivatives of h_{ij}. It can also be noted that there will be a reduction in sensitivity by a factor of $1/c$ when non-time-like components of the curvature are detected.

The rest of this chapter will be used to discuss the use of this interferometer to detect earth's Newtonian gravitational potential, Frame dragging and finally gravitational waves. This will be done using a single curved geometry interferometer. This can be considered as modification of that proposed by Wan et. al. [113]. While they proposed the particle be initialised in a superposition of $s_z = \pm$, here it will considered to be in an initial spin superposition of $s_z = 0$ and $s_z = 1$. The interferometric scheme will then lead to both states having the same, constant velocity in only one direction, which I define as the y direction. To create the spatial superposition in the x direction, the spin 1 state will be moved away and then pulled back to the other spin state. This is proposed to be achieved by using the Stern-Gerlach effect to apply a constant, spin dependent acceleration a. The direction of this acceleration will need to change at times τ_1 and τ_2. This can be achieved by mapping the elec-

tronic spin state between $s_z = \pm 1$ or by reversing the direction of the magnetic field gradient. As the x direction is defined by the direction of the spacial superposition, it will also correspond to the direction of the applied magnetic field gradient. The interferometer geometry is then mostly controlled by the non-zero spin trajectory. This trajectory will be broken into three stages, signified by instantaneous changes in the acceleration. Beginning at time $t = 0$ the particle will have a acceleration a in the x direction until it reached a maximum velocity of v_x at $t = \tau_1$. The particles acceleration is then reversed to $-a$ time $t = \tau_2 = 3\tau_1$ at which point the velocity will be $-v_x$ and the magnetic field is once again flipped to give an acceleration a. The two paths recombine at time $t = \tau_3$ at which point the particle should have velocity only in the y direction. With this both arms will have travelled a distance of l in the y direction and phase difference between the two paths can be read out using Ramsay interferometry. The layout of this interferometer can be seen in figure 4.2.

Figure 4.2 also provides an insight into how an approximately constant, but controllable, magnetic field gradient might be acheived throughout a large spatial region. Specifically, the detail cut-away shows how this could be sourced by many flat current carrying wires arranged to approximate the ideal curved shape for the magnetic field source. By running a current through each pair of wires in the same direction only when the particle is directly below it we can ensure the particle experiences an approximately uniform magnetic field gradient in the desired direction, without requiring significant magnetic field magnitudes.

4.2 Newtonian Potential

Considering only the first perturbation term in Eq. 4.4, the standard substitution for the Newtonian potential, $h_{00} = 2MG/c^2R$ can be made. Defining the vertical as the x-axis, the experiment can be taken to be performed at ground level so R is radius of the Earth, and M Earth's mass, the difference in action between the two arms up

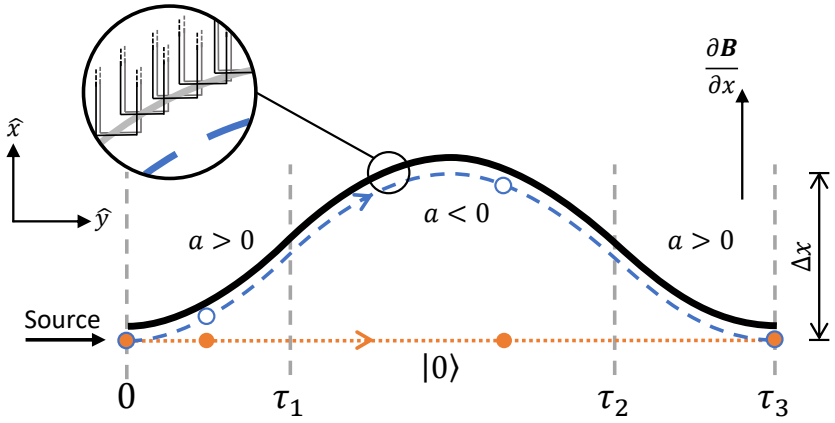

Figure 4.2: Interferometer path diagram showing spin $|\pm 1\rangle$ dashed blue path and spin $|0\rangle$ path dotted in orange. The magnetic field source (thick black line) could be shaped to follow the non-spin-zero path such that it can provide a large magnetic field gradient without a needing an exceedingly large magnetic field. The maximum superposition of $\Delta x = a\tau_1^2$ is achieved halfway through the interferometry process. The vertical dotted lines show the position when the acceleration direction changes occur. The circular cut-out shows the detail for how the magnetic field source could actually be implemented as many individual flat current carrying wires turned on in sequence. Note the unusual axis orientation with the x axis vertical representing the spatial superposition distance

to the second order in $\left(a\tau_1^2/R\right)$ is then

$$\Delta S\left(h_{00}\right) \approx -\frac{2mMG}{R^2} a\tau_1^3 + \frac{23mMG}{15R^3} a^2\tau_1^5 \tag{4.25}$$

$$\implies \Delta\phi\left(h_{00}\right) \approx \frac{-2\times 10^{35}}{1 \text{ kg m s}} \times ma\tau_1^3 + \frac{2\times 10^{28}}{1 \text{ kg m}^2 \text{ s}} ma^2\tau_1^5 \tag{4.26}$$

where I have used Equation 4.1 to conclude the output phase difference.

Eq.4.25 is consistent with the notion that any curvature detection will be of the form $U(L/R)^2$ where U is the gravitational potential and L is the characteristic laboratory length (in the above case, $L \sim a\tau_1^2$) [114]. Despite this quadratic suppression, it is still detectable due to the $1/\hbar$ factor in the phase difference. As such, even second order (curvature) effects can manifest as unit phase shifts or larger. Fig. 4.3 shows how these results scale with the mass of the object in the interferometer assuming a maximum allowed value of the spatial separation ($a\tau_1^2$). From Fig.4.3 it can be seen that a mass of 10^{-16} kg in a $\sim$ 1 mm interferometer with interrogation time $\tau_1 \sim$ 100ms gives a detection of acceleration with sensitiv-

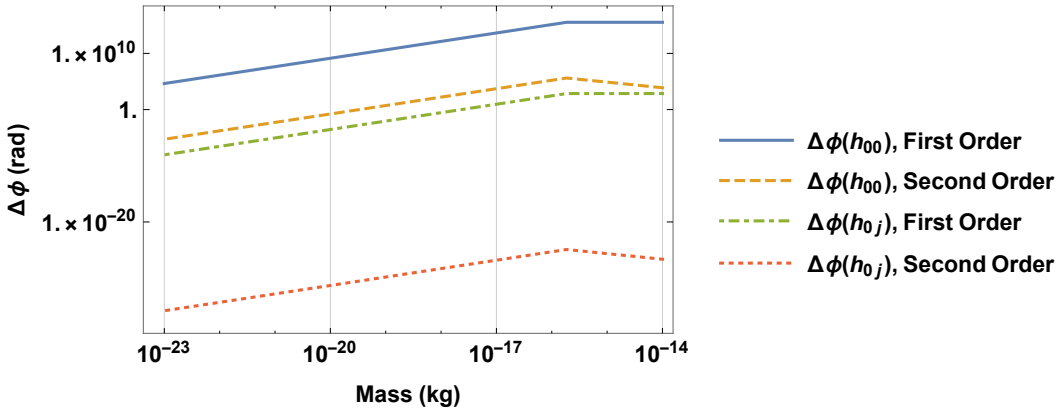

Figure 4.3: Newtonian potential and frame dragging phase difference scaling with the mass of objects for a maximum interferometer size and time of $\Delta x = 1$mm and $\tau_1 = 100$ms respectively with $v_y = 10\text{ms}^{-1}$. As the mass m increases, the phase change increases as $\Delta x = a\tau_1^2$ can be kept to its highest value by allowing more time τ_1. However, an optimal point is reached slightly after about $m = 10^{-16}$kg after which the Δx obtained with the maximum τ_1 starts decreasing in inverse proportion to mass even for the fixed maximum feasible values of magnetic fields (10^6Tm^{-1}).

ity down to $\sim 5 \times 10^{-15}\text{ms}^{-2}\text{Hz}^{-1/2}$. This result corresponds to sending a single particle through the interferometer at a time and as such represents a lower bound on the sensitivity of such a detector. This compares favourably with the recent work demonstrating the direct detection of metric curvature of a test mass which reported a sensitivity of 5×10^{-9} $\text{ms}^{-2}\text{Hz}^{-1/2}$ [33]

This detector could also be used to detect smaller masses and more local signals. For example, the mass M at distance R which yields a detectable phase shift compared to it not being there, effectively it ceasing to exist, is given by

$$M = \frac{\hbar R^2}{2\sqrt{N} m G \Delta x \tau_1} \tag{4.27}$$

which suggests for the interferometer specifications used for Fig. 4.3, at a distance of 1 km, a mass of approximately 4 kg is detectable provided the mass has moved from a very far distance to this 1 km range or by varying the interferometer orientation relative to the mass. On the other hand, all stationary masses naturally present around the interferometer will not act as a noise when detecting other signals as they will provide a constant phase difference between arms for a fixed orientation

of the interferometer.

I can also consider detecting the motion of a mass. Taking the motion to be slow enough that the interferometer phase can be found for the mass M at R before it moves a distance d and detected again. The minimum movement detectable will then be

$$d \approx \frac{\hbar R^3}{4\sqrt{N} m M G \Delta x \tau_1} \tag{4.28}$$

where it has been assumed that $d \ll R$. For example the previous $M = 4$ kg mass a distance $R = 100$ m away will produce a detectable phase variation if it moves by $d \approx 0.5$ m or more. This can act as a noise source when looking to detect other signals, this will be discussed below in Ch. 5.

4.3 Frame dragging

To explore the detection of frame dragging, the 'frame dragging' metric given in [115] was considered.

$$ds^2 = -H(r)\ c^2 dt^2 + J(r)\left[dr^2 + r^2\, d\theta^2 + r^2 \sin^2(\theta)\,(d\psi - \Omega\, dt)^2\right] \tag{4.29}$$

where

$$H(r) \approx 1 - \frac{8GM}{c^2 r} + \cdots,\ J(r) \approx 1 + \frac{8MG}{c^2 r} + \cdots, \tag{4.30}$$

here the binomial expansion approximation has been used for being in the linearized limit, and $\Omega = 2MG\nu/c^2R$ is the scaled angular velocity of the central rotating mass. Once again M is the mass of the Earth, R is its radius and ν is its angular velocity. The relevant component of Eq. 4.29 is the cross term $d\psi dt$.

The apparatus is taken to be aligned parallel with the with the equator and surface of the earth, and taking a small angle approximation with regards to the angular distance the mass travels along the interferometer in the 'y' direction measured from the centre of the earth. Defining M as the mass of the Earth, R its radius, and ν its angular velocity gives a phase difference, again to the second order in $\left(a\tau_1^2/R\right)$

$$\Delta\phi\left(h_{0j}\right) \approx \frac{8mMG\nu\sin^2(\theta)\,av_y}{\hbar c^2 R}\left(\tau_1^3 - \frac{3M^2G^2}{c^4R^2}\tau_1^3\right) + \frac{92mM^3G^3\nu\sin^2(\theta)\,v_y}{5\hbar c^6R^4}a^2\tau_1^5. \tag{4.31}$$

Substituting all known constants, assuming the interferometer is located on the surface of the Earth, gives $\Delta\phi\left(h_{0j}\right) \approx 4\times10^{21}mav_y\tau_1^3$ as the first order, metric dependent phase and $\Delta\phi\left(h_{0j}\right) \approx 6\times10^{-4}ma^2v_y\tau_1^5$ for the second order, curvature dependent phase. These effects are significantly more modest so high precision measurements would be needed, specifically to measure the second order term. Such measurements would provide an independent verification of the results from Gravity Probe B [37]. Fig. 4.3 also shows the phase due to first and second order effects independently with respect to the object mass.

4.4 Gravitational Waves

This setup is also senstive to gravitational waves, which manifest as transverse traceless perturbations around the Minkowski background:

$$h_{xx} = -h_{yy} \quad = h_+\cos(\psi_0+\omega t) \tag{4.32}$$

$$h_{xy} = h_{yx} \quad = h_\times\cos(\psi_0+\omega t)\,. \tag{4.33}$$

Here, I have assumed the GW is propagating along the $x_3 = z$ direction, perpendicular to the interferometer with angular frequency ω and taking the two helicity states of the GWs as $h_+,\ h_\times \ll 1$. Also ignoring the kinetic energy component of the particle's action as it is not relevant to the following discussion. The GW induced phase difference is

$$\Delta\phi\left(h_{ij}\right) = \frac{4mh_+a^2\tau_1\cos(\psi_0)\cos(\omega\tau_1)}{\hbar\omega^2}\left(1-\frac{\sin(\omega\tau_1)}{\omega\tau_1}\right) \tag{4.34}$$

$$\approx \frac{2mh_+a^2\tau_1^3\cos(\psi_0)}{3\hbar} \tag{4.35}$$

where ψ_0 is the wave's phase at $t = 2\tau_1$ and the approximate form holds when $\omega\tau_1 \ll 1$. Note the $h_\times$ component is not recorded in our interferometer, as it is pro-

portional to v_x, which varies between positive and negative values, thus cancelling itself out, unlike h_+ as it is a function of v_x^2. However, by rotating the apparatus, the x and y directions can effectively be relabelled, allowing for the detection of $h_\times$.

The underlying mechanism for this phase difference is ultimately through the particle coupling to the local space-time parameters (the metric). The metric is what will be directly affected by the GW, and this is detected through the phase evolution as given by the action, see Eq. 4.4. Note that our apparatus is *not* directly detecting the tidal acceleration of the particle caused by the GW. In fact, it is negligible compared to that generated by the magnetic field gradient needed to enable the interferometry. It simply measures the spatial stretching and contraction caused by the GW in the same manner as it would measure a permanent change in the relevant components of the metric. Of course, there is an unavoidable time variation of the metric due to the GW. However, this variation is not exploited here[1] – the time variation of the metric is much slower than an individual run of the interferometer for the frequencies this detector is most sensitive to. Essentially, the interferometer detects phase changes due to static metric components. In this way, the correct analogy here between laser interferometers and this particle interferometer is that the mass is the replacement for the photons. They both act to measure the change in spatial distances due to the GW. As the path length difference of $\sim h_+ L$ is essentially being measured in units of the matter-wave de Broglie wavelength, $\sim 10^{-17}$ m, $L \sim 1$ m suffices. To emphasize that one should *not* interpret this signal as the tidal acceleration as given by $h_+ L\omega^2$ directly acting on the mass.

This also leads directly to how the GW sensitivity in our interferometer scales uniquely compared to the acceleration sensitivity. Consider increasing the magnetic field gradient applied while reducing τ_1 such that $a\tau_1^2 = \Delta x$ remains fixed. The GW sensitivity scales as $\Delta\phi \propto \frac{\Delta x^2}{\tau_1}$ because the GW metric couples to the velocity of the particle ($S \propto h_{ij} v^i v^j$) while the stray acceleration sensitivity (h_{00}) scales as $\Delta\phi\,(h_{00}) \propto \Delta x \tau_1$. As such, the GW sensitivity can be further enhanced while

[1] Here, I am specifically referring to the variation during a single particles traversal of the interferometer. The sinusoidal modulation of the phase difference due to the variation of the metric from one run to the next will be how the GW is measured

suppressing the noise effects in our signal, giving an improved signal to noise ratio. Thus this detector is qualitatively very different from LIGO/LISA. This also highlights significant room for future advancement. Specifically, as the background gravity gradient noise acts as one of the primary limits to gravitational wave sensitivity in laser interferometers, the primary way they can be used to detect lower amplitudes and frequencies is by going into space. Here, this limit can be circumvented by improving the acceleration rate of the mass. This unusual behaviour can be understood as a result of precisely what is being detected by the interferometer. As discussed above, the gravitational wave is detected by the mass measuring the slight path length differences, so it is the length of space probed that is important, not how long the process lasts. In comparison, when measuring h_{00} terms which here act as noise, it is the difference in the acceleration between the two arms of the interferometer which is of interest, a difference that builds with time. By comparison, laser-based GW detectors cannot change the speed of the probing particles as the photons will always travel at a fixed speed.

A second *crucial* difference between laser interferometers and MIMAC is that there is no back-action and as such, the related standard quantum limit is not a limiting factor. This is because the measurement only occurs *once*, after the interferometry has taken place, and the position is not measured either, only the final spin state. Indeed our interferometer is closest in mechanism to single atom interferometers, which were suggested as some of the early atom-interferometry schemes for GW detection [42–44].

These two differences form the basis of the potential advantages this interferometer holds over laser interferometers, in which the standard quantum limit and Newtonian noise act as the primary limits on the sensitivity. Neither are fundamentally limiting with MIMAC or a MIMAC like interferometer.

Concerning the early atom interferometers, our advantage stems from the much larger mass, m. The SG methodology opens up the scope to create a high enough Δx, even with the increased mass. This raises the question that, shouldn't the smaller masses be capable of probing a large spacial region in less time? This

is true; however, given the sensitivity scales with mass, atomic or similar masses only become more sensitive once truly staggering ($\Delta x \sim O(1\text{ km})$) spatial superpositions are achieved. Here it should be noted that the more advanced proposals from atom interferometry such as Atomic GW Interferometric Sensor (AGIS) as discussed in [46] are qualitatively very different from this scheme. As such, only the scales should be compared, but not the mechanism. They generate a phase difference $\sim 10^{16} h_+$ for the space-based detector [45] with baseline size $L \sim 10^7$ m compared to our $\Delta\phi\left(h_{ij}\right) \sim 10^{17} h_+$ for a baseline size of 1 m as shown in Fig. 4.4. Again, as the mechanism of our proposal differs significantly from AGIS and related schemes, the above comparison does not capture the entire effectiveness of these two proposals.

One can see from Eq.4.35 that the phase output will be independent of GW frequency provided $\omega\tau_3 \sim \omega\tau_1 \ll 1$, though it will be limited by gravity gradient noise at lower frequencies (see Fig. 4.4). It is in this regime that our interferometer is most sensitive to GWs. The frequency scaling of detectability is understood by noting it is susceptible to the wave's time-averaged amplitude, which tends to zero for higher frequencies. As such, higher frequency GWs can be detected by using shorter time detectors, as seen in Fig. 4.4, albeit with a lower sensitivity without also increasing the magnetic field gradient and mass. Note that a detectable strain is defined by $\Delta\phi\left(h_{ij}\right) \geq 1/\sqrt{N}$ for N particles traversing the interferometer in series (and/or several interferometers in parallel). Further note that around $10 - 10^4$Hz, LIGO is already performing[116], while there are undetected lower frequency GW sources [117]. Thus such an interferometer would be complementary in part of the range of LISA [118] ($10^{-6} - 10$Hz) for an underground implementation or all of its range for a space based interferometer.

4.5 Discussion about Interferometer Size

So for all three phase results, when considering the mass dependence of the acceleration it appears that to obtain greater sensitivities with smaller masses or, the sensitivity is independent of mass. As such, one may conclude that using the small-

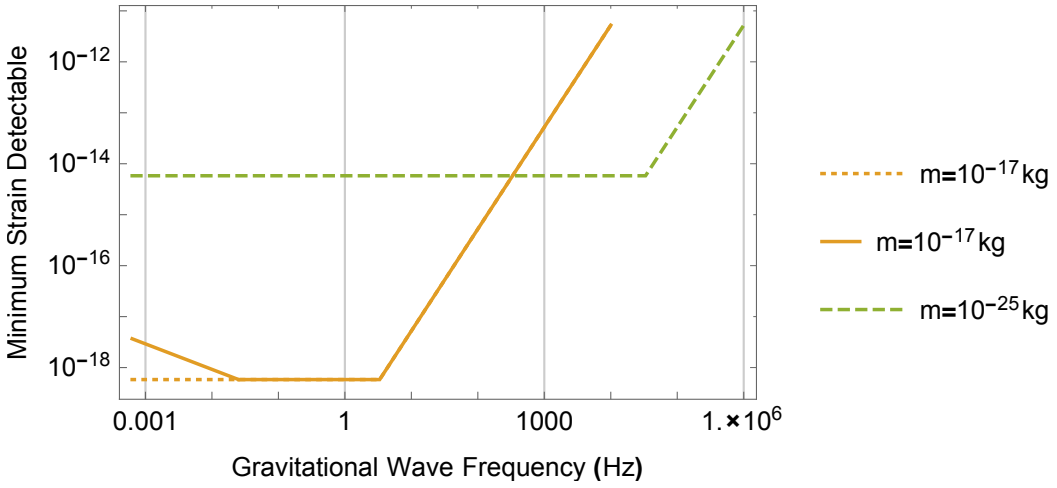

Figure 4.4: Comparison of strain sensitivity between two different mass, $\Delta x = 1$m GW detectors. The dashed green curve is for a ground based interferometer of mass 10^{-25}kg, $\tau_1 = 7.3 \times 10^{-5}$s and a flux $N = 10^6$ taken from [36] for Rb^{87} atoms, the lack of GGN limit in the sensitivity can be attributed to the extremely short interferometry time reducing the effect of the Newtonian potential in the final phase difference. The lower orange curves are for a 10^{-17}kg mass, $\tau_1 \approx 0.73$s, and $N = 400$ for ground based (solid, including GGN with relevant cancellation) and space based (dotted) sensitivities. It also shows the low frequency strain sensitivity reduction due to gravity gradient noise.

est masses available is optimal. However, this fails to consider the resulting size of the interferometer. If instead the size is constrained then we will retrieve the linear mass dependence such that larger test masses are desirable.

Consider the maximum separation between the two masses, $\Delta x = a\tau_1^2$. If instead this is considered as an important variable within the system then a multitude of combinations for m, τ_1 and a should be considered to optimise the sensitivity such that highly localised changes the gravitational field can be detected.

Consider for example Equation 4.26, making the substitution for Δx this becomes

$$\Delta\phi_{h_{00}} \approx 10^{35} m\Delta x\tau_1 + 10^{28} m\Delta x^2\tau_1. \tag{4.36}$$

and so the superposition size is fixed then once again it becomes beneficial to use the largest mass such that the target interferometer size is maintained. Similarly for Frame Dragging a phase shift of order

$$\Delta\phi\left(h_{0j}\right) \approx 10^{21} m v_y \Delta x \tau_1 + 10^{14} m v_y \Delta x^2 \tau_1. \tag{4.37}$$

Finally, gravitational wave signals are expected to generate a phase shift of

$$\Delta\phi\left(h_{ij}\right) \approx 10^{34} h_{xx} m \frac{\Delta x^2}{\tau_1} \tag{4.38}$$

In the next chapter I will present a noise analysis for such a detector, considering the likely limiting effects and mitigations for them.

Chapter 5

Noise and Uncertainty in MIMAC

While the interferometer discussed in the previous chapter is ambitious in its scope, the analysis was conducted by considering its 'in principle' feasibility, particularly with the example scheme for realising the interferometer. The proposed set-up will likely require state of the art magnetic field gradient stability, very low pressure and internal temperatures, all of which have been realized individually. It will also require the ability to send nanodiamonds into such a system and further manipulate them, which is still being developed. This all has to further be combined with cryogenic free flight [119]. Despite all this, at this level there does not appear to be any fundamental or insurmountable obstacle to its creation using current or near-future technologies.

In this chapter, I will seek to back up this claim by discussing the primary sources of decoherence as well as consider the primary sources of noises in the phase output signal. This will be used to place limits on the tolerable noise and fluctuations of the experimental parameters, such as mass fluctuations from one particle to the next and timings. On top of the constraints and methods discussed below, the creation of this interferometer will require further work to ensure excellent surface termination to reduce dangling bonds, motional decoupling and a method for the creation of a beam of flying diamond among further experimental advances on which work is ongoing [120].

As discussed in the previous chapter, to realise the proposed interferometer a magnetic field gradient ($\partial_x \vec{B}$) is used to create the spatial superposition of size

$\Delta x = a\tau_1^2$ with $a = g_{NV}\mu_B \partial_x \vec{B}/m$ where g_{NV} is the Landé g factor and μ_B is the Bohr magneton [23]. For large mass interferometry to carry an advantage over atoms, Δx must be kept $\sim$ 1m even while m increases. To this end, to keep $\tau_1 \approx 0.73$ s as is required to achieve our maximum GW sensitivity (see figure 4.4) a magnetic field gradient, $\partial_x \vec{B}$ of 10^6 Tm^{-1} is needed. Such a large magnetic field gradient could be created using a current-carrying wire, or many pairs of overhead wires as shown in Figure 4.2. This should allow for a more uniform magnetic field gradient to be maintained while increasing the distance between the interferometric particles and the wires, so reducing spurious forces. These wires would have to be arranged in many small horizontal sections such that they approximately follow the path of the non-zero spin interferometer arm. This allows the magnetic field generating wires to always remain close to the non-zero spin interferometer arm, generating a sufficiently large magnetic field gradient without also requiring an unreasonably large magnetic field. This will however require a large current, which will necessitate the use of carbon nanotube-metal composites. These can support a current density of up to $\rho_I = 10^{13}$ Am^{-2}[121]. The magnetic field gradient amplitude from a single wire is

$$B = \frac{\mu_0 I}{2\pi D} \tag{5.1}$$

$$\implies \partial_x B = \frac{\mu_0 I}{2\pi D^2} = \frac{\mu_0 \rho_I \tilde{r}^2}{2(\tilde{r}+\Lambda)^2}$$

$$\approx \frac{\mu_0 \rho_I}{8} \sim 10^6 \text{ Tm}^{-1} \tag{5.2}$$

where here D is the distance between the centre of the wire and the point at which the magnetic field strength is measured, $\tilde{r}$ is the radius of the wire, Λ is the distance from the surface of the wire and we have taken ($\Lambda \approx \tilde{r}$). In this way, the primary concern to creating the large magnetic field gradients necessary are the current stability and the distance Λ required to eliminate other interactions, such as the patch potential and Casimir interactions, importantly this distance simply sets the thickness required, and does not limit the theoretical possibility of achieving the required

magnetic field gradient. While such a device would likely require the many small pairs of overhead wires discussed, for clarity and as this is a simple proof of concept argument, a simpler (single bent wire) set-up will be discussed below. This should not significantly change the gradient strength, noise and decoherence between the two situations so that the analysis conclusion for many straight and one bent magnetic field source will be effectively the same.

5.0.1 Decoherence

One of the primary sources of decoherence for the spatial superposition states will be scattering of air molecules and black-body emission giving "which path" information. This decoherence has been considered elsewhere [122] which give a black body emission rate of

$$\Gamma_{bb} = \frac{16\pi^5 c\bar{R}^3}{189}\left(\frac{k_B T}{\hbar c}\right)^6 \mathrm{Im}\left(\frac{\varepsilon_{bb}-1}{\varepsilon_{bb}+1}\right) \tag{5.3}$$

and a collision rate of

$$\Gamma_{scatter} = \frac{16\pi\sqrt{2\pi}}{\sqrt{3}}\frac{P\bar{R}^2}{\bar{v}m_a} \tag{5.4}$$

where $\bar{R}$ is the particle radius, k_B is Boltzmann's constant, c is the speed of light, ε is the dielectric constant, P the pressure, $\bar{v}$ is the gas molecule average velocity and m_g is the mass of the gas molecules in the chamber.

Given the significant superposition size desired, particularly relative to the expected de Broglie wavelength of the mass, any black body or collision scattering event will completely decohere the superposition. As such, the above amounts to the black-body and collisional decoherence rates.

Taking the most ambitious interferometer parameters of the previous chapter which corresponds to a mass of $\sim 10^{-17}$ kg and 100 nm radius, the decoherence rates can be made sufficiently low ($\ll \frac{1}{t_4} \sim 1$ Hz). For example, they were calculated to be 0.006 Hz due to scattering of air molecules and 0.06 Hz due to black-body photon emission. This will require low pressures $\sim 10^{-14}$ Pa and low internal temperatures ~ 50 mK. These however have both been achieved separately in cryogenically cooled systems [123] for the pressure, and in a dilution fridge [119] or

using laser cooling [124, 125] to reduce the internal temperature. The electron spin coherence at 10 mK can also reach 1 s with dynamical decoupling [126, 127] which is already partially occurring in the design naturally due to spin flipping pulses. This can be further improved upon by applying pulses to the spin bath [128]. Furthermore, the scale of the superpositions considered here should not be incompatible with the predicted effects of stochastic GW induced decoherence given the mass employed is sufficiently small [129].

5.0.2 Gravitational Signals as Noise

By construction, the interferometric signal only depends on the relative phase between the two arms and thereby is immune to the thermal noise in the initial state $|\psi(0)\rangle$. Thus, for the most sensitive proposed detector (for GWs), the phases due to frame dragging and Newtonian potential (including gravity gradients [130]) will likely form the primary noise source. There can also be further noise sources due to the implementation, for example, particle-particle and particle-magnet Casimir, patch potential and gravitational interactions.

In the following, I will consider the most challenging to detect signals (GWs) for which the highest strain sensitivity of $h_+ \sim 10^{-18}$ occurs. I will consider employing a particle mass of $m \sim 10^{-17}$ kg and assume that $N = 400$ masses traverse the interferometer in series over the duration of the interferometer (τ_3), one after another. This can be achieved by successively cooling [124, 125, 131–133] and injecting one particle every ~ 10 ms. This then sets the signal strength, which all noises must be kept below. Further, for low-frequency GW detection, say for GWs of frequency ~ 10 mHz, one can do ~ 100 repeats of this interference during the period of the gravitational wave. This will improve the sensitivity by an order of magnitude to bring the detector into the range of detection of massive binaries at the above frequency [134]. One can further improve sensitivity by another factor of $1/\sqrt{\mathcal{N}}$ by using $\mathcal{N}$ interferometers in parallel. This is all assuming and interferometer characteristic time of $\tau_1 = 0.73$ s, and maximum particle velocity $v_x = a\tau_1 = 1.35$ ms^{-1}.

Firstly, a simple noise source in any signal, GW signals included, is due to pa-

rameter fluctuations from one run to the next. With this in mind, it is only necessary to consider the largest phase effect (the Newtonian potential) as it will magnify any uncertainty the most. It should be noted that, although not immediately obvious from 4.25, the first order Newtonian phase is independent of the particle mass. This is due to the inverse scaling of the superposition size with the mass. Furthermore, this noise can be suppressed by orientating the interferometer to be perpendicular to the Newtonian potential gradient (parallel with the ground). This will result in a phase uncertainty $\delta\phi$ due to mass (δm), distance (δR), superposition size ($\delta(\Delta x)$) and timing ($\delta\tau_1$) uncertainty of approximately

$$\delta\phi \approx \frac{23\delta m MG\sin(\alpha)}{15\hbar R^3}\Delta x^2\tau_1 + \frac{2mMG\sin(\alpha)}{\hbar R^2}\left(\frac{-2\delta R}{R}\Delta x\tau_1 + \delta(\Delta x)\tau_1 + \Delta x\delta\tau_1\right)$$

where $\alpha = 0$ when the interferometer is exactly perpendicular to the local Newtonian potential gradient. Note that the second-order noise is included to consider how mass uncertainty contributes to the noise. This was derived from Equation 4.25, allowing for variations in the experimental parameters and orientating the interferometer relative to the local Newtonian gravitational potential. Given that an orientation uncertainty ≤ 1 pRad is measurable [135], and hence $|\sin(\alpha)| \leq 10^{-12}$ is achievable, the mass, distance, separation and timing fluctuation would have to be kept below $\delta m \leq 10^{-18}$ kg, $\delta R \leq 0.1$ m $\delta(\Delta x) \leq 10$ nm and $\delta\tau_1 \leq 1$ ns respectively to ensure $\delta\phi$ is kept below the detectable limit. That is, to ensure $\delta\phi \leq 0.1$. Variations in otherwise known (systematic) phases can be countered through careful characterisation of system parameters and/or modifications of the interferometric setup.

It can be noted that some noises can be identified due to the unique functional dependences. Specifically, given the five identified signals scale uniquely with a, v_y and τ_1. Thus, individual signals could be identified separately by a network of interferometric sensors, allowing them to be filtered out of the signal. Of specific note is that by setting $v_y = 0$, 4.20 becomes zero. Doing so will limit the ability to introduce more than one particle into the interferometer at a time, making the sensitivity (and noise ceiling) $\Delta\phi = 1$ for a single run of a single interferometer. Further-

more, certain external noises can be actively cancelled. First-order signals can be detected and cancelled by a symmetric detector (using an initial spin superposition $\frac{1}{\sqrt{2}}[|+1\rangle+|-1\rangle]$) insensitive to second-order effects and importantly, the signal of interest (GWs). Here by first-order signals I am referring to terms in 4.19 and 4.20 which are a function of only a single derivative. This can be done as these are the only terms to which a symmetric interferometer is sensitive. This would allow these noises to be treated as signals which can be subtracted from the total phase output. The second-order Newtonian potential term can also be approximated by the use of slightly displaced symmetric interferometers. These would again be insensitive to GWs and result in third-order effects being left in the noise. This method of active cancellation would not be perfect. For example, consider a source located at a distance R from the primary detector, with secondary, symmetric interferometers located at $R\pm s$ from the source. The signal at the central asymmetric interferometer would be approximately the average of the signal at each symmetric interferometer on either side of it. This approximate signal can be used to cancel the phase noise, thus reducing it by a factor $\varepsilon^{(1)}$ which encompasses how close the approximation is. To determine $\varepsilon^{(1)}$ I expanded the signal in orders of $\frac{s}{R}$ from the central, asymmetric interferometer, giving

$$\begin{aligned}
\varepsilon^{(1)} &= \frac{\delta\phi^{(1)}(R)-\frac{1}{2}\left(\delta\phi^{(1)}(R+s)+\delta\phi^{(1)}(R-s)\right)}{\delta\phi^{(1)}(R)} \\
&= 1-\frac{1}{2}\left(\left(1+\frac{s}{R}\right)^{1/2}+\left(1-\frac{s}{R}\right)^{1/2}\right) \\
&\approx 1-\frac{1}{2}\left(1+\frac{s}{2R}-\frac{s^2}{8R^2}+1-\frac{s}{2R}-\frac{s^2}{8R^2}\right) \\
&= -\frac{s^2}{8R^2}. \qquad (5.5)
\end{aligned}$$

Take, for example, the movement of a 1 kg mass, a distance of 1 m away from the sensor and aligned with the interferometers x axis (the direction it is sensitive in). Taking the primary interferometer as having a symmetric interferometer above and below it at a distance of $s = 1$ cm then by 4.28 its movement would have to

be less than $d = 10^{-10}$ m without any active cancellation before it could source a signal clouding noise. However, with cancellation, this becomes $d = 10^{-5}$ m, a still significant but far less difficult value.

5.0.3 Gravity Gradient Noise

Distant Newtonian potential fluctuations are known as Gravity Gradient Noise (GGN) [136, 137]. This acts as one of the primary noise sources which limit GW detections in present-day GW antennas, particularly at the low frequencies. Gravity Gradient noise is often due to seismic waves causing variations in the local gravitational field or temperature fluctuations in the atmosphere. The seismic waves need not be as dramatic as earthquakes but stochastic fluctuations in the local density and surface fluctuations in the surrounding ground. It is difficult to say anything too specific about gravity gradient amplitudes as these are known to be highly location dependent [138]. However, I can estimate its effect by following the analysis performed in [139] and [140]. This can be combined with the gravity gradient accelerations measured at certain locations [141, 142]. I will then consider how well the expected noise can be cancelled.

Consider the effect of a fluctuation in the atmospheric or ground density $\Delta\rho$ of some volume V. For the example of ground-based fluctuations of wavelength λ and height ξ, $V = \lambda^2\xi$. Also, take this to occur at some distance r from the detector. This will yield an anomalous acceleration of magnitude

$$a = \frac{G\Delta\rho V}{r^2}\cos(\beta)\sin(\gamma) \tag{5.6}$$

where β and γ are the polar coordinates of the disturbance with the coordinate origin located at the detector. This was derived by considering the standard formula for the acceleration due to the Newtonian gravitational interaction and that the interferometer is sensitive in only a single direction. Thus the trigonometric dependencies are due to the directional sensitivity of the detector. To simplify the analysis, I will consider all regions of fluctuation as independent and so consider the combined effect by adding the squared acceleration. I will also consider a min-

imum distance, r_0, between the noise source and the detector. This can be achieved by implementing the detector within a highly controlled cavity with no density fluctuations. Considering initially an interferometer located at the surface of the earth, the square of the expected acceleration will be

$$a^2 \approx G^2\Delta\rho^2V^2\int_0^{\frac{\pi}{2}}\int_{-\pi}^{\pi}\int_{r_0}^{\infty}\frac{1}{r^4}\cos^2(\beta)\sin^2(\gamma)\,r^2\sin(\gamma)\,r\beta\gamma \tag{5.7}$$

$$\rightarrow a \approx \sqrt{\frac{2\pi}{3}}\frac{G\Delta\rho V}{\sqrt{r_0}} \tag{5.8}$$

If instead, the interferometer is placed underground at a depth d this becomes

$$a_u^2 \approx G^2\Delta\rho^2V^2\int_0^{\frac{\pi}{2}}\int_{-\pi}^{\pi}\int_{d/\cos(\gamma)}^{\infty}\frac{1}{r^2}\cos^2(\beta)\sin^3(\gamma)\,r\beta\gamma \tag{5.9}$$

$$\rightarrow a_{\mathrm{u}} \approx 0.6\frac{a\sqrt{r_0}}{\sqrt{d}}. \tag{5.10}$$

Using the measured median results in [141, 142] of $a_{\mathrm{surface}} = 3\times10^{-11}$ ms^{-2} for fluctuations occurring at 1 mHz, the underground phase noise due to a stochastically varying local acceleration, assuming $r_0 = 1$ m and $d = 100$ m, is estimated to be

$$\delta\phi^{(1)} \sim \frac{2m}{\hbar}\left(0.6\frac{a\sqrt{r_0}}{\sqrt{d}}\right)\Delta x\tau_1 \tag{5.11}$$

$$\sim 2\times10^5 \text{ rad} \tag{5.12}$$

which is clearly quite significant. It is also worth noting that 'quiet' (low GGN noise) sites can be expected to have noise values two orders of magnitude smaller [139]. There will also be second order effects ($\delta\phi^{(2)}$) where the local gravity varies across the interferometer which will be approximately a factor of $\frac{\Delta x}{\lambda} \sim 0.001$ smaller for typical fluctuation wavelengths $\lambda = 1$ km [138] giving $\delta\phi^{(2)} \sim 2\times10^2$ rad at 1 mHz.

Active cancellation of this noise may be possible by measuring and cancelling it using symmetric implementations of the interferometer, as discussed above. Em-

ploying this would reduce the phase noise to $\delta\phi^{(1)} \to \varepsilon^{(1)}10^5 \sim 10^{-4}$ for $s = 0.01$ m which is sufficient to potentially enable detections of GW in the mid-band frequency range.

There is, however, still the issue of the second-order phase variations ($\delta\phi^{(2)}$). External sensors can similarly approximate these. This would now require two symmetric interferometers (or other sensors) spread in the 'x' direction. The second-order phase variations will be given by the difference between them divided by the distance between them. The two interferometers would have to be spread further apart to make room for the original interferometer between them and will only accurately measure a linear change in g across the interferometer. This suggests the remaining error in the phase due to GGN after both sets of external sensors are used will be effectively the third-order GGN effect. This will be a further $\frac{\Delta x}{\lambda}$ smaller than the second-order effect, giving $\delta\phi^{(3)} \sim 10^{-1}$ rad at 1 mHz frequency. This is still significant, and as such, gravity gradient noise will create an effective noise floor to the sensitivity of our detector. To determine it effects on the sensitivity at other frequencies, the GW noise frequency dependence of $a \propto 1/\sqrt{f}$ [139] can be used to generate the noise floor after cancelling $\delta\phi^{(1)}$ and $\delta\phi^{(2)}$ as discussed. The remaining GGN is then

$$\delta\phi^{(3)} \sim \left(\frac{\Delta x}{\lambda}\right)^2 \frac{2m}{\hbar}\left(0.6\frac{\sqrt{r_0}}{\sqrt{d}} \times \frac{3\times 10^{-11}}{\sqrt{f/1\text{ mHz}}}\right)\Delta x\tau_1 \tag{5.13}$$

$$\approx \frac{8\times 10^{-3}}{\sqrt{f/1\text{ Hz}}} \tag{5.14}$$

for the $m = 10^{-17}$ kg interferometer used in figure 4.4. This suggests that the maximum sensitivity possible occurs in the 0.04 Hz-3 Hz range, in which the sensor achieves its greatest sensitivity, while the GGN is not prohibitive. This result also matches closely with the median GGN spectra as given in [141].

This is a somewhat crude model, treating both ground and atmospheric fluctuations at once, assuming uncorrelated fluctuations and integrating over each cell rather than summing over each external noise source. However, as I am using actual measured results for a_{surface} and in effect only concerned with the scaling with

r and d, it should be a suitable model for the moment. Also, as I am using the measured median GGN spectra, these results are likely to overestimate the noise as it would affect our interferometer as any such device would be placed at a 'quiet' site with low GGN. Furthermore, it is worth noting that such a method of measuring and cancelling noise can be applied to other GW sensors, potentially extending the ground-based observable frequencies in all GW sensors.

5.0.4 Heisenberg Uncertainty Noise

Another key noise source in standard GW detectors is the fundamental noise due to the Heisenberg uncertainty principle (HUP). I will consider how this fundamental uncertainty feeds into the final phase output to determine the fundamental noise floor in such a device. For simplicity, I will consider the mass to be in a coherent state cooled to or near the minimum uncertainty state, that is,

$$\sigma_x \sigma_p = \frac{\hbar}{2} \tag{5.15}$$

$$\sigma_p = \sqrt{\frac{m\omega\hbar}{2}} \approx 7\times 10^{-24}\ \text{kgms}^{-1} \tag{5.16}$$

$$\sigma_x = \sqrt{\frac{\hbar}{2m\omega}} \approx 7\times 10^{-12}\ \text{m}. \tag{5.17}$$

where the particle is assumed to be released from a 100 kHz trap. Beginning with position uncertainty, this could impact the final result due to the uncertainty in the initial position relative to the signal source, giving

$$\delta\left(\Delta\phi\left(h_{00}\right)\right) \approx \left(\frac{2mMG}{\hbar}a\tau_1^3\right)\left(\frac{1}{(R)^2}-\frac{1}{(R+\sigma_x)^2}\right)\sin(\alpha) \tag{5.18}$$

$$\approx \left(\frac{4mMG\sigma_x}{\hbar R^4}a\tau_1^3\right)\sin(\alpha) \sim 10^{-7}\sin(\alpha) \tag{5.19}$$

where α is the angle between the interferometer's x axis and the local plane of constant Newtonian potential. The second manner in which position uncertainty due to HUP typically can manifest as noise is by impacting the overlap of the particle's wave-packets.

Along similar lines we can consider how the initial momentum uncertainty

results in phase uncertainty. This gives

$$\delta\left(\Delta\phi_{h_{00}}\right) \approx \frac{8MG\sigma_p a\tau_1^4}{\hbar R^3}\sin(\alpha) \sim 10^5 \sin(\alpha) \tag{5.20}$$

as such provided $\alpha \ll 10^{-5}$, this noise should not pose as a limiting factor in such devices. Particularly as $\alpha \sim 10^{-12}$ [135] is possible and likely necessary (C.F. 5.0.2).

5.0.5 Particle-Particle Interactions

A further source of noise and decoherence is due to the particle's interactions with other particles traversing the interferometer. Any electrostatic interactions can be eliminated as the particle charge can be measured and modified down to the single electron level [143]. The other particle-particle interactions can be kept in check by ensuring the particle flux is low. Here I am defining the flux as the number of particles through the interferometer per second. The phase uncertainty it introduces is primarily due to the inter-particle Casimir interaction. It can be minimised by ensuring a large enough v_y such that the distance in the y direction between the particles is increased. For example, considering the effective Casimir potential (U_{C}) between two diamond ($\varepsilon = 5.7$) spheres of radius $\bar{R}$ a distance d apart as

$$U_{\mathrm{C}} = \frac{23\hbar c\bar{R}^6}{4\pi d}\left(\frac{\varepsilon-1}{\varepsilon+2}\right)^2 \tag{5.21}$$

provided $v_y = 10$ ms^{-1} then a flux $N = 1000$ will lead to a phase uncertainty of approximately 0.002 rad with a phase sensitivity to the 0.03 radian level per 'shot' (containing all $N = 1000$ particles). When $v_y = 1$ ms^{-1} the highest allowable flux is about $N = 90$ which gives a phase uncertainty of approximately 0.05 rad with sensitivity of approximately 0.1 rad per shot. To this end, $N = 400$ with $v_y = 10$ ms^{-1} is deemed an appropriate middle ground. It is sufficient to ensure the particle-particle interactions are negligible while also gaining phase sensitivity, with larger fluxes yielding phase sensitivity which would likely lost to other noises discussed above. Note that such large values for v_y may be achievable for a polarizable particle

(e.g. nanodiamond) using rapid acceleration in a pulsed optical field [144].

5.0.6 Magnetic Field Fluctuations

Fluctuations of the magnetic field and its gradient will affect the interferometer in multiple different ways. It can modify Δx, stop the interferometer closing perfectly, and through the phase fluctuation associated with variations in the magnetic potential energy.

The source of the magnetic field fluctuations will be due to variations in the current through the wire taking $I \to I + \delta I$. Such fluctuations will translate to variations in the applied acceleration δa and lead to a position uncertainty of δx. If such fluctuations occur at periods similar to the total interferometry time ($\tau_3 = 4\tau_1$), they will automatically be cancelled by the alternating direction of the acceleration. Similarly, if they occur significantly faster, they will on average cancel throughout the interferometry process. As such, the most significant position fluctuations occur if the sign of δI changes at times $t = \tau_1$ and then again at $t = \tau_2$, suggesting a characteristic period of $2\tau_1$, which leads its contribution to the acceleration not to cancel. In this instance

$$\frac{\delta(\Delta x)}{\Delta x} = \frac{\delta a}{a} = \frac{\delta I}{I}. \tag{5.22}$$

If multiple particles are traversing the interferometer in series, then for a later particle, this effect would be smaller or cancel completely. However, I will not consider this to ensure the noise is never underestimated in the analysis. In the context of the Newtonian potential variations from one run to the next we found that we require $\delta(\Delta x) \leq 10$ nm (CF. Section 5.0.2), which, given the maximum superposition size is $\Delta x = 1$ m, sets a limit to the current variation $\delta I = 10^{-8} I$ over a time-scale of $2\tau_1 \approx 1.5$ s. To ensure this is not exceeded, the experimentalists could actively monitor the current and employ feed-forward to keep drift below this level.

Furthermore, the current fluctuation due to thermal effects within the conducting wire by considering Johnson-Nyquist noise can be considered, which leads to a

current noise through a wire

$$\delta I = \sqrt{\frac{4k_B T \Delta f}{\underline{R}}} \tag{5.23}$$

where k_B is Boltzmann's constant, T the temperature of the wire, $\Delta f \sim 1$ Hz the bandwidth for noise, and $\underline{R} \sim 22$ kΩ is the wire's resistance[145]. This gives a current noise of $\delta I \sim 10^{-12}$ A if the wire is maintained at room temperature. This is likely to be well below the required noise floor, even with the wire heating up well above room temperature.

This will also cause the wave-packets to overlap only up to the bound given approximately by $\delta(\Delta x)$. However, this analysis has not considered that such a device will likely require many pairs of flat, current-carrying wires sourcing the magnetic field. Given such a set-up, the minimum fluctuation frequency is far greater, so its impact is lessened. To see this, note that each small section of the current-carrying wire pair will have to be controlled independently and thus will have an independent current fluctuating stochastically about the intended value I. Therefore, there is no independent noise at frequencies lower than that which corresponds to when each wire pair controls the particle. Noise at such frequencies essentially corresponds to the sum of noises from blocks of consecutive wires. Thus we do not need to consider them separately, considering the noise at the frequency corresponding to the time each wire pair controls the particle suffices. In this case, the wire pair controls the motion of the particle for typically $t_{\text{wire}} = 7$ μs to ensure the particle sees a uniform, linear magnetic field gradient throughout the interferometry process. This corresponds to a noise frequency of $f_{\text{wire}} \sim 1.4 \times 10^5$ Hz. Over the total time of the experiment $\sim$ 1s, the uncertain part of the Zeeman phase accumulated will be a summative random walk type phase. Here each wire interval is responsible for a step in the random walk. For this to be negligible, we require the random part of the magnetic field magnitude at the frequency f_{wire} to be $\delta B(f_{\text{wire}}) < \frac{\hbar}{\mu_B}\sqrt{f_{\text{wire}}} \sim 4$ nT. This corresponds to a current uncertainty of $\delta I(f_{\text{wire}}) < 20\mu A$ at the frequency of f_{wire}. For frequencies $f > f_{\text{wire}}$, the constraint on $\delta B(f) \leq 4\sqrt{f/f_{\text{wire}}}$ nT will only

be easier to satisfy. Additionally, the fluctuation in the gradient will also cause an uncertainty in the particle's position of

$$\begin{aligned} \delta(\Delta x) &= \frac{\delta I t_{\text{wire}}^2 \Delta x}{I \tau_1^2} \\ &\approx \frac{\delta I \times 10^{-10}}{I} \end{aligned} \tag{5.24}$$

which, by requiring $\delta(\Delta x) \ll \sigma_x$, bounds the high frequency (MHz) magnetic field fluctuations δI to $\delta I \ll 20$ A. This can be extrapolated to give a general, frequency dependent bound of

$$\delta I(f) \leq \frac{2 \times 10^3 \text{A Hz}^{-1/2}}{\sqrt{f}} \tag{5.25}$$

This will act to limit to using the results derived below we can conclude $\delta(\Delta x) \sim 10^{-15}$ m, far below the assumed wavepacket spread due to Heisenberg uncertainty of $\sigma_x \sim 10^{-11}$m and so is not of significant concern.

Finally, I considered the phase fluctuation due to uncertainty in the experimental parameters in the magnetic field coupling. This phase is due to the coupling between an electronic spin and an aligned magnetic field and is given by

$$\begin{aligned} \phi_{\vec{B}} &= \frac{\vec{\mu} \cdot \vec{B} t}{\hbar} \\ &= -\frac{egS}{2m_e\hbar} \frac{\mu_0 I}{2\pi D} t \end{aligned} \tag{5.26}$$

where e and m_e are the charge and mass of an electron, $g \approx 2$ is the gyromagnetic ratio, and S is the spin angular momentum. Now, as the spin state is reversed throughout the interferometer, the total phase will effectively unwind itself, up to the stability in the mean magnetic field strength and timing accuracy. In this way, the phase difference will be $\Delta\phi_{\vec{B}} = 0$ up to some stochastic fluctuations given by

$$\begin{aligned} \delta\left(\Delta\phi_{\vec{B}}\right) &= \frac{eg\hbar}{2m_e\hbar} \times \frac{\mu_0 \delta I}{2\pi D} \tau_3 + \frac{eg\hbar}{2m_e\hbar} \times \frac{\mu_0 \rho_I \pi D^2}{2\pi D} \delta t \\ &\sim \frac{10^{-7}\text{m}}{D} + 10^{17} \text{m}^{-1}\text{s}^{-1} D \delta t \end{aligned} \tag{5.27}$$

The first term implies a restriction on the distance between the centre of the wire and the particle of $D \geq 1$ μm, while the second term implies a limit on the timing uncertainty of $\delta t \ll 10^{17} D$ m^{-1}s. So, taking $D = 2 \times 10^{-5}$ m, thus requiring a current of $I \approx 2000$ A and magnetic field magnitude of $B = 40$ T, a timing uncertainty of $\delta t \leq 10^{-13}$ s is required. This is undoubtedly an onerous requirement but does not seem entirely unreasonable given the achievement of femtosecond timings also achieved recently [146].

5.0.7 Particle-Magnet Casimir Interaction

To model the particle-magnet Casimir induced phase fluctuations, I noted that as the particle radius is $\bar{R} \sim 10^{-7}$ m and the particle-magnet surface distance is kept at $\Lambda = 10^{-5}$ m, the particle-magnet system can be considered to be in the long-range limit (given $R \ll \Lambda$). The path phase difference with therefore be [147]

$$\Delta\phi_{\text{Casimir}} = \frac{23c\bar{R}^3}{4\pi\Lambda^4}\tau_3 \sim 10^6 \text{ rad} \tag{5.28}$$

where c is the speed of light, and τ_3 is the total interferometry time as shown in Figure 4.2. While this is significant, it is a constant phase provided the separation distance is also kept constant it can be normalised for in the output. This requires certainty in the particle-magnet separation to be $\sim 10^{-11}$ m while the timing stability mentioned above is sufficient here. This also leads to a maximum path displacement of $\sim 10^{-3}$ m over the length of the interferometer leading to the two states not overlapping without also adjusting the spin-0 arm of the interferometer. This displacement will be stable to the same level as the phase and should not limit the ability to overlap the two arms completely.

Patch potentials refer to electrostatic interactions between regions of non-zero charge on a globally charge-neutral object. The geometry of the system will further minimise the particle-magnet patch potential interaction. The patch potential force [148] scales as

$$F \propto \frac{\bar{R}e^{\Lambda/p}}{\sinh(\Lambda/p)} \tag{5.29}$$

where again $\bar{R} \sim 10^{-7}$ m is the particle radius, $\Lambda \sim 10^{-4}$ m is the particle-magnet

separation and here $p < \bar{R}$ is the linear size of the patch potential. This exponential suppression means that the patch potential is effectively negligible. Furthermore, since the particle moves past many differing wires which make up the magnetic field source, and by initialising the particles as physically spinning, any potential patch interactions would be averaged over. Finally, by constructing the particle a single from a single crystal, these patch potential effects could be made negligible by removing any patches of charge on the particle itself.

Part III

A Realistic Interferometer

Chapter 6

Engineering Schrödinger cat like superposition's with Stern-Gerlach effect

6.1 Introduction

In this chapter, I discuss the detail of how we expect to use diamond nano-spheres with an embedded nitrogen-vacancy (NV) centre as a promising candidate for a large mass capable of being placed in a large, discrete spatial superposition. I will consider multiple different designs, discussing and advantages or disadvantages and also discuss the feasibility of the configurations, particularly when employed as suggested throughout this thesis (Chapters 2 and 4) and proposed in [80].

6.2 Hamiltonian

To explicitly model the spin and the host crystal material, I will assume a nitrogen-vacancy (NV) centre spin in a diamond nano/micro-crystal is used. However, the results will hold for other potential materials provided they have similar values of diamagnetic susceptibility. The internal spin state due to the NV centre will be taken as initialised in the state $\frac{1}{\sqrt{2}}(|1\rangle + |-1\rangle)$. It will also be assumed that the mass will be in *free fall* along the z-axis due to gravity; this can be achieved in a drop-tower experiment and will indeed likely be necessary to avoid external gravitational noise

sources [149]. I will consider a magnetic field $\vec{B}$ and look to create a splitting in the x direction. This situation is thus described by the Hamiltonian [150, 151]

$$H = \frac{\hat{P}_x^2 + \hat{P}_y^2 + \hat{P}_z^2}{2m} + mg\hat{z} + \hbar D\hat{S}_z^2 - \frac{\chi_m m}{2\mu_0}\hat{B}^2 - g\mu_B \hat{s}\cdot\vec{B}, \tag{6.1}$$

where m is the mass of the diamond, χ_m is the mass magnetic susceptibility, $g \approx 2$ is the land'e g factor, $\mu_B = \frac{e\hbar}{2m_e}$ is the Bohr magneton, $\hat{s}$ is the spin operator, and $D = (2\pi) \times 2.8$ GHz is the NV zero-field splitting. This Hamiltonian does not couple the x, y and z axes, and as such, the motion in each can be considered independently. Thus to simplify things, unless otherwise specified, I will consider the interferometer as one dimensional, with the splitting defining the x-axis. Any motion due to gravity will be along the z axis and is not analysed. The above Hamiltonian does not consider the full spin dynamics either, this however will be justified below.

6.3 A New method

It has been generally assumed previously [4, 69, 80, 149, 152–154] that employing the Stern-Gerlach effect to create a spatial splitting will result in constant or approximately constant acceleration. This spin-dependent acceleration, a, would have a magnitude given by

$$a\left(s_x, \partial\vec{B}\right) = \frac{g e\hbar}{2m_e} s_x \partial_x B \tag{6.2}$$

where $g \approx 2$ is the Landé g factor, e and m_e are the charge and mass of an electron respectively, and the $s_x = \pm 1$ states of the NV centre will be used. Creating a large spatial splitting of Δx would then require the mass to be accelerated for a time $t_a = \sqrt{\frac{\Delta x}{a\left(-1,\partial\vec{B}\right)}}$ when using a magnetic field with a constant gradient. However, this fails to consider that when pushing towards the mesoscopic mass regime, diamagnetism can significantly affect the motion. This has now been highlighted [151], which suggested that instead of constantly accelerating in a linear magnetic field (constant magnetic field gradient), the mass will act as an harmonic oscillator. However, this analysis did not touch on the spin dynamics, particularly the possibility

of Majorana spin flips occurring or the spin stability provided by high-frequency Larmor precession.

Here, I will consider the constraints on the magnetic field and seek to address these problems directly. Noting that $\vec{\nabla}\cdot\vec{B}=0$ and $\vec{\nabla}\times\vec{B}=0$, as the masses are away from the source of the magnetic field. For simplicity, I assume will assume the magnetic field to have the following profile: $\vec{B}=B_x(x,y)\hat{x}+B_y(x,y)\hat{y}$ and set $\hat{z}\cdot\vec{B}=0$. Again, I will also define the x axis as the desired superposition direction and require the magnetic field to have a constant magnetic field gradient along the x direction of magnitude η. This is strictly speaking an unnecessary requirement. However, it is expected to lead to simpler dynamics to understand and is taken as a general requirement, at least initially.

Majorana spin-flip transitions can occur in regions where the magnetic field approaches zero magnitude. This is due to the selected spin states, in this case $s_x=\pm1$ can become degenerate with other spin states. This could lead to a loss of both control due to the spin-dependent motion utilised in SG interferometry; and coherence given its internal spin state which is interfered. This then sets a straightforward requirement on the experimental set-up: $|B_x(x,y)|\gg\left|B_y(x,y)\right|\forall x,y$ in the vicinity of the controlled trajectories.

A second consideration is the Larmor precession frequency. Larmor precession occurs as a magnetic moment, in this case the internal intrinsic spin, will experience a torque in the presence of an external magnetic field. This serves a very beneficial role in SG interferometry as it serves to effectively uncouple the spinor components [155–157]. It is this that then allows the SG interferometer to act as a 1-D interferometer. To see this, consider an electron with spin $s_z=\frac{1}{2}$ in a bias magnetic field $\vec{B}=B_0\hat{z}$. This will not cause and precession in the spin $s_z=\frac{1}{2}$ state. However the spin $s_x=\pm\frac{1}{2}$ and $s_y=\pm\frac{1}{2}$ states will precess with frequency $\omega_L=-\frac{ge}{2m_e}|B|$ where $g\approx2$ is here the Landè g factor, e is the electron charge and m_e is the electron mass. Suppose this precession frequency is much faster than the translational dynamics induced by the SG effect. It would then effectively average out any motion in the directions transverse the applied bias field. Thus, ensuring there is always

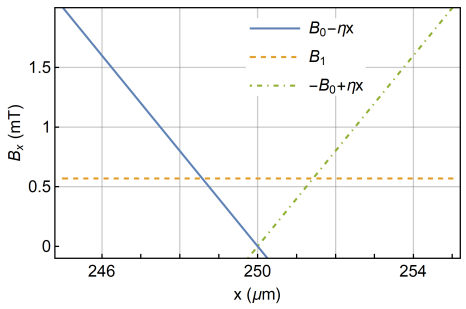

(a) Diagram of the x components of the magnetic fields considered. The inset figure shows detail around the zero-field region.

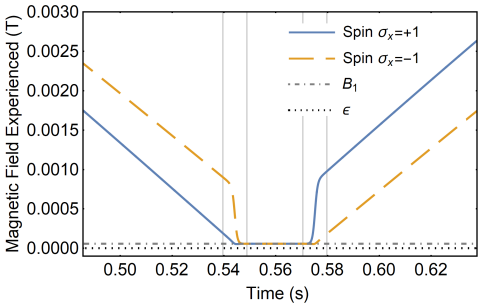

(b) Magnetic field experienced by each arm of the interferometer with time. The vertical grey lines represent times τ_i for $i = 1,2,3,4$.

Figure 6.1: Figures showing the three different magnetic fields being employed as well as how this is experienced by the particle. Fig.6.1a shows the magnetic field profile along with an insert showing the details around the zero-field region. Fig.6.1b shows an example of how the magnetic field is experienced by the two arms of the interferometer around the zero-field region. Both figures are for $B_0 = 10^{-2}$ T, $\eta = 40$ Tm^{-1} and $B_1 = 100\varepsilon$ T.

a significant bias field in the direction of the desired splitting, an experimentalist can ensure that only the desired splitting direction is chosen.

6.3.1 Finding a Suitable Magnetic Field

The simplest form for the magnetic field which will satisfy all the above conditions will be of the general form

$$\vec{B}(x,y) = (B_0 + \eta x)\,\hat{x} - \eta y \hat{y}\,, \tag{6.3}$$

where the magnetic field gradient must be in two directions due to the limitations on the field's divergence. This also highlights why the bias field induced, rapid Larmor precession is necessary. It is impossible to create a magnetic field gradient in only one direction.

Provided $|B_x(x,y)| \gg |B_y(x,y)|$, and by ensuring $y \approx 0$ and

$$x \notin \left[\frac{B_0 - \varepsilon}{\eta}, \frac{B_0 + \varepsilon}{\eta}\right], \tag{6.4}$$

which we define as the *zero field region*, the motion in the y direction can be made to rapidly average out. The above condition accounts for both the Larmor *and* the

Majorana spin-flip transitions. As such, provided ε is sufficiently large, the spin state in the y and z basis will experience a rapid Larmor precession. As such only the on-axis magnetic field gradient needs to be considered for the rest of our analysis [155, 156].

If we desire a minimum Larmor frequency of ω_L^{min}, we can define a minimum allowable magnetic field magnitude:

$$\varepsilon \sim -\frac{2m_e\omega_L^{min}}{ge}. \tag{6.5}$$

Therefore, the particle must not enter this region given by Eq.(6.4). Given that we know the mass will act like an harmonic oscillator in such a magnetic field, with the centre of the well near the zero point of the field, this requirement is almost always violated unless care is taken. As such, there are two options for how this can be achieved with the mass initialised to one side of the harmonic traps: The superposition can be closed before the trajectories reach the zero-field region or; the magnetic field can be mapped to a different magnetic field as the trajectories enter the zero-field region. Due to the substantial limitation placed on the superposition size by the first option, I will choose the latter.

To achieve this, it is necessary to use three linear magnetic fields:

$$\vec{B}(x,y) = (B_0 - \eta x)\hat{x} + \eta y\hat{y} \tag{6.6}$$

$$\vec{B}(x,y) = B_1\hat{x} \tag{6.7}$$

$$\vec{B}(x,y) = -(B_0 - \eta x)\hat{x} - \eta y\hat{y} \tag{6.8}$$

as seen in figure 6.1a. Note that had the magnetic field been mapped back to Equation 6.6, then the mass would have to experience a zero magnitude magnetic field as the value of the field is continuous. The constant magnetic field will still have the same requirements as the bias field, that is, $B_1 \gg \varepsilon$, and the timing of the switching between the magnetic fields will be done to ensure that the particle never experiences nearly *zero* magnetic field. To smoothly map between the the different

magnetic fields, a switching function was defined as:

$$\begin{aligned}\mathrm{Sw}(t,t_{on},t_{off}) =& 0.5\left(\tanh\left[\Omega\left(t-t_{on}\right)\right]+1\right)\\ &\times 0.5\left(\tanh\left[\Omega\left(t_{off}-t\right)\right]+1\right)\end{aligned} \tag{6.9}$$

where Ω is the switching frequency parameter. This parameter will have to be sufficiently slow such that the magnetic field change is always adiabatic. This is to ensure that it does not complicate the spin dynamics.

6.3.2 Switching Frequency and Adiabaticity

To ensure that no Majorana spin flips are induced and avoid complicated spin dynamics in general, it is necessary to ensure the magnetic field switching frequency Ω is sufficiently low. The adiabaticity condition can be written in at least two forms:

$$\dot{\omega}_L \ll \omega_L^2 \tag{6.10}$$

and

$$\Omega \ll \omega_L^{min}. \tag{6.11}$$

The first ensures that the change in the spin dynamics is slower than the spin dynamics itself, while the second ensures the magnetic field changes slower than the spin dynamics. Now, these will depend on the trajectories taken through the magnetic field, which is itself, in part, determined by the value of Ω. As such, an assumed value was taken, and the above conditions we verified. The result was that $\Omega = 10^3 - 10^6$ Hz was necessary, with shorter time interferometers employing higher-frequency switching. The above adiabaticity conditions were checked by plotting their values throughout the relevant section of the trajectory. The second condition can also be made to hold by directly setting $\Omega \ll \omega_L^{min}$.

6.3.3 Solving Dynamics

Given this set of magnetic fields, the achievable superposition size can be calculated. To do so, first, the equations of motion should be determined. As previously

discussed, only a one-dimensional form of the Hamiltonian is needed, which significantly simplifies the motion. Now it is worth considering the general scheme so that the analytically solvable steps can be identified and solved. I will define five distinct phases of evolution. Each is determined by the current state of the magnetic field ($\vec{B}$) as this controls the trajectories. The five phases are

1. $t < \tau_1$, $\vec{B}$ is given by Eq.6.6.
2. $\tau_1 \leq t < \tau_2$, $\vec{B}$ is switching adiabatically from Eq.6.6 to Eq.6.7.
3. $\tau_2 \leq t < \tau_3$, $\vec{B}$ is given by Eq.6.7.
4. $\tau_3 \leq t < \tau_4$, $\vec{B}$ is switching adiabatically from Eq.6.7 to Eq.6.8.
5. $\tau_4 \leq t$, $\vec{B}$ is given by Eq.6.8.
6. $t = \tau_5$, when the spin states are reversed to close the superposition while $\vec{B}$ is still given by Eq.6.8.
7. $t = \tau_6$, when the two wave functions are brought to overlap in the position and the momentum basis.

As shown below, the motion when $0 \leq t < \tau_1$ and $\tau_4 \leq t$ is solvable analytically (see subsection 6.3.3.1). The motion when $\tau_1 \leq t < \tau_4$ is, however, far more complicated. As the switching function leads to a time dependance in the potential, the motion is not easily solvable analytically. Instead, it was solved numerically, as discussed in subsection 6.3.3.2.

6.3.3.1 Analytical Solution

Here I will consider the general analytic solution for the trajectories when $0 \leq t < \tau_1$ and $\tau_4 \leq t$. Given the large mass of the particle, we can solve for the classical equations of motion to determine the trajectories. As previously mentioned, the result is expected to be that for an harmonic oscillator. To see this, consider the Hamiltonian during the first stage of the motion:

$$H_x = \frac{1}{2m}p_x^2 - \frac{\chi_m m}{2\mu_0}(B_0 + \eta x)^2 - \frac{g\not{e}\hbar}{2m_e}S_x(B_0 + \eta x). \tag{6.12}$$

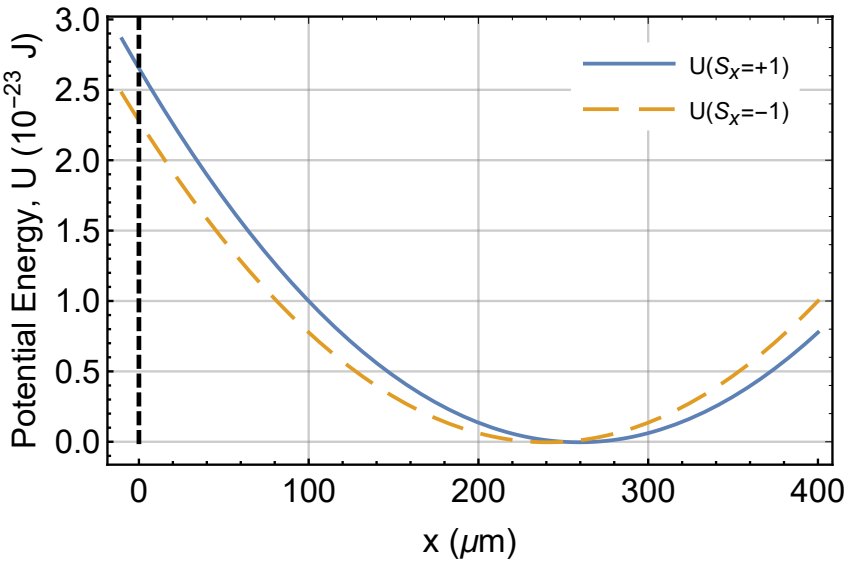

Figure 6.2: Potential energy corresponding to both spin $S_x = +1$ and $S_x = -1$ for a magnetic field as given by Eq. 6.6. The initial position is shown by the vertical black dashed line.

As such the potential energy of the mass will be

$$U(x) = -\frac{\chi_m m}{2\mu_0}(B_0 + \eta x)^2 - \frac{g e\hbar}{2m_e} S_x (B_0 + \eta x) \tag{6.13}$$

which is be seen in Figure 6.2.

This can be simplified using a change of variables, using $x = x' + \frac{\kappa}{\eta} - \frac{B_0}{\eta}$, the potential energy

$$U(x) = -\frac{\chi_m m}{2\mu_0}(B_0 + \eta x)^2 - \frac{g e\hbar}{2m_e} S_x (B_0 + \eta x) \tag{6.14}$$

becomes

$$\begin{aligned} U(x') &= -\frac{\chi_m m}{2\mu_0}\left(B_0 + \eta\left(x' + \frac{\kappa}{\eta} - \frac{B_0}{\eta}\right)\right)^2 - \frac{g e\hbar}{2m_e} S_x \left(B_0 + \eta\left(x' + \frac{\kappa}{\eta} - \frac{B_0}{\eta}\right)\right) \\ &= -\frac{\chi_m m}{2\mu_0}(\eta x' + \kappa)^2 - \frac{g e\hbar}{2m_e} S_x (\eta x' + \kappa) \\ &= -\frac{\chi_m m}{2\mu_0}\eta^2 x'^2 - \frac{\chi_m m}{\mu_0}\left(\kappa + \frac{\mu_0 g e\hbar}{2\chi_m m m_e} S_x\right)\eta x' - \frac{g e\hbar}{2m_e} S_x \kappa - \frac{\chi_m m}{2\mu_0}\kappa^2. \end{aligned} \tag{6.15}$$

As such, by setting $\kappa = -\frac{\mu_0 g e\hbar}{2\chi_m m m_e} S_x$, the linear term in x' in the potential energy disappears, leaving the potential for a simple harmonic oscillator with an unimportant constant in the end. This means that the mass will indeed act like a particle in an harmonic trap which is centred at $x = \frac{\kappa}{\eta} + \frac{B_0}{\eta} = \frac{\mu_0 g e\hbar}{2\chi_m m m_e \eta} S_x + \frac{B_0}{\eta}$. This allows the general solution to the equations of motion for the trajectories in to be known straight away, giving

$$x(t) = A\cos(\omega t + \phi) + C(s_x) \tag{6.16}$$

for $0 \leq t < \tau_1$ and $\tau_4 \leq t$ where A and ϕ are determined by the initial conditions, $\omega = \sqrt{-\frac{\chi_m}{\mu_0}}\eta$ is the frequency of the diamagnetic trap and $C(s_x)$ is determined by the spin state. Note that the spin will always be within the adiabatic limit throughout these times, such that $\dot{\omega}/\omega^2 < 1$ as η is constant for this duration of the experiment. The translation constant is then

$$C^{s_x=\pm 1} = B_0/\eta \pm \alpha\,, \tag{6.17}$$

where $\alpha = -\mu_\pm \frac{\mu_0}{\chi_m m \tilde{\eta}(t)} = -\frac{g e\hbar}{2m_e}\frac{\mu_0}{\chi_m m \tilde{\eta}(t)}$, where $\tilde{\eta}(t) = \eta$ when $t < \tau_1$ and $\tilde{\eta}(t) = -\eta$ when $t > \tau_4$ accounts for the changing sign of the magnetic field gradient.

The trajectory through these times, $t \notin [\tau_1, \tau_4]$, can be constructed by simply assembling the solutions piecewise. To do this, the values of the constants are determined by the initial conditions for each time segment. Specifically, if $x(t_0) = x_0$ and $\dot{x}(t_0) = v_0$ serve as the initial conditions, then

$$A = -(C - x_0)\left(1 + \frac{v_0^2}{\omega^2}(C - x_0)^{-2}\right)^{1/2} \tag{6.18}$$

$$\phi = \tan^{-1}\left(\frac{v_0}{\omega(C - x_0)}\right) - \omega t_0. \tag{6.19}$$

For example, if we consider the particle to be initialised in a superposition of spin states $|+1\rangle$ and $|-1\rangle$ at the origin with zero initial velocity, then we can define the

initial motion of the two arms as:

$$x_1^+(t) = -\left(\frac{B_0}{\eta}+\alpha\right)\cos(\omega t)+\left(\frac{B_0}{\eta}+\alpha\right) \tag{6.20}$$

$$x_1^-(t) = -\left(\frac{B_0}{\eta}-\alpha\right)\cos(\omega t)+\left(\frac{B_0}{\eta}-\alpha\right). \tag{6.21}$$

This is sufficient to yield an initial estimate of the maximum superposition size achievable. Specifically, after the first stage of the evolution, governed by the above two equations, the two trajectories should begin experiencing a relative deceleration at a rate not entirely different to the previously applied relative acceleration. Therefore, the maximum superposition size achievable should be on the order of twice the superposition size achieved during the first phase. The first phase of the evolution ends when the trajectories reach the zero-field region. This point can be roughly estimated here to occur when the mass in the bottom of the potential well[1] which will occur approximately when $\omega t_{zerofield} \approx \frac{\pi}{2} \implies t_{zerofield} \approx \frac{\pi}{2\omega}$. This then gives the maximum superposition size achievable, Δx_{max} as

$$\begin{aligned}\Delta x_{max} \sim & 2\left(x_1^-(\frac{\pi}{2\omega})-x_1^+(\frac{\pi}{2\omega})\right)\\ =&\frac{g e\hbar}{m_e}\frac{\mu_0}{\chi_m m\eta}\\ =&\frac{g e\hbar}{m_e}\frac{\mu_0}{\chi_m m}\frac{2t_{zerofield}}{\pi}\sqrt{-\frac{\chi_m}{\mu_0}}\\ =&\frac{g e\hbar}{\pi m m_e}\sqrt{-\frac{\mu_0}{\chi_m}}t\end{aligned} \tag{6.22}$$

where the time dependence is under the assumption that $t = 2t_{zerofield}$.

Determining the full trajectory will require a more complete analysis for when the switching must occur. As when the magnetic field is given by Eq. 6.7, there will be no spin dependant acceleration and thus it is desirable to minimise $\tau_4 - \tau_1$. To do this, the initial evolution, $x_1(t)$, should be maintained for as long as possible while still ensuring that Eq.6.4 is satisfied. As the particle approaches the boundary set

[1] It will occur slightly to the left or right of this point depending on the internal spin state. This is because the spin-dependent SG effect displaces the centre of the well. As this is only to find an order of magnitude estimate to the superposition size, it is suitable to ignore this.

by Eq.6.4, the magnetic field is modified. Specifically, this is done as the magnetic field experienced by the forward most trajectory approaches B_1, that is:

$$x_1^-(t \approx \tau_1) = \frac{B_0 - B_1}{\eta}, \tag{6.23}$$

where $x_1^{+/-}(\tau_1) = A_1^{+/-}\cos(\omega\tau_1) + c_1^{+/-}$.

Similarly, the non-zero magnetic field gradient should be returned as soon as possible while ensuring Eq. 6.4 holds. As such, the magnetic field gradient should begin being restored as the magnetic field experienced by the rearmost trajectory ($x_2^-(t)$) approximately the magnetic field as given by Eq. 6.8, that is:

$$\begin{aligned} B_1 =& -B_0 + \eta x_2^+(\tau_3) \\ x_2^+(t \approx \tau_3) =& \frac{B_1 - B_0}{\eta} \end{aligned} \tag{6.24}$$

where x_2^+ and x_2^- are the trajectories when $t \in [\tau_1, \tau_4]$, which will need to be found by numerically integrating the equations of motion.

The final two stages of the trajectories will then be given by:

$$x_3^+(t) = A_3^+\cos\left(\omega t + \phi_3^+\right) + C_3^+, \tag{6.25}$$

$$x_3^-(t) = A_3^-\cos\left(\omega t + \phi_3^-\right) + C_3^-, \tag{6.26}$$

$$x_4^+(t) = A_4^+\cos\left(\omega t + \phi_4^+\right) + C_4^+, \tag{6.27}$$

$$x_4^-(t) = A_4^-\cos\left(\omega t + \phi_4^-\right) + C_4^-, \tag{6.28}$$

where

$$
\begin{aligned}
A_3^+ &= -\left(C_3^+ - x_2^+(\tau_2)\right)\left(1+\frac{\left(v_2^+(\tau_2)\right)^2}{\omega^2}\left(C_3^+ - x_2^+(\tau_2)\right)^{-2}\right)^{1/2}, \\
A_3^- &= -\left(C_3^- - x_2^-(\tau_2)\right)\left(1+\frac{\left(v_2^-(\tau_2)\right)^2}{\omega^2}\left(C_3^- - x_2^-(\tau_2)\right)^{-2}\right)^{1/2}, \\
\phi_3^+ &= \tan^{-1}\left(\frac{v_2^+(\tau_2)}{\omega\left(C_3^+ - x_2^+(\tau_2)\right)}\right) - \omega\tau_2, \\
\phi_3^- &= \tan^{-1}\left(\frac{v_2^-(\tau_2)}{\omega\left(C_3^+ - x_2^-(\tau_2)\right)}\right) - \omega\tau_2, \\
C_3^+ &= -\left(\frac{B_0}{\eta} - \alpha\right), \\
C_3^- &= -\left(\frac{B_0}{\eta} + \alpha\right),
\end{aligned}
\tag{6.29}
$$

and

$$
\begin{aligned}
A_4^+ &= -\left(C_4^+ - x_3^+(\tau_3)\right)\left(1+\frac{\left(v_3^+(\tau_3)\right)^2}{\omega^2}\left(C_4^+ - x_3^+(\tau_3)\right)^{-2}\right)^{1/2}, \\
A_4^- &= -\left(C_4^- - x_3^-(\tau_3)\right)\left(1+\frac{\left(v_3^-(\tau_3)\right)^2}{\omega^2}\left(C_3^- - x_3^-(\tau_3)\right)^{-2}\right)^{1/2}, \\
\phi_4^+ &= \tan^{-1}\left(\frac{v_3^+(\tau_3)}{\omega\left(C_4^+ - x_3^+(\tau_3)\right)}\right) - \omega\tau_3, \\
\phi_4^- &= \tan^{-1}\left(\frac{v_3^-(\tau_3)}{\omega\left(C_4^+ - x_3^-(\tau_3)\right)}\right) - \omega\tau_3, \\
C_4^+ &= -\left(\frac{B_0}{\eta} + \alpha\right), \\
C_4^- &= -\left(\frac{B_0}{\eta} - \alpha\right).
\end{aligned}
\tag{6.30}
$$

The values for the times τ_3 and τ_4 are fixed by the following conditions:

1. $\Delta x(\tau_4) = x_4^+(\tau_4) = x_4^-(\tau_4)$ and $\Delta v(\tau_4) = v_4^+(\tau_4) = v_4^-(\tau_4)$, such that the two arms of the interferometers are brought together to overlap in both the position and the momentum space, respectively.

2. $x_4^+(\tau_4) > \frac{B_0+\varepsilon}{\eta}$, such that the Majorana spin flip region of the magnetic field is avoided.

The appropriate times to solve the above conditions, and the motion in the second, third and fourth phases ($\tau_1 \leq t < \tau_4$) was solved numerically as discussed below.

6.3.3.2 Numerical Solution

Given the general trajectories when $t \neq [\tau_1, \tau_4)$ are known, up to the initial conditions, it is now necessary to determine the trajectory in the unsolved region. To do this, a fourth order Runge-Kutta algorithm was used. This involves discretising the position and velocity into a set of parameters. The position and velocity at the $n+1$th step is then defined as

$$x_{n+1} = x_n + \frac{1}{6}\left(k_{x1} + 2k_{x2} + 2k_{x3} + k_{x4}\right) \tag{6.31}$$

$$v_{n+1} = v_n + \frac{1}{6}\left(k_{v1} + 2k_{v2} + 2k_{v3} + k_{v4}\right) \tag{6.32}$$

where

$$k_{v1} = a\left(x_n, t_n\right)\mathrm{d}t \tag{6.33}$$

$$k_{x1} = v_n \mathrm{d}t \tag{6.34}$$

$$k_{v2} = a\left(x_n + \frac{k_{x1}}{2}, t_n + \frac{\mathrm{d}t}{2}\right)\mathrm{d}t \tag{6.35}$$

$$k_{x2} = \left(v_n + \frac{k_{v1}}{2}\right)\mathrm{d}t \tag{6.36}$$

$$k_{v3} = a\left(x_n + \frac{k_{x2}}{2}, t_n + \frac{\mathrm{d}t}{2}\right)\mathrm{d}t \tag{6.37}$$

$$k_{x3} = \left(v_n + \frac{k_{v2}}{2}\right)\mathrm{d}t \tag{6.38}$$

$$k_{v4} = a\left(x_n + k_{x3}, t_n + \mathrm{d}t\right)\mathrm{d}t \tag{6.39}$$

$$k_{x4} = \left(v_n + k_{v3}\right)\mathrm{d}t \tag{6.40}$$

where $\mathrm{d}t$ is the time step size. This integration method was chosen as it provided a suitably high order integration to provide accurate results without exceedingly small values of $\mathrm{d}t$ which otherwise dramatically increase run-time.

The primary input into this numerical integration is then the initial conditions x_1, v_1 and t_1; and the acceleration, which is determined by the equation of motion

derived from the Hamiltonian. Remembering again

$$H_x = \frac{1}{2m}p_x^2 - \frac{\chi_m m}{2\mu_0}B_x(x,t)^2 - \frac{g\not{e}\hbar}{2m_e}S_x B_x(x,t). \tag{6.41}$$

where it is assumed other components of the magnetic field can be ignored. The equation of motion can then be derived using

$$\dot{x} = \frac{\partial H_x}{\partial p} \tag{6.42}$$

$$\dot{p} = -\frac{\partial H_x}{\partial x}. \tag{6.43}$$

These yields

$$\dot{x} = \frac{p}{m} \tag{6.44}$$

$$\implies \ddot{x} = \frac{\dot{p}}{m} \tag{6.45}$$

$$\dot{p} = \frac{\chi_m m}{2\mu_0}B_x(x,t)\partial_x B_x(x,t) + \frac{g\not{e}\hbar}{2m_e}S_x\partial_x B_x(x,t) \tag{6.46}$$

$$\implies \ddot{x} = \frac{\chi_m}{2\mu_0}B_x(x,t)\partial_x B_x(x,t) + \frac{g\not{e}\hbar}{2mm_e}S_x\partial_x B_x(x,t) \tag{6.47}$$

allowing for the acceleration used in the integration to be identified as $a(x,t) = \ddot{x}$. The method used to find the full trajectories was:

1. The initial conditions for both arms we taken to be $t = 0$, $x = 0$ and $v = 0$, this was used to define x_1^+ and x_1^- using the analytic forms provided above.

2. This was then used to find the parameter T_1, defined as $x_1^-(t = T_1) = \frac{B_0 - B_1}{\eta}$. From this, the values of τ_1 and τ_2 can be found. This was done using the fact that $Sw(\tau, -\infty, T_1) \approx 1 \; \forall \; \tau \leq \tau_1$ and $Sw(\tau, -\infty, T_1) \approx 0 \; \forall \; \tau \geq \tau_2$.

3. The numerical integration was used to find x_2^+ under the assumption that $\tau_3 = \infty$ and using the numerical solution for $x_1^+(t = \tau_1)$ and the associated velocity and time as the initial condition. This was used to define the second time parameter T_2 using $x_2^+(t = T_2) = \frac{B_1 - B_0}{\eta}$. Similar to the previous step, this was used to define τ_3 and τ_4.

4. The numerical integration for x_2^+ was then re-performed, now with the actual values of τ_3 and τ_4. x_2^- was also calculated numerically. This then provides the full trajectories from $t = 0$ until $t = \tau_4$ with $x_1 =^{+/-}$ being calculated analytically, providing the trajectory when $t < \tau_1$. $x_2 =^{+/-}$ is then the numerically calculated trajectories which hold for $\tau_1 \leq t < \tau_4$. The experienced magnetic field was calculated throughout this stage of the evolution to ensure the minimum experienced magnetic field was never too low, as shown in Figure 6.1b.

5. The analytic solutions can be used for the remaining sections of the trajectories, $x_3 =^{+/-}$ and $x_4 =^{+/-}$. The time at which the spin-flip occurs, τ_5, and when the interferometer is closed, τ_6, are still to be determined. This is done by first guessing a value for τ_5 (typically taken to be $\tau_5 = 2\tau_4$). This can then be used to solve for the trajectories and determine and estimate for τ_6 by taking $\Delta v(t = \tau_6) = 0$ where $\Delta v(t)$ is the velocity difference between the two arms of the interferometer. $\Delta x(\tau_6)$ was then calculated and used to improve the guessed value of τ_5. This was done by noting that increasing τ_5 decreases the value of $\Delta x(\tau_6)$ and vice versa. The above process was repeated until $\Delta x(\tau_6)$ was suitably close to zero, remembering that by definition $\Delta v(\tau_6) = 0$.

6. Finally the full trajectory was assembled piecewise out of $x_1 =^{+/-}$, $x_2 =^{+/-}$, $x_3 =^{+/-}$ and $x_4 =^{+/-}$. It was also checked that the superposition will close *before* the trajectories enter the zero-field region a second time and that the resulting magnetic field experienced throughout the evolution was never below ε.

An example of the resulting trajectory and superposition size can be seen in Figure 6.3. Figure 6.4 shows how the maximum superposition size scales with time, mass and magnetic field gradient.

It was noted that typically for masses $m \geq 10^{-17}$ kg, the primary driver of the motion is the diamagnetic effect $\propto |\vec{B}(x,y)|^2$, while the NV centre coupling, $\propto \vec{\mu}_\pm \cdot \vec{B}$, serves to slightly displace the potential well created by the induced dia-

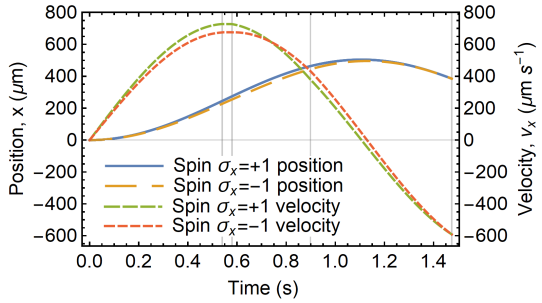

(a) Paths through the interferometer for each arm of the interferometer. This shows both the position and velocity changes with time .

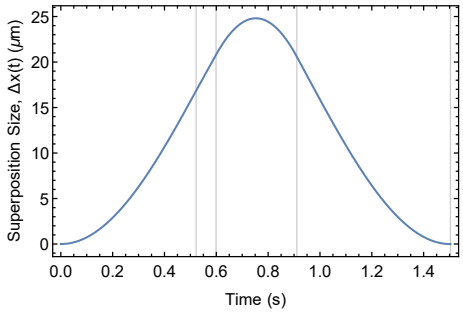

(b) Superposition size $\Delta x(t)$ and velocity difference $\Delta v(t)$ with time.

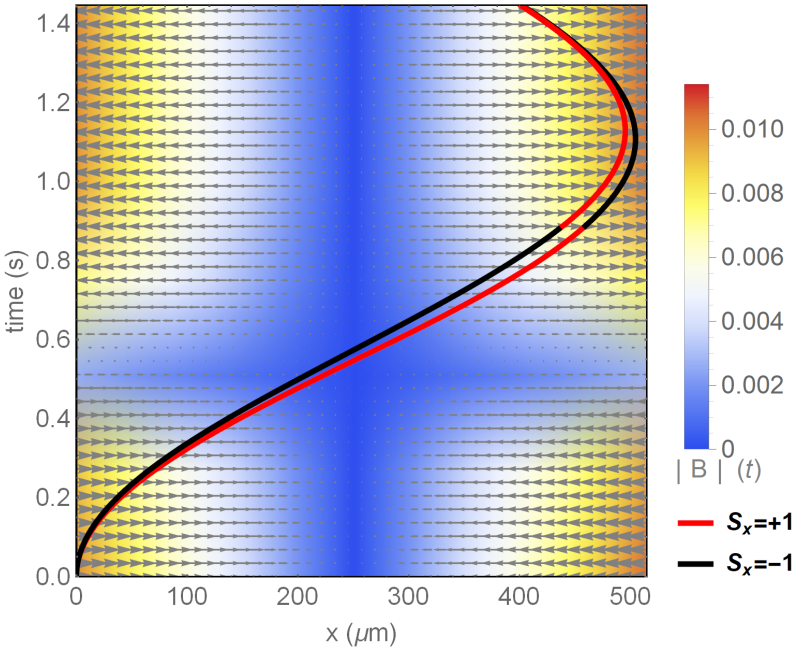

(c) Example interferometer path trajectories through the varying magnetic fields used. The magnetic field transition time here is accentuated for readability. Note that the internal spin states are reversed at time $t \approx 0.9$ s to ensure the interferometer is closed.

Figure 6.3: Figures showing both the position and velocity through the interferometer (Figure 6.3a), and the superposition size (Figure 6.3b) with time; and the trajectories through the magnetic field (Figure 6.3c). These plots are the result of the full analytic and numerical analysis.The vertical grey lines represent times τ_i for $i = 1,2,3,4$. The figures are for $B_0 = 10^{-2}$ T, $\eta = 46.483$ Tm^{-1} and $m = 10^{-16}$ kg.

magnetism. As such, we can expect both the interferometer arms to have a similar path w.r.t a centre of mass motion of both the states dictated by the diamagnetic effect. While the NV centre coupling leads to a small perturbation from the centre of mass motion, thus creating a spatial superposition.

When the masses are confined to a harmonic oscillator potential, the wave function will not spread during the evolution when employing a coherent state. Furthermore, it is sufficient to consider the centre of mass as following the classical trajectory, and any thermal fluctuations in the initial state do not limit the coherence in the final state as they factor out of the motion, see for the discussion in [4].

6.3.4 Discussion of Superposition size achievable

By evaluating the trajectory for various mass particles, and employing various magnetic field gradient it was possible to find some general scaling behaviour. The final time τ_6, was determined to be

$$\tau_6 \approx 58.5 \times (1\ \mathrm{Tm}^{-1}/\eta)\ \ \mathrm{sec}\,, \tag{6.48}$$

to ensure that the relative positions of the two paths $\Delta x(t = \tau_6) = 0$ m, and the relative velocity $\Delta v(t = \tau_6) = 0$ ms^{-1}. Furthermore, the maximum superposition which occurs between $\tau_4 < t < \tau_5$ can be determined numerically:

$$\Delta x(m, \tau_6) \approx \left(\frac{1.6 \times 10^{-16}\ \mathrm{Kg}}{m}\right)\left(\frac{\tau_6}{1\ \mathrm{sec}}\right) \times 10^{-6}\ \mathrm{m} \tag{6.49}$$

for $B_0 = 10^{-2}$ T, $B_1 = 100\varepsilon$ and $m \gtrsim 10^{-17}$ kg. The latter condition on the mass arises because the induced diamagnetic term does not dominate the NV centre potential. This is because the diamond's small mass and hence volume determines the induced diamagnetic potential. For a lighter diamond, if we do not modify the times $\tau_i(\eta)$ and B_1, the masses would inevitably move through the zero-field region of the magnetic field, and therefore demands a different magnetic field setup, see [3, 27]. Therefore, our analysis holds true for $m \geq 10^{-17}$ kg for $\chi_m \approx -6.2 \times 10^{-9}$ kgm^{-3}. Using Eq.6.49 we can estimate that achieving a superposition size of 20 μm with a

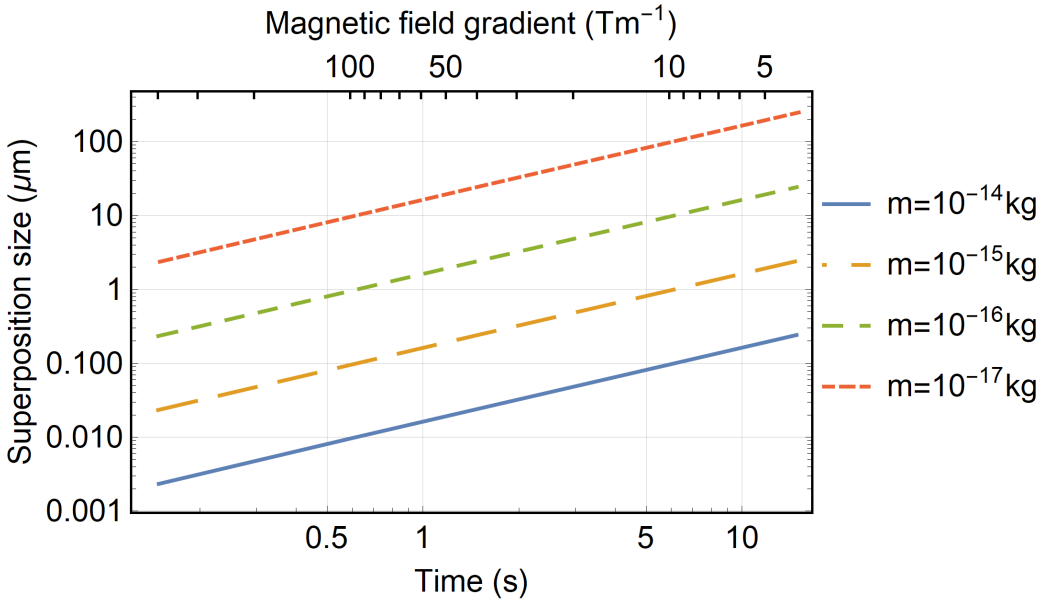

Figure 6.4: Maximum superposition size achievable with time. This was determined numerically by calculating the full paths through the interferometer. Note that for masses $m = 10^{-17}$ kg and heavier these results are well approximated by Eq. 6.49.

10^{-16} kg mass requires a total time of $\tau_6 \sim 1.6 = 1.25$ s, which corresponds to the magnetic field gradient $\eta \sim 46.8$ Tm^{-1}, again using $B_0 = 10^{-2}$ T and $B_1 = 100\varepsilon$, which can be achieved in a laboratory [27].

It is also work comparing this result to the previously estimated maximum superposition size, as given by Equation 6.22 which evaluates to

$$\Delta x(m, \tau_6) \approx \left(\frac{1.7 \times 10^{-16}\ \text{Kg}}{m}\right)\left(\frac{\tau_6}{1\ \text{sec}}\right) \times 10^{-6}\ \text{m} \tag{6.50}$$

and as such provides an intuitive explanation for the full superposition size scaling observed.

6.3.5 Fluctuations in set-up

Here I will present an analysis of fluctuations within the proposed interferometric set-up. To do so, the equations of motion need to be determined. For simplicity, once again, only a single dimension is considered for the moment, with the one

dimensional Hamiltonian given by

$$H_x = \frac{1}{2m}p^2 - \frac{\chi_m m}{2\mu_0}\left(B_0 + \eta x\right)^2 - \mu_B S_x \eta \tag{6.51}$$

where each variable is taken to be only the x component of the full vector and the x component of the magnetic field is taken to be $B(x) = B_0 + \eta x$. For this, treating the motion classically, we can write down the equations of motion for the variables x and p using

$$\dot{x} = \frac{\partial H_x}{\partial p} \tag{6.52}$$

$$\dot{p} = -\frac{\partial H_x}{\partial x}. \tag{6.53}$$

These yields

$$\dot{x} = \frac{p}{m} \tag{6.54}$$

$$\implies \ddot{x} = \frac{\dot{p}}{m} \tag{6.55}$$

$$\dot{p} = m\eta\chi_m\left(B_0 + \eta x\right) + \eta\mu_B S_x \tag{6.56}$$

$$\implies \ddot{x} = \eta\chi_m\left(B_0 + \eta x\right) + \frac{\eta\mu_B}{m}S_x. \tag{6.57}$$

Now the above can be repeated, taking linear perturbations of the parameters and keeping only the first order terms in the perturbations. In general I will write the perturbed parameter X as $X + \delta X$:

$$\delta H_x = \frac{1}{2m}\left(p + \delta p\right)^2 - \frac{\chi_m m}{2\mu_0}\left(B_0 + \delta B_0 + \left(\eta + \delta\eta\right)\left(x + \delta x\right)\right)^2 - \mu_B S_x\left(\eta + \delta\eta\right). \tag{6.58}$$

Of course there are other sources of noise such as timing uncertainties in both the spin flipping microwave pulse, as well as the timing for when the magnetic field is changed. The mass may also changed from one run to the next, however, for the moment a fixed mass will be taken. This is done as I am here focused on determining what is indeed possible, by say, recycling the interferometric particle.

Leaving future projects to determine how well any signal can be improved by using a higher flux of particles. Once again, the equation of motion for the perturbed position coordinate is

$$\frac{\partial^2}{\partial t^2}(x+\delta x) = \frac{\chi_m}{\mu_0}\left(x\eta^2 + 2x\delta\eta\,\eta + \delta\eta B_0 + \eta\,\delta B_0 + \eta B_0\right) + \frac{S_x\mu_B}{m}(\eta+\delta\eta) \tag{6.59}$$

from which we can define the equation of motion for just the position fluctuation as

$$\begin{aligned}\frac{\partial^2}{\partial t^2}\delta x =& \frac{\partial^2}{\partial t^2}(x+\delta x) - \frac{\partial^2}{\partial t^2}x & (6.60)\\ =& \frac{\chi_m}{\mu_0}(2x\delta\eta\,\eta + \delta\eta B_0 + \eta\,\delta B_0) + \frac{S_x\mu_B}{m}\delta\eta + \frac{\chi_m}{\mu_0}\eta\,\delta B_0 \equiv a_\eta^\pm + a_{B_0}^\pm & (6.61)\end{aligned}$$

where the $\pm$ superscript identifies which arm of the interferometer it corresponds to and $a_\eta^\pm(a_{B_0}^\pm)$ contain all terms which are a function of the fluctuations in gradient (bias field), $\delta\eta$ (δB_0).

The purpose of this analysis is to determine how well the two arms will overlap, thus the parameter of interest is

$$\delta\Delta x(t) = \delta x^1(t) - \delta x^+(t) \tag{6.62}$$

which corresponds to the uncertainty in the superposition size at time t. In an ideal interferometer $\delta\Delta x(t = t_{\text{final}}) = 0$ and for any coherent output to be possible $\delta\Delta x(t_{\text{final}}) \ll \sigma_x$ where σ_x is the fundamental position uncertainty in the particle wave function.

Taking first a_{B_0}, we can see what effects slight perturbations in the bias field have on the ability to close the interferometer. This yields

$$\begin{aligned}\delta\Delta x(t_{\text{final}})_{B_0} =& \int_0^t \mathrm{d}u' \int_0^{u'} \mathrm{d}u\; a_{B_0}^+ - a_{B_0}^- \\ =& 0 \end{aligned} \tag{6.63}$$

such that, to the first order, δB_0 does not contribute to any position difference uncertainty throughout the evolution. This is not to say it does not lead to any potential

issues. For example, phase fluctuations due to the varying position and geometry of the interferometer and concerns regarding the minimum magnetic field experienced throughout the interferometry process as shown below. However, these issues are secondary to what is being considered here.

This means that δB_0 errors act as a stochastic shift in the entire interferometer. This will show up as noise in any output phases which are position-dependent. The size of the phase fluctuation will thus depend on not just δB_0, but also the nature of the distance scaling in the phase term and likely the average distance itself.

Now considering a_η

$$\begin{aligned}
\delta\Delta x_\eta(t) =& \int_0^t \mathrm{d}u' \int_0^{u'} \mathrm{d}u\; a_\eta^+(u) - a_\eta^-(u) \\
=& \int_0^t \mathrm{d}u' \int_0^{u'} \mathrm{d}u\; \frac{\chi_m}{\mu_0}\left(2x^+(u)\delta\eta(u)\eta + \delta\eta(u)B_0 + \eta\,\delta B_0\right) + \frac{|S_x(u)|\mu_B}{m}\delta\eta(u) \\
& - \int_0^t \mathrm{d}u' \int_0^{u'} \mathrm{d}u\; \frac{\chi_m}{\mu_0}\left(2x^-(u)\delta\eta(u)\eta + \delta\eta(u)B_0 + \eta\,\delta B_0(u)\right) - \frac{|S_x(u)|\mu_B}{m}\delta\eta(u) \\
=& 2\frac{\chi_m\eta}{\mu_0}\int_0^t \mathrm{d}u' \int_0^{u'} \mathrm{d}u\; \Delta x(u)\delta\eta(u) + 2\frac{|S_x(u)|\mu_B}{m}\int_0^t \mathrm{d}u' \int_0^{u'} \mathrm{d}u\; \delta\eta(u) \\
=& \delta\Delta x_\eta^{\mathrm{dia}}(t) + \delta\Delta x_\eta^{\mathrm{NV}}(t)
\end{aligned} \tag{6.64}$$

where as only first order perturbations are currently being considered, the unperturbed time dependent superposition size is used inside the integral and the gradient perturbation effects are separated into those arising due to the diamagnetic coupling $\delta\Delta x_\eta^{\mathrm{dia}}(t)$ and due to the NV $\delta\Delta x_\eta^{\mathrm{NV}}(t)$. These can be used to provide an estimate for the stability required to ensure reasonable interference contrast in the output. By noting that $\Delta x(u) \leq \Delta x_{max}$ and ignoring the fluctuating magnetic field gradient when $t \in [t_1, \tau_4)$ gives

$$\delta\Delta x_\eta(\tau_6) \approx \left(\frac{\chi_m\eta\Delta x_{max}}{\mu_0} + \frac{|S_x(u)|\mu_B}{m}\right)\tau_6^2\delta\eta. \tag{6.65}$$

This is also not taking into account the frequency spectrum of the noise. Doing so leads to an upper bound by considering all noise in the most malicious frequency range. Given $\delta\Delta x_\eta(\tau_6) \ll \sigma_x$ for the states to overlap significantly, magnetic field

gradient fluctuations must obey the relation

$$\begin{aligned}\delta\eta \ll & \sigma_x \left(\frac{\chi_m \eta \Delta x_{max}}{\mu_0} + \frac{|S_x(u)|\mu_B}{m} \right)^{-1} \tau_6^{-2} \\ = & \sigma_x \left(\frac{ge\hbar}{mm_e} + \frac{ge|S_x(u)|\hbar}{2mm_e} \right)^{-1} \tau_6^{-2} \\ \implies \delta\eta \ll & \sigma_x \frac{2mm_e}{3\hbar ge\tau_6^2}\end{aligned} \tag{6.66}$$

where I have estimated the maximum superposition size using Equation 6.22.

6.3.6 Spin Phase Evolution

It is not just variation in the overlap of the two wave packets which must be taken into account. The output phase must also be stable enough for a signal to be read out for such a device to be useful for the applications considered throughout this thesis. As such, it is necessary to determine the output signal expected from such an interferometer. This is done by considering the phase evolution difference between the two paths taken through the interferometer. The final output signal will be a function of the difference of the phase accumulated along each of the paths through the interferometer. This path phase difference will arise due to external forces acting on the masses. This includes gravitational or electromagnetic interactions which differ across the paths taken through the interferometer. As well as any momentum disparity of the mass through each trajectory due to the trajectories themselves. For the moment, I will neglect the former external sources and focus on only the intrinsic path phase difference. The external factors are highly implementation dependant and may amount to signals in such devices (see Ch. 4). Given that the entire Hamiltonian is used to determine the trajectories, it is sufficient to calculate the action for a *free* spin travelling along fixed trajectories which are given by the two possible classical trajectories through the interferometer. This will then yield a phase, θ accumulated along a path γ of

$$\theta = \frac{1}{\hbar} \int_\gamma \frac{p(t)^2}{2m} \mathrm{d}t \tag{6.67}$$

where $p(t)$ is the time-dependent momentum of the particle.

To evaluate this, the motion can be broken into three distinct segments: $\tau_0 = 0 \leq t \leq \tau_1$, before the particle has reached the zero-field region; $\tau_4 < t \leq \tau_5$, after the particle has reached the zero-field region but before the spin has been reversed; and $\tau_5 < t \leq \tau_6$, the remainder of the evolution, ending when the two wave packets are brought to overlap. This ignores the brief period when the motion in not solvable analytically. As this period ($t \in (\tau_1, \tau_4]$) is brief and only order of magnitude estimates are necessary at this stage, it should not have a significant impact on the final phase. The general particle momentum for the ith segment can be written as

$$p_i^{+/-}(t) = -m\omega A_i^{+/-} \sin\left(\omega t + \phi_i^{+/-}\right) \tag{6.68}$$

for the $+$ and $-$ arm of the interferometer and where the value of $A_i^{+/-}$ and $\phi_i^{+/-}$ differs from one segment to the next. Thus the phase difference accumulated through any given stage of the interferometer will be

$$\begin{aligned}
\Delta\theta = \sum_{i\in\{1,5,6\}} \Bigg[& \frac{m}{2\hbar} \int_{\tau_{i-1}}^{\tau_i} \left(\omega A_i^+ \sin\left(\omega t + \phi_i^+\right)\right)^2 \\
& - \frac{m}{2\hbar} \int_{\tau_i}^{\tau_{i+1}} \left(\omega A_i^- \sin\left(\omega t + \phi_i^-\right)\right)^2 \Bigg] \\
= & \frac{m\omega}{8\hbar} \left[2\omega\tau_1 - \sin\left(2\omega\tau_1\right)\right] \left[\left(A_1^+\right)^2 - \left(A_1^-\right)^2\right] \\
& + \sum_{i=5}^{6} \frac{m}{8\hbar} \Bigg[2\omega^2 \left(\tau_i - \tau_{i-1}\right) \left(\left(A^+\right)^2 - \left(A^-\right)^2\right) \\
& + \sin\left(2\phi^+ + 2\tau_{i-1}\omega\right) - \sin\left(2\phi^- + 2\tau_{i-1}\omega\right) \\
& - \sin\left(2\phi^+ + 2\tau_i\omega\right) + \sin\left(2\phi^- + 2\tau_i\omega\right) \Bigg]
\end{aligned} \tag{6.69}$$

Now it is suitably insightful to consider in detail the phase difference accrued when

$t \in [\tau_0, \tau_1]$. Given that $\sin(2\omega\tau_1) \approx 0$, the phase difference will be

$$\begin{aligned}
\Delta\theta(t=\tau_1) \approx & \frac{m}{8\hbar}\Big[2\omega^2\tau_1\left(\left(A_1^+\right)^2-\left(A_1^-\right)^2\right) \\
& -\sin(2\tau_1\omega)+\sin(2\tau_1\omega)\Big] \\
= & \frac{m}{8\hbar}2\omega^2\tau_1\left[\left(\frac{B_0}{\eta}+\alpha\right)^2-\left(\frac{B_0}{\eta}-\alpha\right)^2\right] \\
= & \frac{m\tau_1}{\hbar}\omega^2\frac{B_0}{\eta}\alpha \\
= & \frac{m\tau_1}{\hbar}\left(\frac{-\chi_m}{\mu_0}\eta^2\right)\frac{B_0}{\eta}\left(\frac{-ge\hbar}{2m_e}\frac{\mu_0}{\chi_m m\eta}\right) \\
= & \frac{geB_0}{2m_e}\tau_1. \qquad (6.70)
\end{aligned}$$

In each time segment considered here, the particles are simply acting as harmonic oscillators, flipping between two different harmonic wells, the entire path phase difference can be approximated as

$$\Delta\theta \approx \frac{geB_0}{2m_e}\left(\frac{\tau_1}{\tau_6}-\frac{\tau_5-\tau_4}{\tau_6}+\frac{\tau_6-\tau_5}{\tau_6}\right)\tau_6 \qquad (6.71)$$

where the extra terms in equation 6.69 are neglected and the negative multiplying the time difference occurs when the internal spin direction is reversed relative to the external field. As a reminder, this occurs by reversing the field magnitude, not the particle spin state. Thus, for the full trajectories, the path phase difference will be $\Delta\theta \propto \tau_6$. This can be seen clearly in Figure 6.5, which shows the phase scaling linearly with time and almost independently of mass. Figure 6.5 also shows the approximate phase difference given by Equation 6.71 and how it compared to the exact value. This allows for the required stability in the experimental parameters to be estimated, given $\frac{ge}{2m_e} \sim 10^{11}$; to keep the final phase uncertainty $\delta(\Delta\theta) < 1$ will

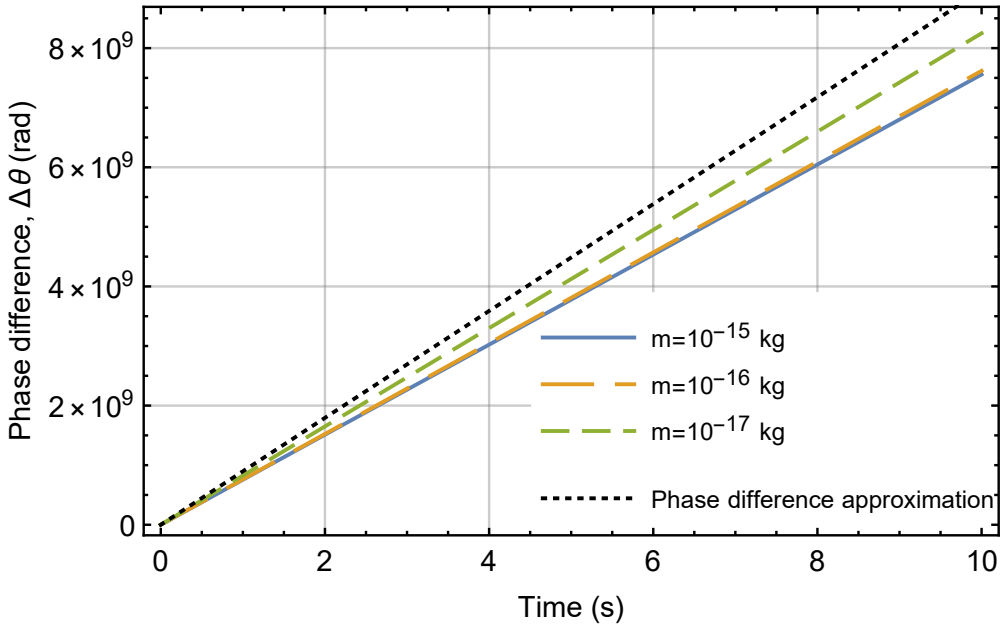

Figure 6.5: Phase difference magnitude scaling with total runtime for $m = 10^{-15}$ kg, $m = 10^{-16}$ kg, and $m = 10^{-17}$ kg. This also shows the phase difference as predicted by Equation 6.71.

require

$$10^{-11}\ \text{Ts} > B_0 \times \delta t \tag{6.72}$$

$$10^{-11}\ \text{Ts} > \delta B_0 \times t. \tag{6.73}$$

This places an strict requirement on both timing certainty, δt; and bias field stability, δB_0. This will serve as a further challenge that must be met before such an experiment can be fully realised.

6.4 Employing An Accelerating Magnetic Field

In this section I will consider what, if any, benefit to the above linear magnetic field proposal by allowing the field to be moved with the particle. I will here consider the x component of the magnetic field to be

$$B_x = -\eta x + B_0(t) \equiv -\eta\,(x - x_0(t)) \tag{6.74}$$

where $x_0(t) = \frac{B_0(t)}{\eta}$ is the controllable zero point of the field. This control can be implemented by simply modifying only the strength of the bias field. Considering the acceleration of a spin s mass at the initial location x_i as $a(x_i, s_x)$:

$$a(x_i, s) = -\frac{\chi_m}{\mu_0}\eta^2 (x_0(t) - x_i) - s_x \frac{g e \hbar}{2 m m_e}\eta. \tag{6.75}$$

If we assume the initial point for the mass is left of the zero point of the field ($x_0(t) > x_i$), then we can see that a spin $s_x = +1$ will have a larger acceleration and so will be the 'front' spatial state. I will take the magnetic field zero-point to be shifted with this same acceleration, $a(x_i, +1)$ and consider the apparent acceleration for a mass with the two spin states of interest ($s_x = \pm 1$). In an accelerating reference frame in which the magnetic field is stationary, the front mass will then also have zero acceleration, $\tilde{a}(x_i, +1) = 0$, while the other spin state will have a position-dependent acceleration of $\tilde{a}(x, -1) = a(x, -1) - a(x_i, +1)$. Thus, the 'rear' mass ($s_x = -1$) will be accelerated in the negative $\tilde{x}$ direction (where $\tilde{x}$ corresponds to the x-axis in the accelerate reference frame). This acceleration will continue until the rear mass reaches $\tilde{x}_a$ where

$$\tilde{a}(\tilde{x}_a, -1) = 0 \tag{6.76}$$

which gives

$$\begin{aligned} 0 =& a(\tilde{x}_a, -1) - a(x_i, +1) \\ =& -\frac{\chi_m}{\mu_0}\eta^2 (x_0 - \tilde{x}_a) + \frac{g e \hbar}{2 m m_e}\eta + \frac{\chi_m}{\mu_0}\eta^2 (x_0 - x_i) + \frac{g e \hbar}{2 m m_e}\eta \\ =& -\frac{\chi_m}{\mu_0}\eta^2 (x_i - \tilde{x}_a) + \frac{g e \hbar}{m m_e}\eta \\ \implies \tilde{x}_a =& x_i - \frac{g e \mu_0 \hbar}{\chi_m m m_e \eta} \end{aligned} \tag{6.77}$$

at which point the mass will be in a spatial superposition of $\Delta x = \frac{g e \mu_0 \hbar}{\chi_m m m_e \eta}$. Upon reaching $\tilde{x}_a$ the rear mass will still have a net velocity, and so the superposition size will continue to grow beyond this. Assuming the average acceleration is approximately the same on either side of $\tilde{a}_a$, the maximum superposition will be approx-

imately $\Delta x_{\max} = \frac{2ge\mu_0\hbar}{\chi_m m m_e \eta}$. This can be compared to the result found above, which, when written as a function of the magnetic field gradient, was

$$\Delta x_{\text{max, stationary field}} = \frac{g\epsilon\hbar}{m_e}\frac{\mu_0}{\chi_m m\eta} \tag{6.78}$$

which is exactly a factor of 2 smaller. However, this does not account for how the total interferometry time compares between the two methods. It does still imply that this is not a satisfactory route to creating significantly larger superposition sizes.

6.5 Analysis of Extended Free-Flight Scheme

Here I present a further modification of the scheme in which the masses are first rapidly accelerated before the magnetic field gradient is removed. This will leave only a constant bias field in which the magnetic field will be due only to the constant bias field and will not affect the particle motion. I will take a mass m in a superposition of ± 1 electronic spin states. The initial location is set as x_0 at time $t_0 = 0$ and subject to an external magnetic field $B_x = \eta x + B_0$. Throughout, only the motion in the x direction will be considered. It is known that the mass will oscillate in a diamagnetic harmonic trapping potential with frequency $\omega = \sqrt{\frac{-\chi_m}{\mu_0}}\eta$ where $\chi_m < 0$ is the mass magnetic susceptibility. This will lead the mass to evolve along two superposed trajectories given by

$$x^{\pm}(t) = A^{\pm}\cos\left(\omega t + \phi^{\pm}\right) + c^{\pm} \tag{6.79}$$

where the $+$ and $-$ superscript denote the initial spin stated and

$$A^{\pm} = -\left(c^{\pm} - x_0^{\pm}\right)\left[1 + \left(\frac{v_0^{\pm}}{\omega^2}\right)^2\left(c^{\pm} - x_0^{\pm}\right)^{-2}\right]^{1/2} \tag{6.80}$$

$$\phi^{\pm} = \tan^{-1}\left(\frac{v_0^{\pm}}{\omega\left(c^{\pm} - x_0\right)}\right) - \omega t_0 \tag{6.81}$$

$$c^{\pm} = \frac{B_0}{\eta} \pm \frac{g\epsilon\hbar\mu_0}{2m_e\chi_m m\eta} \tag{6.82}$$

where x_0, v_0 and t_0 are the initial conditions. For simplicity are set to $x_0 = 0$ m, $v_0 = 0$ ms^{-s} and $t_0 = 0$ s which gives

$$A^{\pm} = -c^{\pm} \tag{6.83}$$

$$\phi^{\pm} = 0 \tag{6.84}$$

$$c^{\pm} = \frac{B_0}{\eta} \pm \frac{g\hbar\mu_0}{2m_e\chi_m m\eta} \tag{6.85}$$

Thus the position difference between the two trajectories is

$$\begin{aligned}
\Delta x(t) &= \left(A^+ - A^-\right)\cos(\omega t) + \left(c^+ - c^-\right) \\
&= -\frac{g\hbar\mu_0}{m_e\chi_m m\eta}\cos(\omega t) + \frac{g\hbar\mu_0}{m_e\chi_m m\eta} \\
&= -\frac{g\hbar\mu_0}{m_e\chi_m m\eta}\cos(\omega t) + \frac{g\hbar\mu_0}{m_e\chi_m m\eta} \\
&= -\frac{g\hbar\mu_0}{m_e\chi_m m\eta}\left(\cos(\omega t) - 1\right).
\end{aligned} \tag{6.86}$$

Therefore, the maximum superposition size of $\Delta x_{max} = \frac{2g\hbar\mu_0}{m_e\chi_m m\eta}$ occurs at $t = \frac{\pi}{\omega}$. The maximum velocity difference is given by

$$\begin{aligned}
\Delta v(t) &= -\omega\left(A^+ - A^-\right)\sin(\omega t) \\
&= \omega\frac{g\hbar\mu_0}{m_e\chi_m m\eta}\sin(\omega t)
\end{aligned} \tag{6.87}$$

which reaches its maximum value $\Delta v_{max} = \omega\frac{g\hbar\mu_0}{m_e\chi_m m\eta} = -\frac{g\hbar}{m_e m}\sqrt{\frac{-\mu_0}{\chi_m}}$ at $t = \frac{\pi}{2\omega} \equiv t_a$. Note that $t_a = \frac{\pi}{2\omega} = \frac{\pi}{2\eta}\sqrt{\frac{-\mu_0}{\chi_m}}$ which implies $\eta = \frac{\pi}{2t_a}\sqrt{\frac{-\mu_0}{\chi_m}}$. This time also corresponds approximately with when the trajectories enter the zero field region of the field, at which time the superposition size is given by $\Delta x(t = t_a)\frac{g\hbar\mu_0}{m_e\chi_m m\eta}$. If at this time, the magnetic field gradient is switched off, the masses will propagate freely at a constant velocity for a time t_f. Thus at time $t = t_a + t_f$, the superposition size will

be

$$\begin{aligned}\Delta x(t=t_a+t_f) =& \frac{g\hbar\mu_0}{m_e\chi_m m\eta} - \frac{g\hbar}{m_e m}\sqrt{\frac{-\mu_0}{\chi_m}}t_f \\ =& -\frac{g\hbar}{m_e m}\sqrt{\frac{-\mu_0}{\chi_m}}\frac{2}{\pi}t_a - \frac{g\hbar}{m_e m}\sqrt{\frac{-\mu_0}{\chi_m}}t_f \\ =& -\frac{g\hbar}{m_e m}\sqrt{\frac{-\mu_0}{\chi_m}}\left(\frac{2}{\pi}t_a + t_f\right)\end{aligned} \tag{6.88}$$

This still leaves the problem of closing the interferometer. To determine how this can be achieved, we can consider the general problem of how to close an interferometer starting with a general spatial and velocity difference:

$$\begin{aligned}\Delta x(t) =& A^+\cos\left(\omega t+\phi^+\right) - A^-\cos\left(\omega t+\phi^-\right) + c^+ - c^- \\ \Delta v(t) =& -\omega\left[A^+\sin\left(\omega t+\phi^+\right) - A^-\sin\left(\omega t+\phi^-\right)\right]\end{aligned} \tag{6.89}$$

which, for the interferometer to be closed requires:

$$0 = A^+\cos\left(\omega t+\phi^+\right) - A^-\cos\left(\omega t+\phi^-\right) + c^+ - c^- \tag{6.90}$$

and

$$0 = -\omega\left[A^+\sin\left(\omega t+\phi^+\right) - A^-\sin\left(\omega t+\phi^-\right)\right]. \tag{6.91}$$

Starting with the second condition gives

$$\begin{aligned} 0 =& -\omega\left[A^+\sin\left(\omega t+\phi^+\right) - A^-\sin\left(\omega t+\phi^-\right)\right] \\ 0 =& A^+\sin\left(\omega t+\phi^+\right) - A^-\sin\left(\omega t+\phi^-\right) \\ A^+\sin\left(\omega t+\phi^+\right) =& A^-\sin\left(\omega t+\phi^-\right) \\ \frac{A^+}{A^-} =& \frac{\sin\left(\omega t+\phi^-\right)}{\sin\left(\omega t+\phi^+\right)} \\ \Longrightarrow\ A^+ =& A^-\frac{\sin\left(\omega t+\phi^-\right)}{\sin\left(\omega t+\phi^+\right)}\end{aligned} \tag{6.92}$$

which can be substituted into the first condition to give

$$\begin{aligned}
0 =& A^{+}\cos\left(\omega t+\phi^{+}\right)-A^{-}\cos\left(\omega t+\phi^{-}\right)+c^{+}-c^{-}\\
0 =& A^{-}\frac{\sin\left(\omega t+\phi^{-}\right)}{\sin\left(\omega t+\phi^{+}\right)}\cos\left(\omega t+\phi^{+}\right)-A^{-}\cos\left(\omega t+\phi^{-}\right)+c^{+}-c^{-}\\
0 =& A^{-}\left(\sin\left(\omega t+\phi^{-}\right)\cot\left(\omega t+\phi^{+}\right)-\cos\left(\omega t+\phi^{-}\right)\right)+c^{+}-c^{-}\left(c^{-}-c^{+}\right).
\end{aligned} \tag{6.93}$$

Finally, this can be solved for t, taking the positive solution

$$\begin{aligned}
t =& \frac{1}{\omega}\cos^{-1}\left(\frac{\sqrt{\left(c^{+}-c^{-}\right)^{2}\cos^{2}\left(\phi^{+}\right)\left(\left(A^{-}\right)^{2}\cos\left(2c^{+}-2c^{-}\right)+2\left(c^{+}-c^{-}\right)^{2}-\left(A^{-}\right)^{2}\right)}}{\sqrt{2}\left(c^{+}-c^{-}\right)^{2}}\right.\\
&\left.+\frac{A^{-}\sin\left(\phi^{+}\right)\sin\left(\phi^{+}-\phi^{-}\right)}{\left(c^{+}-c^{-}\right)}\right).
\end{aligned} \tag{6.94}$$

Thus it should be possible to close the interferometer, provided the final time is chosen such that the above holds. Note also that the terms $A^{+/-}$, $\phi^{+/-}$ and $c^{+/-}$ will be determined by both the initial acceleration period and how long the masses are allowed to propagate freely.

Therefore, a maximum superposition size of $\Delta x_{max}\approx-\frac{g\hbar}{m_e m}\sqrt{\frac{-\mu_0}{\chi_m}}T$ where T is the total interferometry time is achievable. This is under the assumption that the mass is rapidly accelerated and decelerated, such that $t_f\approx T$. This is only a factor of π larger than what is achievable using the original method detailed above, as given in Equation 6.22.

Taken as a whole, it appears that the induced diamagnetism presents a severely limiting factor to using the Stern-Gerlach effect for massive particle interferometry. In every case considered, the maximum spatial superposition size is inversely proportional to the magnetic field gradient η. Given η is proportional to the applied SG force, this represents a fundamental limitation to the splitting achievable without going well beyond what is achievable here. Given this, more work is clearly needed before such devices can implement the QGEM protocol. However, as presented here, SG interferometry still promises to probe a new regime of large mass,

large spatial superpositions and massive particle interferometry.

6.6 Diamagnetic Repulsion

One further method to potentially create a large spatial splitting is to try to leverage the strong effect of diamagnetism to instead amplify an initial, small Stern-Gerlach sourced spatial split. The most obvious manner of achieving this would be to place a current carrying wire in between the two spatial states. This will naturally provide an equal strength diamagnetic repulsion. During this, the internal spins can be mapped to nuclear spins states as the negligible spin-magnetic field coupling is actively desirable and this may allow longer spin coherence times. I will begin this section by analysing what a wire sourced diamagnetic repulsion might look like, before presenting a possible form of the general scheme.

I will take an initial state with a pre-existing spatial splitting. Both position states and the wire are assumed to lie on the x axis once again simplifying the problem to a 1 dimensional one as I am here interested in only the general concept. The coherent spin is taken to be mapped to a nuclear spin and thus the spin magnetic field coupling is ignored. The centre of the wire is placed at $x = 0$ with the two position states located at $\pm x_0$ where $x_0 > 0$. The magnetic field will be

$$B_x = \frac{\mu_0 I}{2\pi x} \tag{6.95}$$

where I is the current through the wire. This will impart an acceleration on the mass of

$$a_{dia} = -\frac{\chi_m \mu_0 I}{4\pi^2} x^{-3}. \tag{6.96}$$

If we desired to maintain a constant acceleration, the current can be modified as the trajectories diverge from their initial position. Given that $a_{dia} \propto \frac{I}{x^3}$, this will require

$$I(x) = I(x_0)\left(\frac{x}{x_0}\right)^3 \tag{6.97}$$

As such, to control the motion of the mass through a range of, for example, 3 order

of magnitude will require the current to increase by 9 orders of magnitude. To put this another way, for every $\times 10$ increase in the superposition size, the current must be increased $\times 10^3$ to maintain any significant acceleration.

It is also worth highlighting that the diamagnetic acceleration is completely mass independent, which may ease the requirement of re-using the test mass to ensure phase and trajectory stability and potentially allow far greater superpositions to be obtained.

There are however, still two questions that need to be answered:

1. How to create the initial spatial splitting assumed in the above analysis.

2. Given the significant acceleration cannot be maintained through a large spatial region (Equation 6.97), how can we hope to create a large superposition using this method.

The first question has a simple answer in typical SG interferometry considered previously. The splitting could be achieved using the SG effect, using the aforementioned free flight method, whereby the spin states are rapidly accelerated apart in the x direction before being dropped onto the x axis. The second question has two obvious solutions, the first is the masses could simply be rapidly accelerated before being allowed to once again freely fall. Provided the diamagnetic acceleration is much larger than what is achieved using the SG effect, which we know to be the case, this should enable much larger superpositions to be obtained. However, this will still lead to $\Delta x_{max} \propto t$ scaling. Alternatively the fact that y axis motion is required to 'drop' the trajectories either side of the current carrying wire can be leveraged. By continuously dropping the trajectories onto pairs of wires, each further out than the last, multiple sets of diamagnetically repulsive wires can be utilised to maintain a significant acceleration throughout the entire interferometry process. Through this method, the diamagnetic induced acceleration could be maintained at a constant level, leading to $\Delta x_{max} \propto t^2$ scaling which should dramatically increase the spatial splitting achievable.

The general interferometry process would thus be

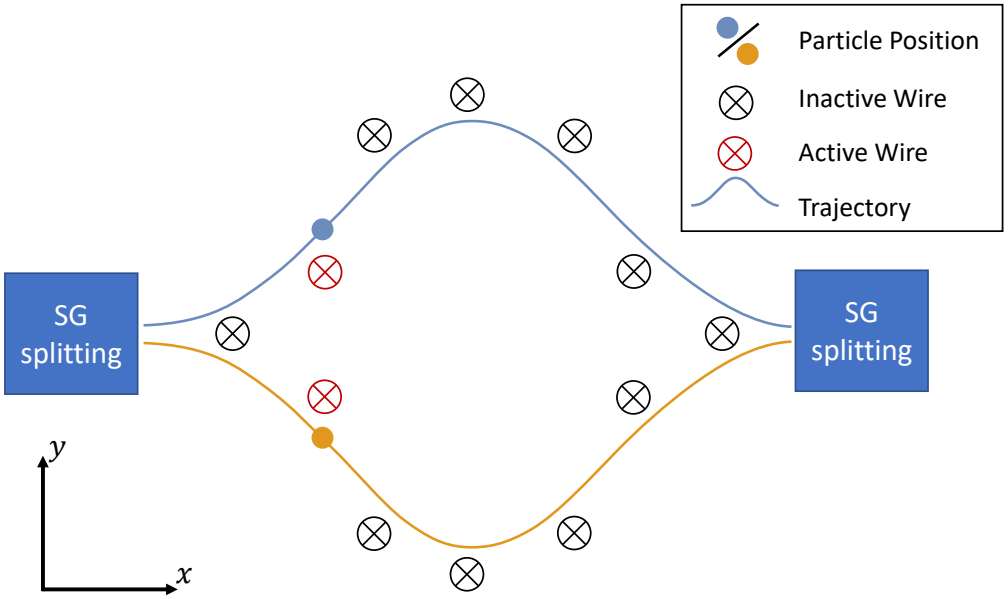

Figure 6.6: Overview of proposed massive particle interferometer using diamagnetic repulsion.

1. A mass is initialised in a trap with in a spin $s_x = \pm 1$ superposition state. At $t = t_0$, the mass will be launched with some velocity v_y in the y direction.

2. The mass will pass through some standard Stern-Gerlach apparatus. This will induce a small spin dependent spatial splitting before the internal spin states are mapped to

3. The two mass states are then diamagnetically repulsed by a series of current carrying wires. Only the nearest (pair) of wire(s) would need to be used at any given time. In this way a constant acceleration can be achieved and the trajectories can be controlled.

4. Once the two trajectories are brought close to one another, a second SG apparatus can be used to close the superposition.

This process is shown in Figure 6.6 and should enable significantly greater spatial splitting to be achieved.

6.7 Old - Free Flight Method

To begin, I will present the initial design thoughts which were largely used in the previous chapters as the example form that the interferometer takes.

To gain an initial insight into the motion expected (see figure **??**) we can consider the direction and magnitude of the interaction terms

$$H_{\text{diamegnetic}} = -\frac{\chi_V V}{2\mu_0}\hat{B}^2 \tag{6.98}$$

and

$$H_{\text{NV}} = -\hat{\mu}\hat{B}. \tag{6.99}$$

In previous work, the magnetic field source considered consists of a trapping potential [151], we will begin by also considering this, before expanding into what may be achieved by combining multiple of these together. We will discuss later the reasonableness of each solution. The motion will be the result of the force on the particle due to the magnetic field gradient coupling given as

$$\begin{aligned} F_{\text{diamegnetic}} =& \frac{d}{dx}\frac{\chi_m m}{2\mu_0}\hat{B}^2 \\ =& \frac{\chi_m m}{\mu_0}\hat{B}\partial_x\hat{B} \end{aligned} \tag{6.100}$$

$$\tag{6.101}$$

and

$$\begin{aligned} F_{\text{NV}} =& \frac{d}{dx}\hat{\mu}\hat{B} \\ =& \hat{\mu}\,\partial_x\hat{B} \\ =& -\frac{g e\hbar}{2m_e}\partial_x\hat{B} \end{aligned} \tag{6.102}$$

where $\partial_x\hat{B}$ is the magnetic field gradient in the x direction, g is the Lagendè g-factor, e and m_e is the charge and mass of an electron.

Thus the relative strength of each effect depends on how the magnetic field gradient varies with distance from the magnetic field source and the strength of the magnetic field itself. This suggests, if we intend to primarily control the motion of the particle we require

$$\begin{aligned} \left|F_{\text{diamegnetic}}\right| &\ll |F_{\text{NV}}| \\ |B| &\ll \frac{ge\mu_0\hbar}{-2\chi_m m_e m} \end{aligned} \tag{6.103}$$

From which we can define a maximum permissible magnetic field amplitude experienced by the interferometric particle, taken here to be diamond ($\chi_m = -6.2\times10^{-9}$ $\mathrm{m_3kg^{-1}}$) of

(6.104)

This will, for example, require a magnetic field of magnitude $B \ll 3\times10^{-7}$ T when using a mass $m = 10^{15}$.

6.7.1 Trapping potential

The difficulty here now lies in the fact that the magnetic field must be small, while maintaining a large magnetic field gradient. This must also be achieved while ensuring a sufficient distance to minimise particle-magnet interactions among other considerations. Still considering ta trapping potential, with the particle beginning in the centre of trap, where the magnetic field is zero. Requiring an, at least approximately, constant magnetic field gradient, implies a linear (or approximately linear) magnetic field. This then implies the window in which a magnetic field source can control a particle is incredibly small. Specifically the particle can be controlled by that magnetic field through a displacement s given by

$$s = \frac{B_M}{\partial_x \vec{B}} \tag{6.105}$$

which, for our example parameters of a mass $m = 10^{-15}$ kg diamond gives $s \sim$ 0.03 nm.

Naively one could consider the use of the same magnetic field gradient shared between the two arms, with the mass reduced to allow a suitable superposition size. For example, desiring $s = 200\ \mu$m, corresponding to using a mass $m \lesssim 10^{-22}$ kg. This however is not the optimal manner of determining the experimental parameters, particularly as smaller masses will likely be less sensitive to any signals the interferometer is being employed to detect. For example, they will entangle slower and be less sensitive to space-time curvature and gravitational waves. For each order of magnitude reduction in mass, we can however also lower the magnetic field gradient by an order of magnitude. Considering this we can conclude a mass $m = 10^{-18}$ kg, and a corresponding magnetic field gradient of $\partial_x \vec{B} = 16$ Tm^{-1} is sufficient. This however does not take into account the time required to complete the interferometry. This however could be further pushed to larger masses by allowing more than one magnetic field source, switching one set on as the previous is turned off. So using 101 magnetic field gradient sources, a 200 μm superposition size may be achievable with a mass $m \leq 10^{-17}$ and $\partial_x \vec{B} = 16$ Tm^{-1}.

This however can still be further improved upon, particularly with the goal here of generating the largest spatial superposition possible, with as large a mass as possible. Alternatively we might consider a QGEM type experimental goal. If this is the case then one must consider the rate of entanglement formation, and the ability to open and close the superposition. To get around these issues in a QGEM experiment, it is likely necessary to employ the parallel set-up as proposed by others []. Here though, I will focus on the problem of creating the largest superposition possible, both with respect to superposition size and mass.

To achieve this goal I then consider the use of free flight during the interferometry process. By employing a large magnetic field gradient over a very short time-frame before letting the particle propagate freely we might hope to increase the superposition size without employing a large number of magnetic field sources as shown in figure **??**. Using this method, an initial acceleration time t_a and free-flight time t_f between accelerations (and hence a total time $T = 4t_a + 2t_f$) we can

create a maximum superposition size

$$\begin{aligned}\Delta x =& a t_a^2 + a t_a t_f \\ =& \frac{g e \hbar}{2 m_e m} \partial_x \hat{B} \left(t_a^2 + t_a \frac{1}{2} (T - 4 t_a) \right) \\ =& \frac{g e \hbar}{2 m_e m} \partial_x \hat{B} \left(\frac{1}{2} t_a T - t_a^2 \right)\end{aligned} \tag{6.106}$$

I initially considered using only 3 magnetic field sources, with one handling the initial and final accelerations and the other two handling the acceleration in between (acting as the mirrors) as seen in figure **??**. The maximum t_a will then be determined by equation 6.105. Specifically

$$t_a = \sqrt{2 \frac{s}{a}} \tag{6.107}$$

$$t_a = \sqrt{\frac{4 m_e m B_M}{g e \hbar \left(\partial_x \hat{B} \right)^2}} \tag{6.108}$$

which I further simplified by considering equation **??** giving

$$\begin{aligned}t_a =& \sqrt{\frac{4 m_e m}{g e \hbar \left(\partial_x \hat{B} \right)^2} \frac{g e \mu_0 \hbar}{-10 \times 2 \chi_m m_e m}} \\ =& \sqrt{\frac{\mu_0}{-5 \chi_m \left(\partial_x \hat{B} \right)^2}}\end{aligned} \tag{6.109}$$

and thus

$$\begin{aligned}\Delta x =& \frac{g e \hbar}{2 m_e m} \partial_x \hat{B} \left(\frac{1}{2} \sqrt{\frac{\mu_0}{-5 \chi_m \left(\partial_x \hat{B} \right)^2}} T - \frac{\mu_0}{-5 \chi_m \left(\partial_x \hat{B} \right)^2} \right) \\ \Delta x =& \frac{g e \hbar}{2 m_e m} \left(\frac{1}{2} \sqrt{\frac{\mu_0}{-5 \chi_m}} T - \frac{\mu_0}{-5 \chi_m \partial_x \hat{B}} \right).\end{aligned} \tag{6.110}$$

When accounting for when the total time does not allow for free flight to occur,

$$\Delta x = \begin{cases} \frac{g\not{e}\hbar}{2m_e m}\left(\frac{1}{2}\sqrt{\frac{\mu_0}{-5\chi_m}}T - \frac{\mu_0}{-5\chi_m\partial_x\hat{B}}\right) & \sqrt{\frac{\mu_0}{-5\chi_m\left(\partial_x\hat{B}\right)^2}} \leq \frac{1}{4}T \\ \frac{g\not{e}\hbar}{2m_e m}\partial_x\hat{B}\left(\frac{1}{4}T\right)^2 & \sqrt{\frac{\mu_0}{-5\chi_m\left(\partial_x\hat{B}\right)^2}} > \frac{1}{4}T \end{cases} \tag{6.111}$$

which is plotted in figure **??** and **??**. If instead of 3 magnetic field sources (two acting as mirrors and one splitting then recombining the masses), N magnetic field sources acting as a single mirror, so $4N-1$ total magnets in total, is used, equation 6.107 becomes $t_a = \sqrt{2\frac{(2N-1)s}{a}}$ giving

$$\Delta x = \begin{cases} \frac{g\not{e}\hbar}{2m_e m}\left(\frac{1}{2}\sqrt{\frac{\mu_0(2N-1)}{-5\chi_m}}T - \frac{\mu_0(2N-1)}{-5\chi_m\partial_x\hat{B}}\right) & \sqrt{\frac{\mu_0(2N-1)}{-5\chi_m\left(\partial_x\hat{B}\right)^2}} \leq \frac{1}{4}T \\ \frac{g\not{e}\hbar}{2m_e m}\partial_x\hat{B}\left(\frac{1}{4}T\right)^2 & \sqrt{\frac{\mu_0(2N-1)}{-5\chi_m\left(\partial_x\hat{B}\right)^2}} > \frac{1}{4}T \end{cases} \tag{6.112}$$

Chapter 7

Conclusion

In this chapter, I will begin by summarising some of the other projects that I was involved in during my PhD which are related to the work in this thesis. I will then briefly summarise each chapter in this thesis before making some concluding remarks on this work and highlight some key questions for future study.

7.1 Supervisory Work

This section will outline the two masters projects that are closely related to the work done in my thesis. These projects were conducted by Jules Tilly (7.1.1) and Daniel Germon (7.1.2). However, I contributed significantly to these projects as I acted as the day to day supervisor throughout the projects.

7.1.1 Qudits Optimisation of the QGEM protocol

This project was concerned with optimising the QGEM protocol by considering the use of qudits, the geometric arrangement of the interferometer arms and the entanglement witness. The project aimed to reduce the difficulty of the required experimental parameters to implement the QGEM protocol. It was found that using higher-dimensional qudits, rather than just qubits of dimension 2, the two masses entangle slower. However, this entanglement is more robust to the presence of decoherence. As such, we showed that the minimum dimensionally qudits are desirable. In a realistic experiment, it may well be necessary to use qutrits or higher dimensional qudits rather than qubits to ensure that a measurable amount of decoherence remains within the system. By modifying the geometric arrangement of the interfer-

ometer, the experimental parameter can all be reduced, although likely be at most an order of magnitude. While this is a small improvement, any improvement is welcome, given the difficulty of implementing this experiment. Finally, this work provided a detailed analysis required for deciding on the best form of entanglement witness, depending on the level of decoherence and level of certainty that entanglement is indeed found.

This work has been published under the title *Qudits for Witnessing Quantum Gravity Induced Entanglement of Masses Under Decoherence*.

7.1.2 Optimising Signal Detection in the Presence of Noise

This project considered how to extract specific space-time metric component signals from a MIMAC detector. This analysis was again considered decoherence and noise within the output signal of the standard MIMAC detector. It compared the direct detection of the second-order space-time curvature with detecting the first order curvature at two separate locations and inferring the second-order curvature term. This suggested it would indeed be easier to move the detector. The project also looked at whether the original detector could be modified in such a way as to cancel specific terms so they do not contribute to the final output signal. This line of work was sadly ultimately unsuccessful. Finally, this project considered how to extract the actual value of the phase difference given it can only be measured modulo 2π. This was found to be possible provided the apparatus could be rotated relative to the signal source by a sufficiently small amount. A procedure was then developed in which the angular distance between two arrangements that yield the same phase difference modulo 2π could be used to calculate the absolute phase difference.

7.2 Summary and Discussion of Results

In Part I I have presented my work on understanding what aspects of quantum gravity may be evidenced using large mass interferometers (Chapter 2). I discussed how it would only probe the linearised, infrared regime. However, this would be sufficient to evidence any fundamentally quantum nature of gravity. I have also presented interpretations of such a quantum gravitational force through standard rel-

ativistic quantum mechanics; notably, I highlighted the fundamental assumptions that must be taken and ideally verified before any conclusion could be drawn from the positive result of a QGEM experiment. The most significant assumption is that the quantum gravitational interaction acts locally, avoiding any action at a distance between the two masses used in the QGEM experiment. Finally, I present how the experiment could still hold with *limited* non-locality. Provided the non-local scale is much less than any interaction distance involved in the experiment. In Chapter 3 I present the work done towards modelling two quantum masses through a quantum gravitational field. This work largely consists of models considering very restrictive assumptions and so is considered incomplete at this stage. However, a logarithmic rate of entropy growth was found. A similar behaviour witnessed in many-body localised systems [158], which opens up interesting possibilities in searching for further parallels.

Part II covers work on understanding how large mass interferometers could serve as detectors capable of measuring space-time curvature, including gravitational waves. I found that large mass interferometers could be used as very sensitive detectors while remaining modest in size. Most impressively approaching the sensitivity of laser-based interferometers for detecting gravitational waves while being 4000 times smaller. While in Chapter 4 I present the sensitivity results while being optimistic about the ability to build such a device, Chapter 5 presents an initial analysis of the reasonableness of such a device. In particular, I consider many of the primary sources of noise and uncertainty. By doing so, I can determine what limitations are placed on the sensitivity and find that an ambitious mixture of current and near-future experimental parameters are sufficient when building such a device. I have also discussed the role multiple interferometers could play in actively removing low frequency noise from a signal.

Part III contains a single chapter (6) in which I detail the work done on designing a Stern-Gerlach interferometer. This aimed to address the limitation of the diamagnetic interaction, which will become significant as the interfered mass becomes heavier. I also sought to design around various other issues which will likely

arise, such as Majorana spin-flip transitions. In doing so, I found that the standard Stern-Gerlach interferometer has a natural limitation on the spatial superposition size achievable within a given time. It appears that the splitting size will always grow linearly with time. As a result, it appears that a new method of reaching larger spatial splitting will be required before the experimental parameters proposed in the original QGEM proposal will be possible. However, the level of spatial splitting of large mass particles achievable by the device discussed here may still be well beyond what has been achieved previously.

7.3 Conclusion

In this thesis I have considered the role large mass interferometry could have in future experiments to detect many different aspects of gravity. The hope of achieving large spatial splitting with large masses has only recently become a near-future possibility [27], and so the field of large mass interferometry is currently largely unexplored. As such, I have taken a fairly broad approach to understanding their use as gravity detectors. In doing so, I found that large mass interferometers promise to be a powerful tool for measuring many aspects of gravity, from evidencing any underlying quantum nature to the direct detection of the curvature of space-time. I have also found that building such a device will require a tremendous amount of effort but is in principle feasible with at most modest advances on current-day technology. This is, however, assuming that the current state of the art results from many different experiments can be combined into a single apparatus.

This has opened up many new research questions worthy of further study. The work done to model entanglement formation through two gravitating masses is currently incomplete. It is hoped that a more easily implemented method of implementing a QGEM experiment may be found by fully understanding this.

Another interesting question is the role such a device could play in detecting further modifications to gravity, perhaps most interestingly at extremely close ranges. As these devices are very sensitive to the local gravitational field, they may measure very weak modifications to the standard Newtonian potential. There is still

a lot of work necessary to ensure that all sources of noise and decoherence are accounted for. Methods to counteract these noise and decoherence sources must then be developed to ensure that an experiment can obtain meaningful results. Chapter 5 and the Toroš paper [149] in which I participated represent work in this direction. However, these will have to be adapted to more realistic interferometers, such as those discussed in Chapter 6. Furthermore, the calculations need to be conducted for full noise spectrum as measured at possible experiment sights.

Finally, given that significant limitations have been placed on the spatial superposition size achievable within any given time frame, more creative methods of creating the spatial splitting will be required to realise the most ambitious interferometer considered here. These could include advances in material science to avoid the impacts of diamagnetism, more innovative experimental set-ups still leveraging the Stern-Gerlach effect, or potential entirely new methods of creating the large spatial superpositions required.

Bibliography

[1] R. Colella, A. W. Overhauser, and S. A. Werner, Physical Review Letters **34**, 1472 (1975).

[2] T. Kovachy, P. Asenbaum, C. Overstreet, C. Donnelly, S. Dickerson, A. Sugarbaker, J. Hogan, and M. Kasevich, Nature **528**, 530 (2015).

[3] Y. Margalit, O. Dobkowski, Z. Zhou, O. Amit, Y. Japha, S. Moukouri, D. Rohrlich, A. Mazumdar, S. Bose, C. Henkel, *et al.*, Science Advances **7**, eabg2879 (2021).

[4] S. Bose, A. Mazumdar, G. W. Morley, H. Ulbricht, M. Toroš, M. Paternostro, A. A. Geraci, P. F. Barker, M. S. Kim, and G. Milburn, Phys. Rev. Lett. **119**, 240401 (2017), 1707.06050 .

[5] C. Marletto and V. Vedral, Phys. Rev. Lett. **119**, 240402 (2017).

[6] A. D. Cronin, J. Schmiedmayer, and D. E. Pritchard, Rev. Mod. Phys. **81**, 1051 (2009).

[7] S. Gerlich, L. Hackermüller, K. Hornberger, A. Stibor, H. Ulbricht, M. Gring, F. Goldfarb, T. Savas, M. Müri, M. Mayor, *et al.*, Nature Physics **3**, 711 (2007).

[8] S. Bose, K. Jacobs, and P. L. Knight, Physical Review A **59**, 3204 (1999).

[9] A. D. Armour, M. P. Blencowe, and K. C. Schwab, Physical Review Letters **88**, 148301 (2002).

[10] W. Marshall, C. Simon, R. Penrose, and D. Bouwmeester, Physical Review Letters **91**, 130401 (2003).

[11] P. Sekatski, M. Aspelmeyer, and N. Sangouard, Physical Review Letters **112**, 080502 (2014).

[12] O. Romero-Isart, M. L. Juan, R. Quidant, and J. I. Cirac, New Journal of Physics **12**, 033015 (2010).

[13] O. Romero-Isart, A. C. Pflanzer, F. Blaser, R. Kaltenbaek, N. Kiesel, M. Aspelmeyer, and J. I. Cirac, Physical Review Letters **107**, 020405 (2011).

[14] F. Khalili, S. Danilishin, H. Miao, H. Müller-Ebhardt, H. Yang, and Y. Chen, Physical Review Letters **105**, 070403 (2010).

[15] M. Scala, M. S. Kim, G. W. Morley, P. F. Barker, and S. Bose, Physical Review Letters **111**, 180403 (2013).

[16] J. Bateman, S. Nimmrichter, K. Hornberger, and H. Ulbricht, Nature Communications **5**, 4788 (2014).

[17] Z. Q. Yin, T. Li, X. Zhang, and L. M. Duan, Physical Review A **88**, 033614 (2013).

[18] H. Pino, J. Prat-Camps, K. Sinha, B. P. Venkatesh, and O. Romero-Isart, Quantum Science and Technology **3**, 025001 (2018).

[19] J. Clarke and M. R. Vanner, Quantum Science and Technology **4**, 014003 (2019).

[20] M. Ringbauer, T. J. Weinhold, L. Howard, A. White, and M. Vanner, New Journal of Physics **20**, 053042 (2018).

[21] K. E. Khosla, M. R. Vanner, N. Ares, and E. A. Laird, Physical Review X **8**, 021052 (2018).

[22] R. Kaltenbaek, G. Hechenblaikner, N. Kiesel, O. Romero-Isart, K. C. Schwab, U. Johann, and M. Aspelmeyer, Experimental Astronomy **34**, 123 (2012).

[23] C. Wan, M. Scala, G. W. Morley, A. A. Rahman, H. Ulbricht, J. Bateman, P. F. Barker, S. Bose, and M. S. Kim, Physical Review Letters **117**, 143003 (2016).

[24] O. Romero-Isart, New Journal of Physics **19**, 123029 (2017).

[25] R. Penrose, General relativity and gravitation **28**, 581 (1996).

[26] A. Bassi, K. Lochan, S. Satin, T. P. Singh, and H. Ulbricht, Reviews of Modern Physics **85**, 471 (2013).

[27] S. Machluf, Y. Japha, and R. Folman, Nature Communications **4**, 2424 (2013).

[28] O. Amit, Y. Margalit, O. Dobkowski, Z. Zhou, Y. Japha, M. Zimmermann, M. A. Efremov, F. A. Narducci, E. M. Rasel, W. P. Schleich, and R. Folman, Phys. Rev. Lett. **123**, 083601 (2019).

[29] J. Anandan, Physical Review B **30**, 3717 (1984).

[30] J. M. Mcguirk, G. T. Foster, J. B. Fixler, M. J. Snadden, and M. A. Kasevich, Physical Review A **65**, 033608 (2002).

[31] S. Qvarfort, A. Serafini, P. F. Barker, and S. Bose, Nature Communications **9**, 3690 (2018).

[32] F. Armata, L. Latmiral, A. D. K. Plato, and M. S. Kim, Physical Review A **96**, 043824 (2017).

[33] P. Asenbaum, C. Overstreet, T. Kovachy, D. D. Brown, J. M. Hogan, and M. A. Kasevich, Physical review letters **118**, 183602 (2017).

[34] S. A. Werner, J. L. Staudenmann, and R. Colella, Phys. Rev. Lett. **42**, 1103 (1979).

[35] J. Anandan, Physical Review D **15**, 1448 (1977).

[36] S. Dimopoulos, P. W. Graham, J. M. Hogan, and M. A. Kasevich, Physical Review D **78**, 042003 (2008).

[37] C. W. F. Everitt, D. B. DeBra, B. W. Parkinson, J. P. Turneaure, J. W. Conklin, M. I. Heifetz, G. M. Keiser, A. S. Silbergleit, T. Holmes, J. Kolodziejczak, M. Al-Meshari, J. C. Mester, B. Muhlfelder, V. G. Solomonik, K. Stahl, P. W. Worden, W. Bencze, S. Buchman, B. Clarke, A. Al-Jadaan, H. Al-Jibreen, J. Li, J. A. Lipa, J. M. Lockhart, B. Al-Suwaidan, M. Taber, and S. Wang, Phys. Rev. Lett. **106**, 221101 (2011).

[38] A. Roura, Physical review letters **118**, 160401 (2017).

[39] A. Roura, Physical review X **10**, 021014 (2020).

[40] B. P. Abbott, R. Abbott, T. Abbott, M. Abernathy, F. Acernese, K. Ackley, C. Adams, T. Adams, P. Addesso, R. Adhikari, *et al.*, Physical Review Letters **116**, 061102 (2016).

[41] G. M. Harry, L. S. Collaboration, *et al.*, Classical and Quantum Gravity **27**, 084006 (2010).

[42] R. Y. Chiao and A. D. Speliotopoulos, Journal of Modern Optics **51**, 861 (2004).

[43] A. Roura, D. R. Brill, B. L. Hu, C. W. Misner, and W. D. Phillips, Phys. Rev. D **73**, 084018 (2006).

[44] S. Foffa, A. Gasparini, M. Papucci, and R. Sturani, Physical Review D **73**, 022001 (2006).

[45] S. Dimopoulos, P. W. Graham, J. M. Hogan, M. A. Kasevich, and S. Rajendran, Physical Review D **78**, 122002 (2008).

[46] S. Dimopoulos, P. W. Graham, J. M. Hogan, M. A. Kasevich, and S. Rajendran, Physics Letters B **678**, 37 (2009).

[47] B. Canuel, A. Bertoldi, L. Amand, E. Pozzo di Borgo, T. Chantrait, C. Danquigny, M. Dovale Álvarez, B. Fang, A. Freise, R. Geiger, J. Gillot, S. Henry, J. Hinderer, D. Holleville, J. Junca, G. Lefèvre, M. Merzougui, N. Mielec, T. Monfret, S. Pelisson, M. Prevedelli, S. Reynaud, I. Riou, Y. Rogister, S. Rosat, E. Cormier, A. Landragin, W. Chaibi, S. Gaffet, and P. Bouyer, Scientific Reports **8**, 14064 (2018).

[48] P. W. Graham, J. M. Hogan, M. A. Kasevich, S. Rajendran, and R. W. Romani, arXiv preprint arXiv:1711.02225 (2017).

[49] D. Rätzel, F. Schneiter, D. Braun, T. Bravo, R. Howl, M. P. E. Lock, and I. Fuentes, New Journal of Physics **20**, 053046 (2018).

[50] D. Rätzel, R. Howl, J. Lindkvist, and I. Fuentes, New Journal of Physics **20**, 073044 (2018).

[51] A. Arvanitaki and A. A. Geraci, Phys. Rev. Lett. **110**, 071105 (2013).

[52] A. Pontin, L. S. Mourounas, A. A. Geraci, and P. F. Barker, New Journal of Physics **20**, 023017 (2018).

[53] M. Ando, K. Ishidoshiro, K. Yamamoto, K. Yagi, W. Kokuyama, K. Tsubono, and A. Takamori, Physical review letters **105**, 161101 (2010).

[54] C. Moller, Nucl. Phys **40**, 353 (1963).

[55] L. Rosenfeld, Nuclear Physics **40**, 353 (1963).

[56] L. Diosi, Physics letters A **120**, 377 (1987).

[57] D. Kafri, J. Taylor, and G. Milburn, New Journal of Physics **16**, 065020 (2014).

[58] D. Kafri, G. Milburn, and J. Taylor, New Journal of Physics **17**, 015006 (2015).

[59] D. Carney, P. C. E. Stamp, and J. M. Taylor, Classical and Quantum Gravity **36**, 034001 (2019).

[60] A. Tilloy and L. Diósi, Physical Review D **93**, 024026 (2016).

[61] T. Jacobson, Physical Review Letters **75**, 1260 (1995).

[62] J. Oppenheim, arXiv preprint arXiv:1811.03116 (2018).

[63] R. Feynman, *Feynman lectures on gravitation* (CRC Press, 2018).

[64] M. Srednicki, *Quantum field theory* (Cambridge University Press, 2007).

[65] C. Anastopoulos and B.-L. Hu, arXiv preprint arXiv:1804.11315 (2018).

[66] M. J. Hall and M. Reginatto, Journal of Physics A: Mathematical and Theoretical **51**, 085303 (2018).

[67] C. Marletto and V. Vedral, Physical Review D **98**, 046001 (2018).

[68] M. Christodoulou and C. Rovelli, Physics Letters B **792**, 64 (2019).

[69] M. Christodoulou and C. Rovelli, Frontiers in Physics **8**, 207 (2020).

[70] A. Belenchia, R. M. Wald, F. Giacomini, E. Castro-Ruiz, Č. Brukner, and M. Aspelmeyer, International Journal of Modern Physics D **28**, 1943001 (2019).

[71] S. M. Giampaolo and T. Macrì, Scientific reports **9**, 1 (2019).

[72] H. C. Nguyen and F. Bernards, The European Physical Journal D **74**, 1 (2020).

[73] M. Carlesso, A. Bassi, M. Paternostro, and H. Ulbricht, New Journal of Physics **21**, 093052 (2019).

[74] A. Al Balushi, W. Cong, and R. B. Mann, Physical Review A **98**, 043811 (2018).

[75] J. J. Sakurai and E. D. Commins, "Modern quantum mechanics, revised edition," (1995).

[76] S. M. Carroll, (1997), gr-qc/9712019v1 .

[77] C. W. Misner, K. S. Thorne, and J. A. Wheeler, *Gravitation* (Princeton University Press, 2017).

[78] P. Van Nieuwenhuizen, Nucl. Phys. **B60**, 478 (1973).

[79] T. Biswas, T. Koivisto, and A. Mazumdar, in *Proceedings, Barcelona Postgrad Encounters on Fundamental Physics* (2013) pp. 13–24, arXiv:1302.0532 [gr-qc] .

[80] T. W. van de Kamp, R. J. Marshman, S. Bose, and A. Mazumdar, Physical Review A **102**, 062807 (2020).

[81] M. Horodecki, P. Horodecki, and R. Horodecki, Physical Review Letters **80**, 5239 (1998).

[82] C. H. Bennett, D. P. DiVincenzo, J. A. Smolin, and W. K. Wootters, Physical Review A **54**, 3824 (1996).

[83] E. T. Tomboulis, (1997), arXiv:hep-th/9702146 [hep-th] .

[84] T. Biswas, A. Mazumdar, and W. Siegel, Journal of Cosmology and Astroparticle Physics **2006**, 009 (2006).

[85] T. Biswas, E. Gerwick, T. Koivisto, and A. Mazumdar, Phys. Rev. Lett. **108**, 031101 (2012), arXiv:1110.5249 [gr-qc] .

[86] W. Siegel, (2003), arXiv:hep-th/0309093 .

[87] L. Buoninfante, A. S. Koshelev, G. Lambiase, J. Marto, and A. Mazumdar, JCAP **1806**, 014 (2018), arXiv:1804.08195 [gr-qc] .

[88] J. Polchinski, *String theory. Vol. 2: Superstring theory and beyond*, Cambridge Monographs on Mathematical Physics (Cambridge University Press, 2007).

[89] J. Ambjorn, A. Goerlich, J. Jurkiewicz, and R. Loll, Phys. Rept. **519**, 127 (2012), arXiv:1203.3591 [hep-th] .

[90] C. Rovelli and L. Smolin, Nucl. Phys. **B442**, 593 (1995), [Erratum: Nucl. Phys.B456,753(1995)], arXiv:gr-qc/9411005 [gr-qc] .

[91] C. de Lacroix, H. Erbin, S. P. Kashyap, A. Sen, and M. Verma, Int. J. Mod. Phys. **A32**, 1730021 (2017), arXiv:1703.06410 [hep-th] .

[92] E. Witten, Nucl. Phys. **B268**, 253 (1986).

[93] P. G. O. Freund and E. Witten, Phys. Lett. **B199**, 191 (1987).

[94] P. G. O. Freund and M. Olson, Phys. Lett. **B199**, 186 (1987).

[95] D. J. Kapner, T. S. Cook, E. G. Adelberger, J. H. Gundlach, B. R. Heckel, C. D. Hoyle, and H. E. Swanson, Phys. Rev. Lett. **98**, 021101 (2007), arXiv:hep-ph/0611184 [hep-ph] .

[96] W.-H. Tan, S.-Q. Yang, C.-G. Shao, J. Li, A.-B. Du, B.-F. Zhan, Q.-L. Wang, P.-S. Luo, L.-C. Tu, and J. Luo, Phys. Rev. Lett. **116**, 131101 (2016).

[97] C. C. Haddock *et al.*, Phys. Rev. **D97**, 062002 (2018), arXiv:1712.02984 [nucl-ex] .

[98] T. Biswas, A. S. Koshelev, and A. Mazumdar, Fundam. Theor. Phys. **183**, 97 (2016), arXiv:1602.08475 [hep-th] .

[99] T. Biswas, A. Conroy, A. S. Koshelev, and A. Mazumdar, Class. Quant. Grav. **31**, 015022 (2014), [Erratum: Class. Quant. Grav.31,159501(2014)], arXiv:1308.2319 [hep-th] .

[100] V. P. Frolov, A. Zelnikov, and T. de Paula Netto, JHEP **06**, 107 (2015), arXiv:1504.00412 [hep-th] .

[101] J. Edholm, A. S. Koshelev, and A. Mazumdar, Phys. Rev. **D94**, 104033 (2016), arXiv:1604.01989 [gr-qc] .

[102] L. Buoninfante, G. Lambiase, and A. Mazumdar, The European Physical Journal C **78**, 73 (2018).

[103] L. Buoninfante, G. Lambiase, and A. Mazumdar, Nuclear Physics B **931**, 250 (2018).

[104] M. Born, Nature **132**, 282.1 (1933).

[105] M. Born and L. Infeld, Proc. Roy. Soc. Lond. **A144**, 425 (1934).

[106] J. Boos, V. P. Frolov, and A. Zelnikov, Phys. Lett. **B782**, 688 (2018), arXiv:1805.01875 [hep-th] .

[107] V. P. Frolov and A. Zelnikov, Phys. Rev. **D98**, 084035 (2018), arXiv:1809.00417 [hep-th] .

[108] A. Pais and G. E. Uhlenbeck, Phys. Rev. **79**, 145 (1950).

[109] G. V. Efimov, Commun. Math. Phys. **5**, 42 (1967).

[110] E. T. Tomboulis, Phys. Rev. **D92**, 125037 (2015), arXiv:1507.00981 [hep-th] .

[111] L. Buoninfante, G. Lambiase, and A. Mazumdar, Nucl. Phys. **B**, 114646 (2019), arXiv:1805.03559 [hep-th] .

[112] L. Buoninfante and A. Mazumdar, Physical Review D **100**, 024031 (2019).

[113] C. Wan, M. Scala, G. W. Morley, A. A. Rahman, H. Ulbricht, J. Bateman, P. Barker, S. Bose, and M. Kim, Physical review letters **117**, 143003 (2016).

[114] M. Visser, arXiv preprint arXiv:1802.00651 (2018).

[115] S. Weinberg, *Gravitation and cosmology: principles and applications of the general theory of relativity*, Vol. 1 (Wiley New York, 1972).

[116] B. P. Abbott *et al.*, Phys. Rev. **D93**, 112004 (2016), [Addendum: Phys. Rev.D97,no.5,059901(2018)], arXiv:1604.00439 [astro-ph.IM] .

[117] J. Ellis, M. Lewicki, and J. M. No, Journal of Cosmology and Astroparticle Physics **2019**, 003 (2019).

[118] P. Amaro-Seoane, H. Audley, S. Babak, J. Baker, E. Barausse, P. Bender, E. Berti, P. Binetruy, M. Born, D. Bortoluzzi, *et al.*, arXiv preprint arXiv:1702.00786 (2017).

[119] S. Bose and G. W. Morley, arXiv preprint arXiv:1810.07045 (2018).

[120] J. S. Pedernales, G. W. Morley, and M. B. Plenio, Physical Review Letters **125**, 023602 (2020).

[121] C. Subramaniam, T. Yamada, K. Kobashi, A. Sekiguchi, D. N. Futaba, M. Yumura, and K. Hata, Nature communications **4**, 1 (2013).

[122] O. Romero-Isart, Physical Review A **84**, 052121 (2011).

[123] D. Fitzakerley, M. George, E. Hessels, T. Skinner, C. Storry, M. Weel, G. Gabrielse, C. Hamley, N. Jones, K. Marable, *et al.*, Journal of Physics B: Atomic, Molecular and Optical Physics **49**, 064001 (2016).

[124] A. A. Rahman and P. Barker, Nature Photonics **11**, 634 (2017).

[125] C. E. Mungan and T. R. Gosnell, in *Advances in Atomic, Molecular, and Optical Physics*, Vol. 40 (Elsevier, 1999) pp. 161–228.

[126] N. Bar-Gill, L. M. Pham, A. Jarmola, D. Budker, and R. L. Walsworth, Nature Communications **4**, 1743 EP (2013).

[127] M. H. Abobeih, J. Cramer, M. A. Bakker, N. Kalb, M. Markham, D. J. Twitchen, and T. H. Taminiau, Nature Communications **9**, 2552 (2018).

[128] H. S. Knowles, D. M. Kara, and M. Atatüre, Nature materials **13**, 21 (2014).

[129] A. M. Steane, Physics Letters A **381**, 3905 (2017).

[130] S. A. Hughes and K. S. Thorne, Physical Review D **58**, 122002 (1998).

[131] U. Delić, M. Reisenbauer, K. Dare, D. Grass, V. Vuletić, N. Kiesel, and M. Aspelmeyer, "Motional quantum ground state of a levitated nanoparticle from room temperature," (2019), arXiv:1911.04406 [quant-ph] .

[132] D. E. Chang, C. Regal, S. Papp, D. Wilson, J. Ye, O. Painter, H. J. Kimble, and P. Zoller, Proceedings of the National Academy of Sciences **107**, 1005 (2010).

[133] L. Ferialdi, A. Setter, M. Toroš, C. Timberlake, and H. Ulbricht, New Journal of Physics (2019).

[134] C. J. Moore, R. H. Cole, and C. P. L. Berry, Classical and Quantum Gravity **32**, 015014 (2014), 1408.0740v2 .

[135] J. Hogan, J. Hammer, S.-W. Chiow, S. Dickerson, D. Johnson, T. Kovachy, A. Sugarbaker, and M. Kasevich, Optics letters **36**, 1698 (2011).

[136] J. Harms, B. J. J. Slagmolen, R. X. Adhikari, M. C. Miller, M. Evans, Y. Chen, H. Müller, and M. Ando, Phys. Rev. D **88**, 122003 (2013).

[137] W. Chaibi, R. Geiger, B. Canuel, A. Bertoldi, A. Landragin, and P. Bouyer, Phys. Rev. D **93**, 021101(R) (2016).

[138] J. Harms, R. DeSalvo, S. Dorsher, and V. Mandic, Physical Review D **80**, 122001 (2009).

[139] P. R. Saulson, Physical Review D **30**, 732 (1984).

[140] M. Pitkin, S. Reid, S. Rowan, and J. Hough, Living reviews in relativity **14**, 5 (2011).

[141] J. Harms, Living reviews in relativity **18**, 3 (2015).

[142] K. Nishida, Proceedings of the Japan Academy, Series B **93**, 423 (2017).

[143] M. Frimmer, K. Luszcz, S. Ferreiro, V. Jain, E. Hebestreit, and L. Novotny, Phys. Rev. A **95**, 061801(R) (2017).

[144] C. Maher-McWilliams, P. Douglas, and P. F. Barker, Nature Photonics **6**, 386 EP (2012).

[145] H. Sugime, S. Esconjauregui, J. Yang, L. D'Arsié, R. A. Oliver, S. Bhardwaj, C. Cepek, and J. Robertson, Applied Physics Letters **103**, 073116 (2013).

[146] J. Kim, J. A. Cox, J. Chen, and F. X. Kärtner, Nature Photonics **2**, 733 (2008).

[147] L. H. Ford, Phys. Rev. A **58**, 4279 (1998).

[148] C. C. Speake and C. Trenkel, Phys. Rev. Lett. **90**, 160403 (2003).

[149] M. Toroš, T. W. van de Kamp, R. J. Marshman, M. Kim, A. Mazumdar, and S. Bose, Physical Review Research **3**, 023178 (2021).

[150] J. H. N. Loubser and J. A. van Wyk, Reports on Progress in Physics **41**, 1201 (1978).

[151] J. S. Pedernales, G. W. Morley, and M. B. Plenio, Physical Review Letters **125**, 023602 (2020).

[152] R. J. Marshman, A. Mazumdar, and S. Bose, Physical Review A **101**, 052110 (2020).

[153] R. J. Marshman, A. Mazumdar, G. W. Morley, P. F. Barker, S. Hoekstra, and S. Bose, New Journal of Physics **22**, 083012 (2020).

[154] J. Tilly, R. J. Marshman, A. Mazumdar, and S. Bose, arXiv preprint arXiv:2101.08086 (2021).

[155] C. T. Sebens, Synthese , 1 (2020).

[156] M. Bloom and K. Erdman, Canadian Journal of Physics **40**, 179 (1962).

[157] D. E. Platt, American Journal of Physics **60**, 306 (1992).

[158] J. H. Bardarson, F. Pollmann, and J. E. Moore, Physical review letters **109**, 017202 (2012).